

**THERMAL ANALYSIS OF THERMOELECTRIC POWER
GENERATOR; INCLUDING THERMAL STRESSES**

BY

ABDULRAHMAN SALMAN AL-MERBATI

A Thesis Presented to the
DEANSHIP OF GRADUATE STUDIES

KING FAHD UNIVERSITY OF PETROLEUM & MINERALS
DHAHRAN, SAUDI ARABIA

In Partial Fulfillment of the
Requirements for the Degree of

MASTER OF SCIENCE

In

MECHANICAL ENGINEERING

May 2012

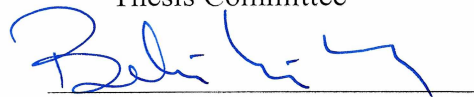
KING FAHD UNIVERSITY OF PETROLEUM AND MINERALS

DHAHRAN 31261, SAUDI ARABIA

DEANSHIP OF GRADUATE STUDIES

This thesis, written by ABDULRAHMAN SALMAN AL-MERBATI under the direction of his thesis advisor and approved by his thesis committee, has been presented to and accepted by the Dean of Graduate Studies, in partial fulfillment of the requirements for the degree of **MASTER OF SCIENCE in MECHANICAL ENGINEERING**.

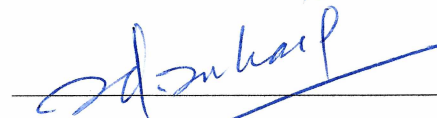
Thesis Committee



Dr. Bekir Sami Yilbas (Advisor)



Dr. Ahmet Z. Sahin (Member)



Dr. Sohail S. Akhtar (Member)



Dr. Amro M. Al-Qutub
Department Chairman



Dr. Salam A. Zummo
Dean of Graduate Studies



30/5/12

Date



**In the name of Allah, the Most Gracious and the
Most Merciful**

Dedicated to

My Beloved Parents

and

My Wife

ACKNOWLEDGMENTS

All praise and thanks are due to Almighty Allah, Most Gracious and Most Merciful, for his enormous beneficence and blessings and for giving me health, courage, knowledge and patience to complete this M.S. work. I seek his mercy, favor and forgiveness and I ask him to accept my little effort. And peace and blessings be upon our Prophet Muhammad, his family and his companions.

Acknowledgement is due to King Fahd University of Petroleum & Minerals (KFUPM) for providing support to this research work and granting me the opportunity to pursue graduate studies.

I am indebted to my thesis chairman, Dr. Bekir Yilbas for his help and advice. I acknowledge him, with deep gratitude and appreciation, for his valuable time, encouragement and continuous guidance given to me. Working with him was really a learning and valuable experience.

I am grateful to my thesis committee member, Dr. Ahmet Sahin for his suggestions and motivation. I am also highly grateful to my thesis committee member, Dr. Sohail Akhtar for his constructive guidance and support. His strong support and co-operation towards this research was a boon to me.

My heartfelt thanks are due to my family for their prayers, guidance, emotional and moral support throughout my academic life. I am grateful to my father (Salman) and my mother

(Fawzia) for their support and motivation during this M.S research work. No personal development could ever take place without the proper guidance from them. Special thanks to my wife (Sara) and my children (Salman, Layla and Azzam) for their patience and support throughout this period. I thank my family for sharing with me many precious moments for the sake of accomplishing my master degree.

Thanks are also due to my senior colleagues at the KFUPM for their Help and prayers especially Mr. Turki Baroud from Mechanical Engineering Department.

TABLE OF CONTENTS

ACKNOWLEDGMENTS	IV
LIST OF TABLES.....	VIII
LIST OF FIGURES.....	IX
THESIS ABSTRACT (ENGLISH)	XIV
THESIS ABSTRACT (ARABIC)	XVI
CHAPTER 1	1
1 INTRODUCTION	1
1.1 HISTORY OF THERMOELECTRICS	3
1.2 BACKGROUND OF THERMOELECTRICS	4
1.3 THERMOELECTRIC EFFECTS.....	7
1.3.1 Seebeck Effect	8
1.3.2 Peltier Effect.....	10
1.3.3 Thomson Effect	11
1.4 THERMOELECTRIC GENERATION AND THE FIGURE OF MERIT	11
1.5 THERMOELECTRIC MATERIALS.....	13
1.6 SCOPE OF THE WORK	17
1.7 THESIS OUTLINE.....	18
CHAPTER 2	19
2 LITERATURE REVIEW	19
2.1 THERMOELECTRIC MATERIAL AND SMALL SCALE STRUCTURES.....	19
2.2 THERMODYNAMICS OF TE DEVICES.....	27
2.3 THERMO-MECHANICAL STUDIES AND TE PERFORMANCE	29
2.4 OBJECTIVES AND APPROACH.....	41
CHAPTER 3	42
3 MATHEMATICAL ANALYSIS	42

3.1	THERMODYNAMICS ANALYSIS	42
3.2	THERMAL STRESS FORMULATIONS.....	48
3.2.1	Heat Transfer Analysis.....	48
3.2.2	Stress Analysis.....	52
CHAPTER 4	57
4	NUMERICAL MODELING	57
4.1	MODEL VALIDATION	60
4.2	MODELING ASSUMPTIONS.....	63
4.3	THERMOELECTRIC MODELING.....	65
4.3.1	Numerical Simulation	70
4.3.2	Boundary conditions	72
CHAPTER 5	75
5	RESULTS AND DISCUSSION.....	75
5.1	THERMODYNAMICS RESULTS	75
5.2	INFLUENCE OF THE PIN CONFIGURATIONS ON THE THERMAL STRESS.....	78
5.3	THERMAL CYCLING PERFORMANCE.....	106
CHAPTER 6	109
6	CONCLUSION AND RECOMMENDATION	109
	NOMENCLATURE	111
	REFERENCES	113
	VITA	121

LIST OF TABLES

Table 1.1	Classes of thermoelectric materials.....	16
Table 4.1	Properties of Bi_2Te_3 used for the efficiency calculation	59
Table 4.2	Maximum and Minimum von Mises stress for TE pins of present simulations with the previous study	62
Table 4.3	Material properties of TEG module, [T. depend means temperatures dependent].....	67
Table 5.1	Comparison of the Maximum stresses developed in TE pin for different configurations.....	105

LIST OF FIGURES

Figure 1.1 Sources of electricity in the U.S. in 2009 [1]	2
Figure 1.2 Conventional metallic thermocouple [8].....	5
Figure 1.3 Bulk semiconductor thermocouple (thermoelectric element) [9].....	6
Figure 1.4 Thermoelectric devices consist of TE modules [10]	7
Figure 1.5 The Seebeck circuit configured as (a) Generator. (b) Thermoelectric cooler [9]	8
Figure 1.6 Basic thermocouple circuit with instrument.....	9
Figure 1.7 Peltier effects: a current flow induces heat flow through the material	10
Figure 1.8 Thermoelectric Generation.....	11
Figure 1.9 Diagram of dependence for the three parameters on free carriers concentration [11].....	14
Figure 1.10 Figure of merit of commercial thermoelectric materials [12]	15
Figure 2.1 ZT versus the synthesis pressure (measured at room temperature) [22]	21
Figure 2.2 ZT as a function of temperature of $\text{Yb}_x\text{Fe}_y\text{Co}_{4-y}\text{Sb}_{12}$ [24].....	23
Figure 2.3 ZT vs. temperature is shown for $\text{Eu}_{0.42}\text{Co}_4\text{Sb}_{11.37}\text{Ge}_{0.5}$ [25]	24
Figure 2.4 The dependence of: (a)the output power and conversion efficiency on the leg length, (b)the thermal stress on the leg length, (c)the output power and conversion efficiency on the side length, and(d) the thermal stress on the side length[49]	31
Figure 2.5 TE generator maximum gained power & EMF during reliability test [54]	35
Figure 2.6 Thermal efficiency curve of the TE collector, compared to same collector without a TEG [61].....	39

Figure 3.1 Schematic view of a thermoelectric power generator and pin configurations	43
Figure 3.2 Geometric configuration of the thermoelectric generator pin	44
Figure 4.1 Validation of present simulations with the previous study [49].....	61
Figure 4.2 The geometric dimensions of TEG module	65
Figure 4.3 The temperature dependence properties of copper plate, (a) thermal conductivity, (b) specific heat, (c) coefficient of linear expansion, and (d) modulus of elasticity [68,69].....	68
Figure 4.4 The temperature dependence properties of Bi ₂ Te ₃ , (a) thermal conductivity, (b) coefficient of linear expansion, and (c) modulus of elasticity.[17,70]	69
Figure 4.5 Model mesh of TE pins used in the simulations.....	71
Figure 4.6 Schematic diagram of TE generator module with [force applied] used in ABAQUS simulation.....	73
Figure 4.7 Heat losses for TE pin.....	74
Figure 5.1 Thermal efficiency variation with R _A (pin area ratio of at hot junction to cold junction), $R_A = A_H / A_L$	77
Figure 5.2 Temperature distribution along the centerline and the maximum stress line for R _A = 0.5.....	79
Figure 5.3 Three-dimensional view of thermoelectric generator with defining Max. Stress line and centerline.	80
Figure 5.4 Cold side temperature with time of heating	81
Figure 5.5 Temperature gradient along the centerline and the maximum stress line for R _A = 0.5.....	82

Figure 5.6 Three-dimensional temperature distribution in the thermoelectric generator for $R_A = 0.5$	83
Figure 5.7 Thermal stress distribution along the centerline and the maximum stress line for $R_A = 0.5$	85
Figure 5.8 Three-dimensional thermal stress distribution in the thermoelectric generator for $R_A = 0.5$	86
Figure 5.9 Three-dimensional thermal stress distribution in the thermoelectric pins for $R_A = 0.5$	86
Figure 5.10 Temperature distribution along the centerline and the maximum stress line for $R_A = 1$	88
Figure 5.11 Temperature gradient distribution along the centerline and the maximum stress line for $R_A = 1$	89
Figure 5.12 Three-dimensional temperature distribution in the thermoelectric generator for $R_A = 1$	90
Figure 5.13 Thermal stress distribution along the centerline and the maximum stress line for $R_A = 1$	91
Figure 5.14 Three-dimensional thermal stress distribution in the thermoelectric generator for $R_A = 1$	92
Figure 5.15 Three-dimensional thermal stress distribution in the thermoelectric pins for $R_A = 1$	92
Figure 5.16 Temperature distribution along the centerline and the maximum stress line for $R_A = 2$	94

Figure 5.17 Temperature gradient distribution along the centerline and the maximum stress line for $R_A = 2$	95
Figure 5.18 Three-dimensional temperature distribution in the thermoelectric generator for $R_A = 2$	96
Figure 5.19 Thermal stress distribution along the centerline and the maximum stress line for $R_A = 2$	97
Figure 5.20 Three-dimensional thermal stress distribution in the thermoelectric generator for $R_A = 2$	98
Figure 5.21 Three-dimensional thermal stress distribution in the thermoelectric pins for $R_A = 2$	98
Figure 5.22 Temperature distribution along the centerline and the maximum stress line for bi-tapered.....	101
Figure 5.23 Temperature gradient distribution along the centerline and the maximum stress line for bi-tapered.....	102
Figure 5.24 Thermal stress distribution along the centerline and the maximum stress line for bi-tapered.....	103
Figure 5.25 Three-dimensional thermal stress distribution in the thermoelectric generator for bi-tapered.....	104
Figure 5.26 Three-dimensional thermal stress distribution in the thermoelectric pins for bi-tapered.....	104
Figure 5.27 One Heating-cooling cycle (time=200 sec).....	107
Figure 5.28 Temperature profile of the maximum stress grid point of five sequential heating-cooling cycles.....	107

Figure 5.29 Thermal stress profile of the maximum stress grid point of five sequential heating-cooling cycles 108

THESIS ABSTRACT (ENGLISH)

NAME: ABDULRAHMAN SALMAN ALMERBATI

**TITLE: THERMAL ANALYSIS OF THERMOELECTRIC POWER
GENERATOR INCLUDING THERMAL STRESSES**

MAJOR FIELD: MECHANICAL ENGINEERING

DATE OF DEGREE: Rajab 1433(H) (MAY 2012)

In recent years, the energy demand is increasing leads to use and utilization of clean energy becomes target of countries all over the world. Thermoelectric generator is one type of clean energy generators which is a solid-state device that converts heat energy into electrical energy through the Seebeck effect. With availability of, heat from different sources such as solar energy and waste energy from systems, thermoelectric research becomes important research topic and researchers investigates efficient means of generating electricity from thermoelectric generators.

One of the important problems with a thermoelectric is development of high thermal stresses due to formation of temperature gradient across the thermoelectric generator. High thermal stress causes device failure through cracks or fractures and these short comings may reduce the efficiency or totally fail the device.

In this thesis work, thermodynamic efficiency and thermal stresses developed in thermoelectric generator are analyzed numerically. The bismuth telluride (Bi_2Te_3) properties are used in simulation. Stress levels in thermoelectric device pins are computed for various pin geometric configurations.

MASTER OF SCIENCE DEGREE

KING FAHD UNIVERSITY OF PETROLEUM AND MINERALS

Dhahran, Saudi Arabia

May 2012

THESIS ABSTRACT (ARABIC)

خلاصة الرسالة

اسم الطالب: عبدالرحمن سلمان المرباطي

عنوان الرسالة: دراسة وتحليل الأداء الحراري لمولدات الطاقة الكهروحرارية بالإضافة إلى دراسة الضغوط

الحرارية الناشئة فيها.

التخصص: الهندسة الميكانيكية

تاريخ التخرج: رجب ١٤٣٣ هـ - مايو ٢٠١٢ م

في السنوات الأخيرة أصبحت الحاجة إلى الطاقة في تزايد، وهذا دفع الدول للبحث عن مصادر جديدة للطاقة النظيفة بهدف الاستفادة من هذه الطاقة. المولدات الكهروحرارية هي نوع من أنواع مولدات الطاقة النظيفة والتي تعتبر من الأجهزة التي لا تحتاج لحركة كي تولد الطاقة، وطريقة عملها أنها تحول الطاقة الحرارية الى طاقة كهربائية بواسطة مبدأ تأثير Seebeck. مع توافر الحرارة من مصادر مختلفة مثل الطاقة الشمسية والحرارة المهدرة من الأنظمة الميكانيكية المختلفة أصبح البحث في مجال الأجهزة الكهروحرارية موضوعاً مهماً للباحثين مما دفعهم للتحقق من فعالية هذه الأجهزة في توليد الكهرباء. واحدة من أهم المشاكل التي تواجه المولدات الكهروحرارية هو نشوء الضغوط الحرارية العالية نظراً لتشكل تدرج في درجة الحرارة عبر هذا أرجل هذه المولدات. تسبب الضغوط الحرارية العالية ضعف للجهاز وذلك من خلال شقوق أو كسور في سطح الجهاز وذلك قد يؤدي إلى تقليل كفاءة الجهاز أو قد يفشله تماماً.

الهدف الرئيسي من هذه الرسالة هو تقديم دراسة للكفاءة الحرارية للمولد الكهروحراري، وكذلك تحليل للضغوط الحرارية الناشئة من ارتفاع حرارة الجهاز أثناء عمله. خواص المادة المستخدمة كمادة كهروحرارية في هذه الدراسة هي البزموت تلوريد bismuth telluride (Bi_2Te_3). كذلك تم حساب مستويات الضغوط الناشئة لعدة أشكال هندسية مختلفة من أرجل الأجهزة الكهروحرارية.

درجة الماجستير في العلوم

جامعة الملك فهد للبترول والمعادن

الظهران ، المملكة العربية السعودية

CHAPTER 1

INTRODUCTION

Nowadays, the increasing of energy prices over the world become one of the important issues and the rising of energy demands turn into crises for most of countries. At the same time, the concern for the environment (clean power systems, without pollution and CO₂ emission) stimulated scientists and engineers to work on clean energy source like increasing the energy harvesting from the sun and improving efficiency of thermoelectric generators. For instance, in the kingdom of Saudi Arabia, the extensive studies were performed in solar power technology to find an alternative source of electric power generation. This is because, the population is growing fast and demand for electricity is rising. In 2004, the population of the kingdom of Saudi Arabia was about 22.7 million and in 2011 it was around 27.1 million. With this growing rate, it is a desire to find another source of energy instead of the conventional one especially, when a large amount of energy is available during all the year from the sun energy.

On the other hand, In United State the electricity has been generated using coal power plants since 1881, but today, they are using different sources of energy that are coal, nuclear, natural gas, hydroelectric, and petroleum with a small amount from solar energy, wind generators, and geothermal sources for generate electric power.

In 2009 [1], coal generation represented 44.9% of total power generation in the United States and solar generation accounted for 3.6% with wind which are renewable sources of energy Figure 1.1

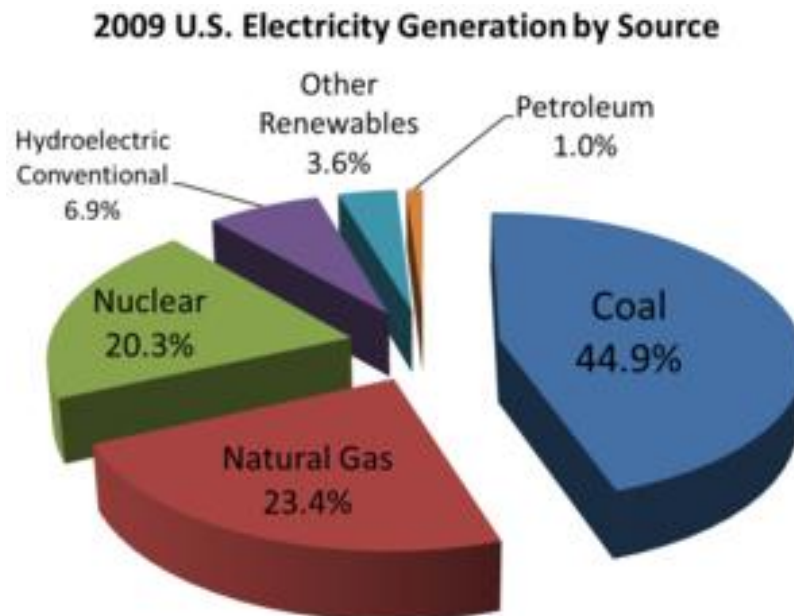


Figure 1.1 Sources of electricity in the U.S. in 2009 [1]

With the availability of huge amount of sun energy (heat), there is a large demand for harvesting this solar energy. The two major ways of harvesting solar energy for electricity are photovoltaic (PV) and solar thermal heat engines.

Specifically, solar thermal power has a large potential for improve meet either by creating efficient selective surfaces to collect the concentrating sun heat or by using an auxiliary device to increase the overall efficiency of the solar power plant which is thermoelectric generators (TEG's).

The focus of this thesis is to analyze the thermoelectric generators through thermodynamics and thermal stress development in the device; including the study for the effect of pin geometric configurations on efficiency and thermal stress distribution.

1.1 History of Thermoelectrics

Before around 200 years, the phenomenon of thermoelectricity was first observed in 1821 by the German academic scientists, Thomas Johann Seebeck who noticed that when a loop was made from wires using two dissimilar metals, a voltage appeared between the junctions of the wires if one junction was hotter than the other [2]. Seebeck realized that a "Thermoelectric Force" induced an electrical current, which by Ampere's law deflects the magnet. Today, such a loop made with dissimilar metals became known as a thermocouple and the phenomenon was named the Seebeck effect. In 1834, a French physicist, Jean Charles Peltier found that an electrical current would produce heating or cooling at the junction of two dissimilar metals. After that, In 1838 Lenz showed that depending on the direction of current flow, heat could be either removed from a junction to freeze water into ice, or by reversing the current, heat can be generated to melt ice and this phenomenon known as the Peltier effect [2] . In additions, the concept of using the sun's heat to power a thermoelectric generator started in 1888 when Edward Weston received his first US patent in solar thermoelectric generators [3]. In 1913, the first experimental results were published by Coblenz [4] in experimental work of solar thermoelectric generations. He found that the efficiency was about 0.008 %. An open circuit produced 0.66 mV per couple, corresponding to a temperature difference of 17°C between hot and cold junctions.

Ioffe [5] developed the modern theory of thermoelectricity using the concept of the figure of merit ZT in 1949. He was one of the first who suggested the use of alloying to reduce lattice thermal conductivity by point defects. After that, Telkes [6] published, in 1954, the first paper on a solar thermoelectric generator which the efficiency was on the order of one percent. She measured 0.63% solar-to-electrical efficiency under no optical concentration using ZnSb p-type elements and doped Bi_2Te_3 n-type elements. When she applied optical concentration to the system, she was able to measure an efficiency of 3.35%. In same year, Goldsmid [7] demonstrated 0 C cooling by using thermoelements based on Bismuth telluride Bi_2Te_3 .

Recently, the interest in thermoelectricity became to the picture again with new ideas from researchers. The aim is to improve ZT ; particularly at small scale of TE structure like micro-scale and Nano-scale of thermoelectric materials. Also, other idea suggests fabricating new classes of complex thermoelectric materials.

1.2 Background of Thermoelectrics

From the thermocouples which are made from metal or metal alloys, the idea of thermoelectric device is come out. Thermocouples generate small voltages, typically tens of microvolt per one degree of temperature difference due to the Seebeck effect. When it connected to a resistive load and its junction is located in a hot or cold environment compared to the ambient, it generates small amounts of electrical power. However, usually, they are used widely in the measurement of temperature or as sensors to control systems such as domestic air conditioning and refrigerators.

In addition, the thermocouple can work in another way of measurements that at the open end of thermocouple, a voltage source can be connected so that an electric current can be driven through the couple. It acts as a heat pump and effectively cools the junction by the Peltier effect. The modified thermocouples made from modern semiconductors which have specific material properties and geometry have been designed specifically to meet the application requirements and having Seebeck coefficients of hundreds of microvolt per degree temperature. The conventional thermocouple is shown in Figure 1.2 used for measurements and as a sensor.

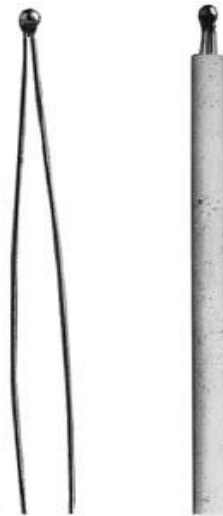


Figure 1.2 Conventional metallic thermocouple [8]

On the other hand, a typical geometry of bulk devices for power generation (thermoelectric generator) or cooling applications (thermoelectric cooler) shown in Figure 1.3 and consist of two pins (thermoelements) of semiconducting material having dimensions in order of millimeters connected at one end with an electrical conducting metal plate.

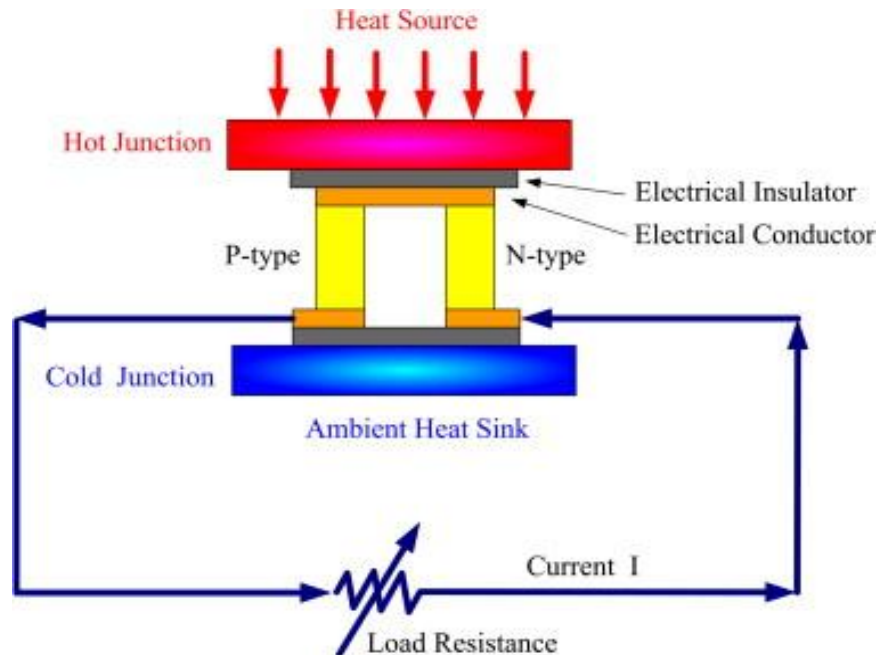


Figure 1.3 Bulk semiconductor thermocouple (thermoelectric element) [9]

The thermoelectric field studies the direct coupling of electricity and heat within a material. Thermoelectric (TE) devices operate as heat engines or heat pumps and they are solid state devices unlike dynamic system which have no moving parts, convert heat (temperature differences) directly into electrical energy, using a phenomenon called the "Seebeck effect" or "thermoelectric effect". These devices use a semiconductor as a material like bismuth telluride (Bi_2Te_3). Thermoelectric devices are made from array of thermoelectric modules connected electrically in series but thermally in parallel as Figure 1.4. However, their efficiency needs to be improved since it has small values comparing with any other conversion technology and its typical efficiencies are between 5% to 10%.

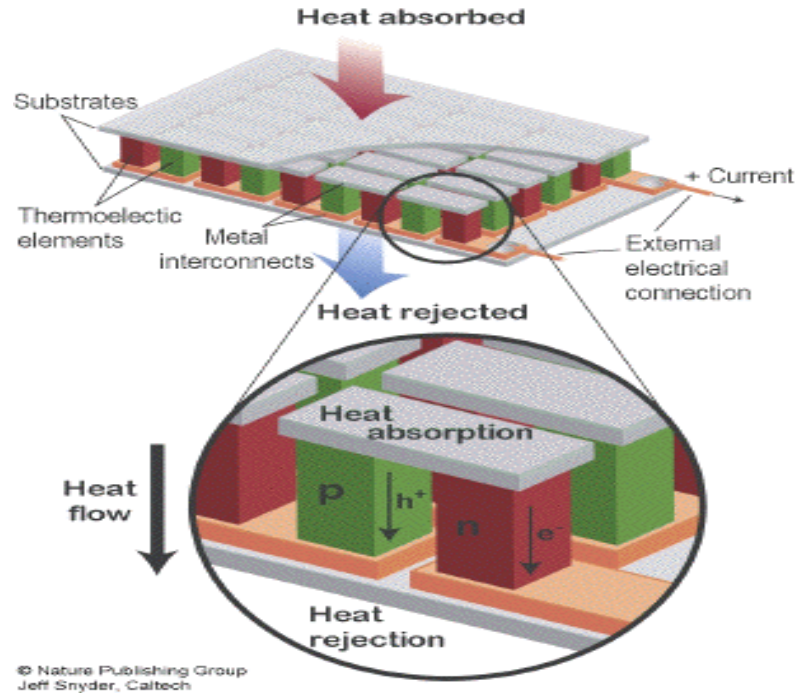


Figure 1.4 Thermoelectric devices consist of TE modules [10]

1.3 Thermoelectric Effects

Early thermocouples were metallic, but many more recently developed thermoelectric devices are made from alternating p-type and n-type semiconductor elements connected by metallic connectors. Semiconductor junctions are common in power generation devices, while metallic junctions are more common in temperature measurement. Charge flows through the n-type element, through a metallic conductor, and passes into the p-type element.

When the heat source provided, the thermoelectric device works as a power generator by Seebeck effect. The heat source drives electrons in the n-type element toward the cooler region, creating a current through the circuit. Holes in the p-type element then flow in the direction of the current. Therefore, thermal energy is converted into electrical energy. In

contrast, if a power source is provided, the thermoelectric device may act as a cooler by the Peltier effect. Electrons in the n-type element move opposite the direction of current and holes in the p-type element will move in the direction of current, both removing heat from one side of the device as shown in Figure 1.5.

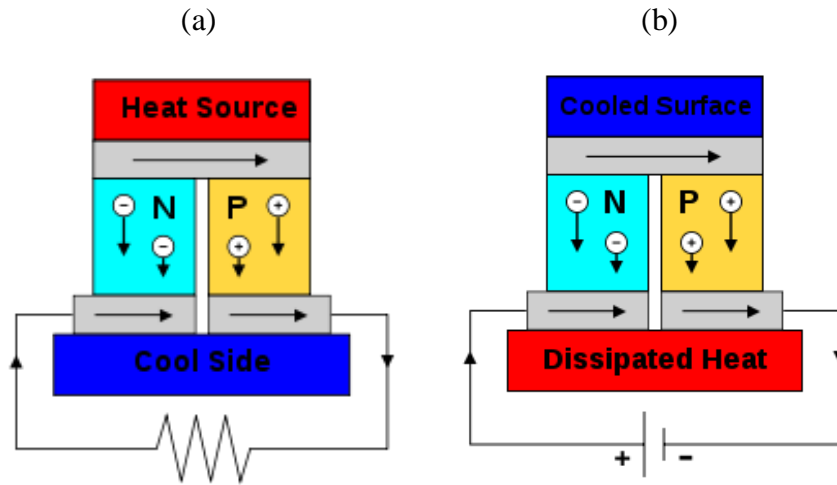


Figure 1.5 The Seebeck circuit configured as (a) Generator. (b) Thermoelectric cooler [9]

1.3.1 Seebeck Effect

The thermoelectric effects can be discussed with reference to the schematic of basic thermocouple circuit with instrument shown in Figure 1.6. The circuit consists of two dissimilar conductors (Metal A, Metal B) that are thermocouple legs or thermoelectric elements. They are connected electrically in series but thermally in parallel. For open circuit (no instrument attached), and the junctions are maintained at different temperatures T_1 and T_2 and $T_1 > T_2$ will result electromotive force EMF. The potential (V) is developed between A and B and given by

$$V = S(T_1 - T_2) \tag{1.3.1}$$

Then, the differential Seebeck coefficient between the two thermoelectric elements S is

$$S = \frac{\Delta V}{\Delta T} \quad (1.3.2)$$

The sign of S is positive if the electromotive force causes a current to flow in a clockwise direction around the thermocouple circuit and measured in $\frac{\text{Volte (V)}}{\text{Kelvin (K)}}$

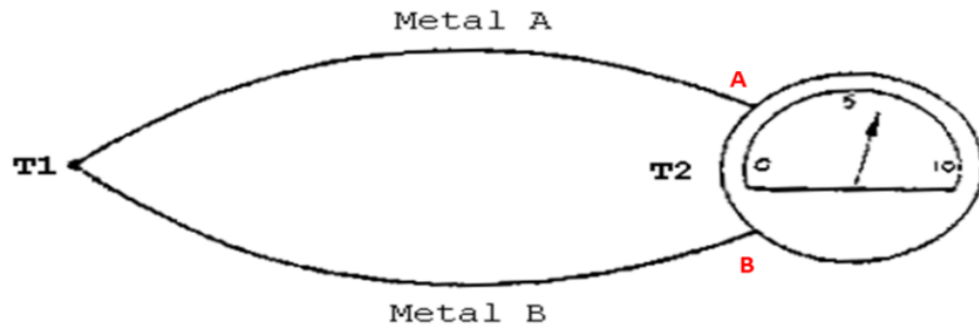


Figure 1.6 Basic thermocouple circuit with instrument

The Seebeck effect is caused by charge-carrier diffusion in the materials. Charge carrier will diffuse when one side of a conductor is at different temperature from the other. Hot carriers diffuse from the hot side to the cold side, since there is a lower density of hot carriers at the cold side of the conductor, and vice versa. If the conductor were left to reach thermodynamic equilibrium, this process would result in heat being distributed evenly throughout the conductor. The movement of heat (in the form of hot charge carriers) from one side to the other is a heat current and the electric current as charge carriers are moving [8].

This means, as the temperature gradient increases in the semiconductor material, the chemical potential will appear through the non-equilibrium carrier concentration. Therefore, when a temperature gradient is forced in a material, a carrier concentration gradient will be present. More charge carriers are generated in the hot side and diffuse to

the cold side creating an internal electric field that resists further carrier diffusion. The steady state electrochemical potential difference between the two sides at different temperature is the known as a Seebeck voltage.

1.3.2 Peltier Effect

Refer to Figure 1.6, for close circuit (with attach instrument), which is external EMF source applied across A and B and a current I flows in a clockwise around the circuit. Then a rate of heat generation Q occurs at one junction between the two elements and a rate of cooling $-Q$ occurs at the other (Figure 1.7). The ratio of Q to I defines the Peltier coefficient π given by

$$\pi = \frac{Q}{I} \quad (1.3.3)$$

Peltier coefficient is positive if T_1 is heated and T_2 is cooled.

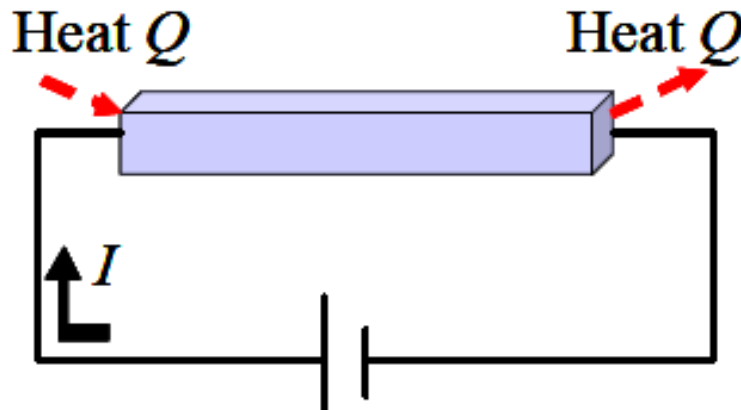


Figure 1.7 Peltier effects: a current flow induces heat flow through the material

1.3.3 Thomson Effect

Thomson effect is one of the thermoelectric effects that relates to the rate of generation of reversible heat Q which came from the current flow along a single element which there is a temperature difference ΔT .

For the small ΔT , the heat generation Q is given by

$$Q = \beta I \Delta T \quad (1.3.4)$$

Where β is Thomson coefficient measured in $\frac{\text{Volte (V)}}{\text{Kelvin (K)}}$.

1.4 Thermoelectric Generation and the Figure of Merit

A thermoelectric device is a heat engine and it follows the laws of thermodynamics. The input is a heat absorbed from hot junction and the output is electric power delivered to the load as shown in Figure 1.8.

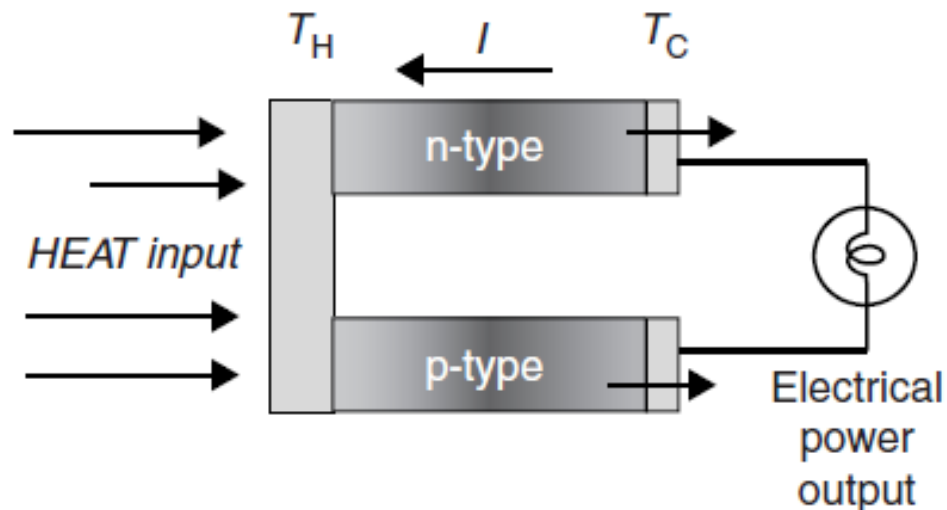


Figure 1.8 Thermoelectric Generation

The efficiency of the ideal thermoelectric generator which there is no heat loss is given by

$$\eta = \frac{\text{electric energy delivered to the load}}{\text{heat absorbed from hot junction}}$$

If it is assumed that the electrical conductivities, thermal conductivities, and Seebeck coefficients of material (a) and material (b) are constant within the thermocouple shown in Figure 1.6, and that the contact resistances at the hot and cold junctions are negligible compared with the sum of the thermocouple resistance, then the efficiency can be expressed as

$$\eta = \frac{I^2 R}{SIT_H + k(T_H - T_C) - \frac{1}{2}I^2 R} \quad (1.4.1)$$

Where k is the thermal conductance of material (a & b) in parallel and R is the series resistance of them. In fact, thermoelectric properties of TE material vary with temperature in both configuration either generation and refrigeration and it should be considered. However, the simple expression found for the efficiency can be employed by using the average values of these material properties for the interest range of temperature.

The conservation energy of thermoelectric device is highly dependent on thermoelectric figure of merit of the TEG thermoelectric generator pin materials which is given by [8]:

$$Z = \frac{S^2 \sigma}{k} \quad (1.4.2)$$

However, in the application the figure of merit is modified to include the average temperature, i.e. ZT

1.5 Thermoelectric Materials

One way to classify the materials is that by considering the electrical conductivity. For instance, metals have high electrical conductivity whereas insulators have very low electric conductivity and at normal conditions are taken as zero and in semiconductors the conductivity takes up in intermediate place between the two. The electrical conductivity is a reflection of the charge carrier concentration.

In addition, the three parameters (Seebeck coefficient, Electric conductivity and thermal conductivity) which formulate the figure-of-merit are functions of carrier concentration. The electrical conductivity increases with increasing the carrier concentration (towards metals) as shown in Figure 1.9 while the Seebeck coefficient decreases. The electronic contribution of the thermal conductivity k_e , which in thermoelectric materials is generally around 1/3 of the total thermal conductivity, also increases with carrier concentration. Clearly from Figure 1.9, figure-of-merit optimizes at the middle area which carrier concentrations is matching to semiconductor materials [11].

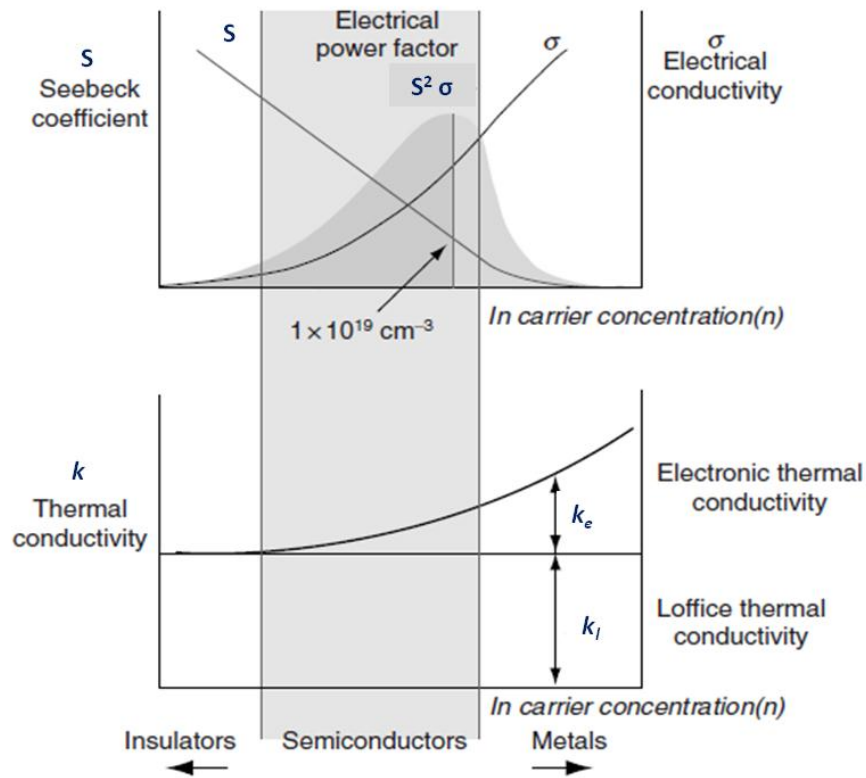


Figure 1.9 Diagram of dependence for the three parameters on free carriers concentration [11]

In recent researches carried out on thermoelectric area, the materials used are semiconductors because of the higher values of figure of merit Z . From the standard thermocouple, it is known that the thermoelectric phenomena happen in all conducting materials but with various values of Z . Also, Z changes with varying temperature and then, a more significant parameter of measuring the TE performance came to the picture which is the dimensionless figure-of-merit ZT where T is absolute or average temperature. However, materials with ZT more than 0.5 are generally considered as thermoelectric materials.

Commercial thermoelectric materials can be divided into three groups depending on the temperature range of operation as shown in Figure 1.10 and Table 1.1. First, Alloys based on bismuth in combinations with antimony, tellurium, and selenium are referred to as low-temperature materials. These are the materials universally used in TE refrigeration. Second, the intermediate temperature range materials which are usually based on lead telluride. Third, thermoelements employed at highest temperatures are fabricated from silicon germanium alloys [12-13].

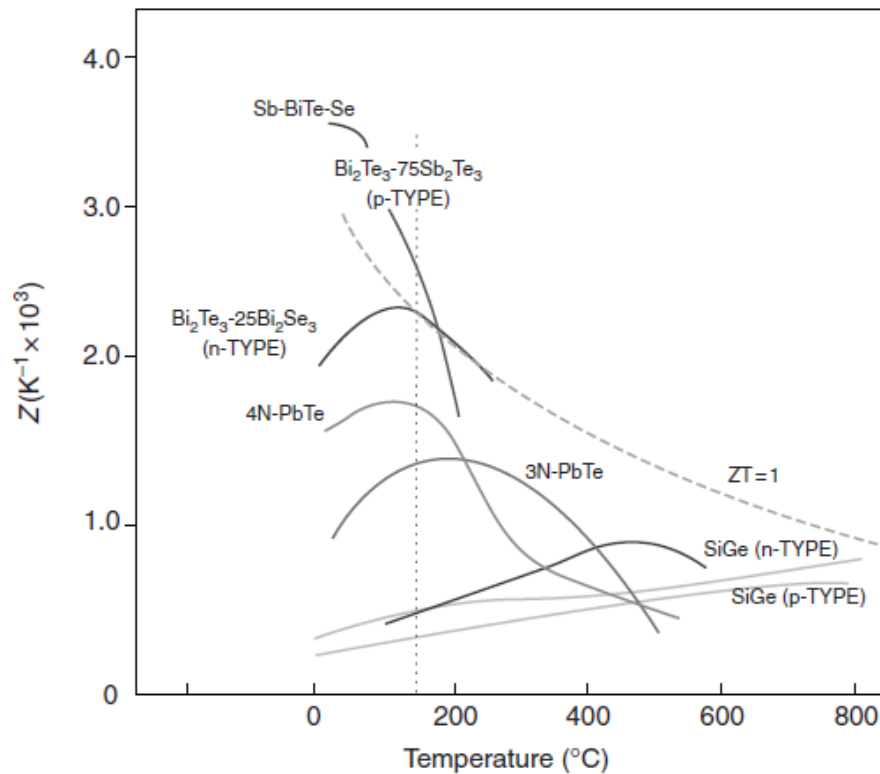


Figure 1.10 Figure of merit of commercial thermoelectric materials [12]

Table 1.1 Classes of thermoelectric materials

	Low-temp. Materials	Intermediate-temp. Materials	High-temp. Materials
Basic Material	Bismuth	Lead telluride	Silicon germanium
Temp. Range	Up to around 500 K	500K – 850 K	Up to 1300 K

As mentioned in section 1.4, the dimensionless figure-of-merit, ZT is the power factor $S^2\sigma T$, over the total thermal conductivity k , which is equal to k_e plus k_l . The electronic component k_e is related to the electrical conductivity but the lattice component is an independent quantity. Bismuth telluride has one of the highest values of the power factor at normal temperatures and a low value for the lattice conductivity [14]. They found that the compounds with empty spaces in their crystal structures can have very low values of the lattice conductivity. The empty spaces may be filled by loosely bound atoms, which are known as **rattlers** and these systems are named as PGEC (phonon glass – electron crystal) implying that these have a lattice conductivity that is characteristic of an amorphous material combined with the typical electronic properties of a crystal such as, skutterudites and clathrates.

Among many potential TE materials, skutterudite compounds have been identified as good candidate [15-16].

1.6 Scope of the work

A thermoelectric power generator (TEG) operates between high and low temperature sources, temperature distribution in thermoelectric generator becomes important. Since, increasing thermal conductivity reduces the figure of merit (ZT), thermal efficiency of the device is affected by temperature distribution over the TEG pins. In addition, due to large temperature difference between the hot and cold heat sources and small device height result in development of high temperature gradients over the pins. This, in turn, causes the formation of high thermal stress field in the TE pins while reducing life span of the pins. The geometric configuration of TEG pins influences temperature and stress field developed in the TE pins.

In the open literature, no significant contribution on pin geometric configuration and its effects on thermal performance of thermoelectric device is observed. Therefore, in the present thesis, thermal analysis of thermoelectric generator including temperature and stress fields is carried out. The study is extended to include the influence of pin geometry on thermodynamics efficiency of the device and thermal stress development in the TE pins.

1.7 Thesis outline

The first chapter of the thesis deals with the introduction of thermoelectric devices, thermoelectric effects, thermoelectric materials and historical development as well as the scope of the work.

Chapter 2 presents a literature survey relevant to thermoelectric such as fabrication of new TE materials, producing TE thin films and enhancement of TE performance.

In chapter 3, the mathematical analysis related to thermodynamics, heat transfer, and thermal stress aspects of TE device are included. In addition, the solution methodology for governing equation is introduced.

In Chapter 4, the numerical method used for solving the thermal and stress problem of thermoelectric generator module is discussed. The validation of ABAQUS code used in this thesis is also presented.

In chapter 5, findings are presented and discussed in details.

In the last chapter, that this is chapter 6, conclusions derived from the results of the work are presented together with recommendations for the future research studies in thesis research area.

CHAPTER 2

LITERATURE REVIEW

Several efforts have been made to develop the materials and structures with high efficient cooling and energy conversation systems. However, a few works studied the influence of thermoelectric effects on the TE stress. Since, the increase in Figure of merit ZT leads directly to improvement in the cooling efficiency of Peltier modules and in the electric generation efficiency of TE generators, the direction of researches is to increase the figure of merit ZT by various techniques.

This chapter reviews the work carried out recently over the thermoelectric development. First, a literature of thermoelectric materials and small scale material structure contribution is presented and the efforts done to improve the figure of merit ZT . Next, an overview over the research related thermodynamics efficiency of thermoelectric devices. Finally, a few investigations in thermo-mechanical and efficiency enhancement of thermoelectric devices are presented.

2.1 Thermoelectric Material and Small Scale Structures

A Significant work has been done on synthesizing new TE materials and fabricating its material structures with improved thermoelectric performance.

Zhao et al. [17] fabricated n-type Bi_2Te_3 with different volume of nano-SiC particles thermoelectric materials by mechanical alloying (MA) and spark plasma sintering (SPS) method. They found an increase in Seebeck coefficient and decrease in electrical and thermal conductivity. They demonstrated an improvement in figure of merit ZT from 0.99 for typical Bi_2Te_3 sample to 1.04. Also, there have been some improvements in ZT like 1.4 in p-type nanocrystalline BiSbTe bulk alloy [18], but even their values are not sufficient to dramatically improve the cooling or energy conversion efficiencies.

Polvani et al. [19] reported a large increase in the thermoelectric power of p-doped antimony bismuth telluride alloys upon pressure tuning under non-hydrostatic compression conditions. Their results showed the value of figure of merit is more than 2.2 with measurements of the electrical conductivity and an upper bound estimated for the thermal conductivity under pressure. They suggested an explanation for the observed behavior that to reproduce TE material at ambient pressure. Hsu et al. [20] measured the thermoelectric properties of bulk $\text{AgPb}_{10}\text{SbTe}_{12}$ and $\text{AgPb}_{18}\text{SbTe}_{20}$. They obtained that the figure of merit ZT of 2.2 at ($T=800$ K) for $\text{AgPb}_{18}\text{SbTe}_{20}$ material.

Koukharenko et al. [21] fabricated bismuth telluride materials Bi_2Te_3 by ultra-rapid quenching and they obtained foils with a thickness varying from 10 to 60 μm . They studied the influence of quenching temperature and heat treatment on the Seebeck coefficient and also the variation of thermoelectric properties with temperature. Their results showed that Bi_2Te_3 foils are degenerate semiconductors of n-type. They concluded that it is now necessary to optimize melt composition to obtain well doped materials in order to improve the thermoelectric properties of Bi_2Te_3 foils.

Zhu et al. [22] synthesized lead telluride (PbTe) by high pressure and high temperature method. They indicated both the thermopower and the electric resistivity drop with increasing synthesis pressure and the thermal conductivities of the samples synthesized by high pressure had lower values than that of samples synthesized at ambient pressure. They found that the value of the dimensionless thermoelectric figure of merit ZT was enhanced nearly 20 times at room temperature and approximately equal to the value of Bi_2Te_3 . The value of ZT was over 0.87 as shown in Figure 2.1. They concluded that the technique of high pressure is a useful tool to obtain materials of improved properties, and highly efficient TE materials may be expected.

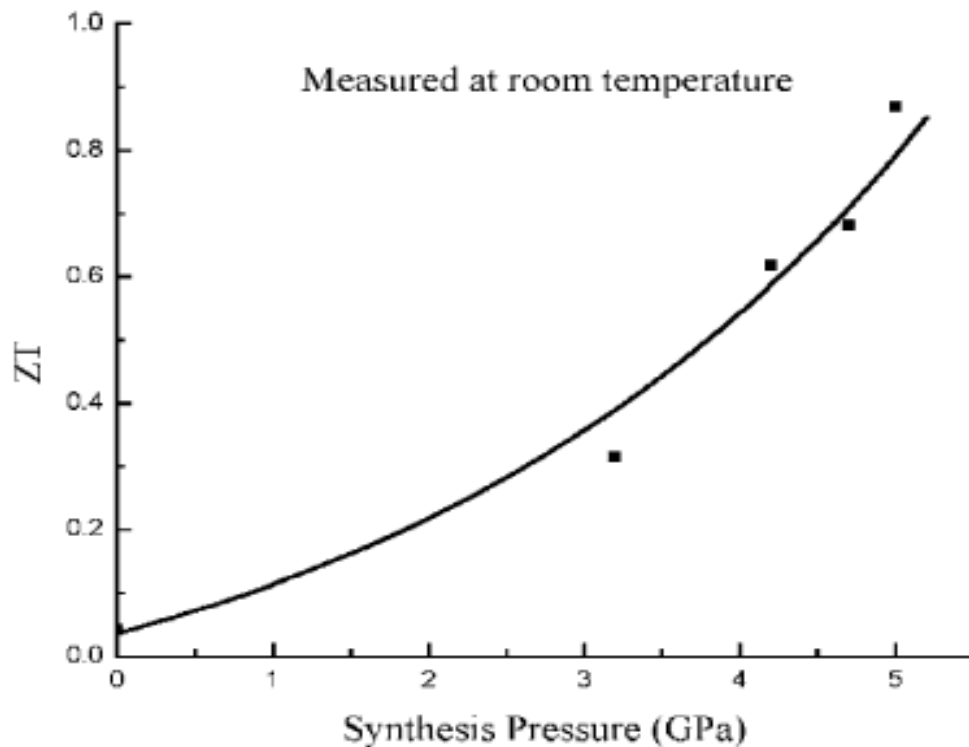


Figure 2.1 ZT versus the synthesis pressure (measured at room temperature) [22]

Song et al. [23] prepared a solid solutions of $\text{Mg}_2\text{Si}_{1-x}\text{Sn}_x$ (with $x = 0, 0.2, 0.4, 0.6, 0.8, 1.0$) from elemental powder mixture as TE materials by bulk mechanical alloying (BMA) with combination of hot pressing. They optimized the hot pressing condition in order to obtain higher figure of merit. The temperature dependence of electrical conductivity, Seebeck coefficient and thermal conductivity were measured from the room temperature up to 700 K. They obtained a maximum figure of merit of 0.13 at 653 K from different samples with nominal compositions of $\text{Mg}_2\text{Si}_{0.4}\text{Sn}_{0.6}$ and Mg_2Si . They concluded that the TE properties of $\text{Mg}_2\text{Si}_{1-x}\text{Sn}_x$ were sensitive to the tin concentration and the figure of merit at room temperature increased with increasing the temperature and pressure of hot pressing.

Chen et al. [24] experimentally investigated the high temperature TE transport properties of p-type Yb-filled Fe-compensated skutterudite $\text{Yb}_x\text{Fe}_y\text{Co}_{4-y}\text{Sb}_{12}$. They presented that the lattice thermal conductivity was significantly reduced to the level near the theoretical limit upon Yb filling and Fe substitution for Co also discouraged the lattice thermal conductivity through additional phonon scattering mechanisms. They found that the highest value of ZT was 0.6 for $\text{Yb}_{0.6}\text{Fe}_2\text{Co}_2\text{Sb}_{12}$ ($x=0.6$) at temperature of 782 K and 0.57 for $\text{YbFe}_4\text{Sb}_{12}$ ($x=1$) at temperature of 780 K as shown in Figure 2.2.

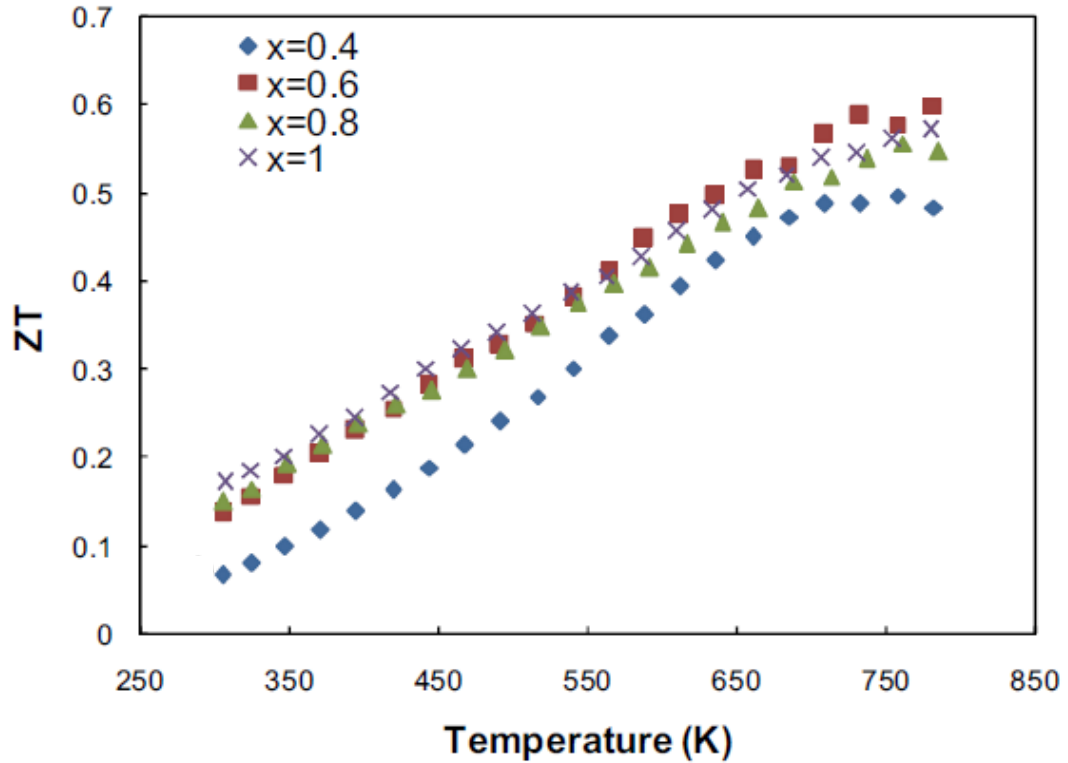


Figure 2.2 ZT as a function of temperature of $\text{Yb}_x\text{Fe}_y\text{Co}_{4-y}\text{Sb}_{12}$ [24]

Lamberton et al. [25] measured the electrical resistivity, thermopower, thermal conductivity, and Hall coefficient of polycrystalline Eu-doped CoSb_3 -based skutterudites with compositions $\text{Eu}_{0.2}\text{Co}_4\text{Sb}_{12}$, $\text{Eu}_{0.43}\text{Co}_4\text{Sb}_{11.59}\text{Ge}_{0.31}$, and $\text{Eu}_{0.42}\text{Co}_4\text{Sb}_{11.37}\text{Ge}_{0.50}$. They observed that the value of ZT for a Eu-filled skutterudite at 700 K more than 1.1 as shown in following Figure 2.3. The figure of merit, ZT versus temperature is shown for $\text{Eu}_{0.42}\text{Co}_4\text{Sb}_{11.37}\text{Ge}_{0.5}$ sample. It is clear that at room temperature the value of ZT was measured of 0.26, and it is approximately above 1.1 at 675 K. In addition, Figure 2.3 shows that the profile of total thermal conductivity k ($k_l + k_e$) with temperature inside the small box. Also, Nolas et al. [26] found similar values for different type of skutterudites and clathrates.

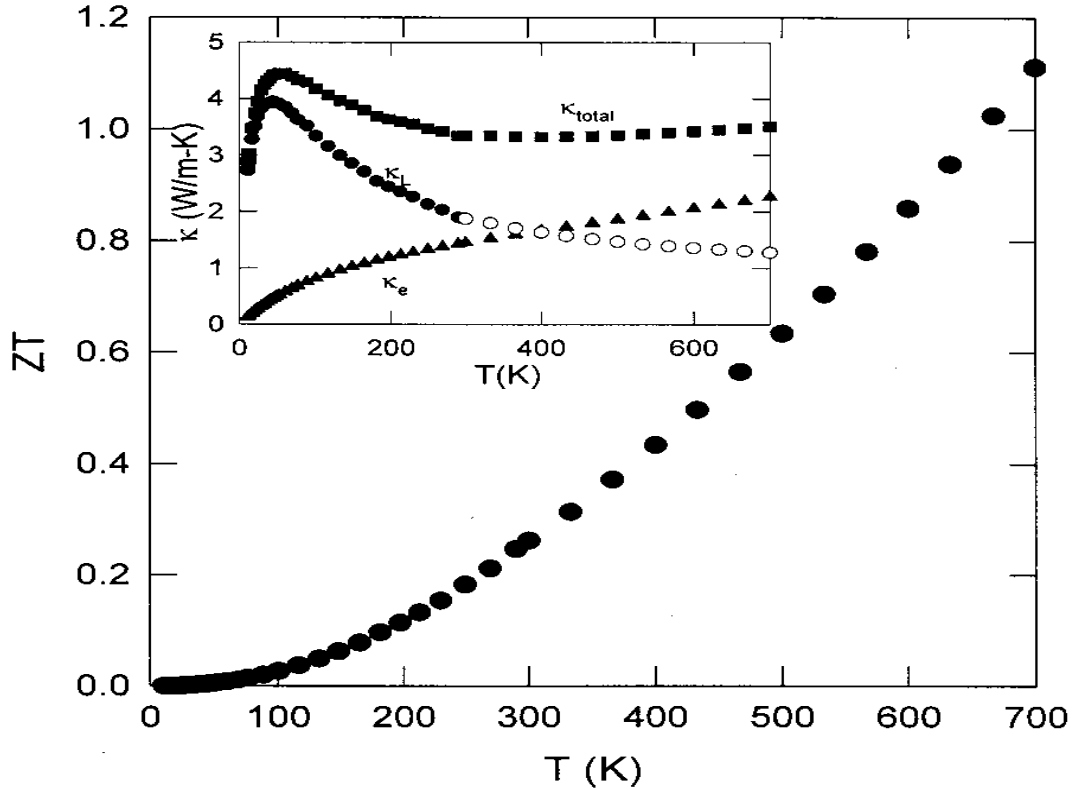


Figure 2.3 ZT vs. temperature is shown for $\text{Eu}_{0.42}\text{Co}_4\text{Sb}_{11.37}\text{Ge}_{0.5}$ [25]

Even though these materials have lower thermal conductivity than in bismuth telluride alloys, they have smaller power factor comparing with bismuth telluride at room temperature. The idea of choosing bismuth telluride as a thermoelectric material came from that, the lattice thermal conductivity decreased with increasing mean atomic weight which was shown by Ioffe [27]. Also, he suggested that the ratio of carrier mobility to lattice conductivity would increase with increasing the atomic weight.

While the researches of fabricating a new compound of TE materials are in development, there are also a number of attempts to produce thermoelectric materials in which at least one of the dimensions is not much greater than the lattice constant. These efforts should leads improving the figure-of-merit by reducing the lattice thermal conductivity. During

the past decade material scientists have been confident that low-dimensional structures such as **quantum wells** in which materials are so thin as to be essentially of two dimensions , **quantum wires** in which extremely small cross-section and considered to be of one dimension, **quantum dots** which are quantum confined in all directions and **superlattices** which is a multiple-layered structure of quantum wells will provide a direction for achieving significantly improved thermoelectric figures-of-merit. The expectation is that the reduced dimensions of these structures will result in an increase in phonon interface scattering and a consequent reduction in lattice thermal conductivity. Consequently, there are significant improvements in the thermoelectric figure of merit ZT was made mainly on quantum well and quantum wire superlattices [28-30].

Harman et al. [31] produced an n-type quantum dot superlattice structures based on PbSeTe material and experimentally investigated for application in thermoelectric. They demonstrated an improvement in cooling values relative to the conventional bulk $(\text{Bi,Sb})_2(\text{Se,Te})_3$ thermoelectric device. They used the n-type film in a one leg of thermoelectric device test setup, which cooled the cold junction 43.7 K below the room temperature hot junction temperature of 299.7 K. The TE device was consisted of a substrate, bulk slab of nanostructured PbSeTe/PbTe as the n-type leg with a dimension of 0.1 millimeter in thickness, 10millimeters in width, and 5 millimeters in length and a metal wire as the p-type leg. Their measurements indicated the attainment of device ZT and it was in range of 1.3 to 1.6 at room temperature.

Venkatasubramanian et al. [32] reported thin-film thermoelectric materials with a significant enhancement in ZT at temperature of 300 K compared with bulk Bi_2Te_3 alloys. They found that the figure of merit of p-type superlattice based on Bi_2Te_3 and Sb_2Te_3 is

equal to around 2.4. The improvement which they achieved is by controlling the transport of phonons and electrons in the superlattices.

Ghoshal et al [33] have approached the problem of making thermoelectric nanostructures in a different way. They described a thermoelectric device structure that limited to the thermal gradients and electric fields at the boundaries of the cold junction, and utilized the reduction of thermal conductivity at the interfaces and the poor electron-phonon coupling at the junctions. They found the value of ZT in the range between 1.4 and 1.7 compared with 0.84 for commercial modules made from the same materials. Their thermoelectric cooler was based on a p-type $\text{Bi}_{0.5}\text{Sb}_{1.5}\text{Te}_3$ and an n-type $\text{Bi}_2\text{Te}_{2.9}\text{Se}_{0.1}$ material. Their work demonstrated that the figure-of-merit can be improved without resort to the usual techniques for producing nanostructures.

Various techniques have been attempted to prepare the bismuth telluride thin films that were used in thermoelectric micro-cooler, such as pulsed laser deposition [34], flash evaporation [35], ion-beam sputtering at room temperature [36,37], sputter-deposition at room temperature [38].

Giani et al. [39] have grown for the first time thin films of Bi_2Te_3 by metal organic chemical vapor deposition using trimethyl bismuth and dimethyl tellurium as classic organ-metallic sources. Miyazaki and Kajitani [40] prepared bismuth telluride films electrochemically by depositing from solutions of Bi_2O_3 and TeO_2 in diluted HNO_3 (pH = 0.50) onto Ti sheet working electrodes at 293 K.

Zou et al. [41] deposited both n- and p-type bismuth telluride thin films by co-evaporator on glass substrates.

However, in general, the thermoelectric properties of thin film Bi_2Te_3 are poor compared with bulk Bi_2Te_3 [38] and this is because of the difficulties in controlling the composition and the defects in thin films. Then, smaller dimensions structure of thermoelectric materials that are Bi-Te thin films become into the approach of researchers because of their better potential in thermoelectric properties with higher thermoelectric figure of merit ZT due to their stronger quantum potential compared with bulk materials [36].

2.2 Thermodynamics of TE Devices

The basic knowledge for thermodynamics of TE device is reviewed in this section which is represented the direct coupling between heat transfer and electric current by the Seebeck coefficient.

Onsager [42] described the set of general linear equations, often called the thermodynamic equations of motion, which gave general description of flows of particles or of energy as being driven by various thermodynamic forces. He observed that, the flow is directly proportional to the corresponding force that drives it. Common examples cited include heat transfer where the vector flow of energy is proportional to the temperature gradient, or Ohm's law in which the electrical current density is proportional to the voltage gradient. Onsager suggested that each of the flows in a given steady-state system is proportional to the sum of all forces acting on the system.

Domenicali [43] stated the general equations for inhomogeneous isotropic media from the theory of irreversible thermodynamics and by considering the charge carrier to be an electron. He described the three fundamental relations of Thermoelectrics. The first

equation described the entropy current density as the sum of the transport entropy and the heat flux entropy. Secondly, the total energy current density is the sum of the particle current energy and the heat flux due to the temperature gradient. The electrochemical potential consists of two parts that are chemical part and electrical part.

The thermodynamics analysis of thermoelectric generator was also investigated by Lampinen [44]. He considered the TE generator as a heat engine cycle process and derived the Kelvin relations for the TE circuit from the energy balance and from the second law without using reversibility or equilibrium assumptions. Also, he derived a new formula for the thermal efficiency of the TE generator, including the Thomson heat effect, and an equation for maximum efficiency.

Kassas [45] also, carried out thermodynamic analysis of a thermoelectric device. He considered the thermoelectric diode and electronic and he computed the Carnot efficiency of the device. He found that increasing emitter temperature increases the Carnot efficiency of the thermoelectric device in which, the diode power intensity and electronic efficiency reduce. He also presented that the second law efficiency increases with emitter to collector temperature ratio and reduces with increasing collector temperature due to increase in collector current flow.

Chen et al. [46] established the differential equations governing the temperature field inside the device operated between two heat reservoirs by using non-equilibrium thermodynamics by considering the effect of Peltier, Fourier, Joule and Thomson heat. They used the performance of TE device as a heat pump or refrigerator. They derived

expressions for the coefficient of performance COP and the rate of heat pumping with analyzing the effect of the Thomson heat on them.

Yamashita [47] constructed new thermal rate equations by introducing the temperature dependences of the electrical resistivity and thermal conductivity of the TE materials on the assumption that they vary linearly with temperature. He formulated the relative energy conversion efficiency, which is the ratio of energy conversion efficiency derived from the new thermal rate equations and conventional one, for a single TE element by approximate analysis. He applied his equations to Si–Ge alloys and he found that the degree of contribution from both parameters to the relative efficiency was a little lower than 1% at the temperature difference of 600 K. However, the relative efficiency could be increased to about 10 % when the temperature dependence of thermal conductivity was increased to become equal to that of electric resistivity. Finally, He concluded that the temperature dependence of the electrical resistivity and thermal conductivity significantly influences the efficiency of the thermoelectric generator.

2.3 Thermo-mechanical Studies and TE performance

Few works have been made to analyze the thermo-mechanical performance of TE generator modules and investigate the influence of various structure parameters on the TE device

Li et al. [48] carried out the finite element analysis FEA for thermal, electricity, and stress coupling effects of TEG device. Different copper pad thicknesses (100um, 500um, and 1000um) under different temperature differences were considered to investigate the

geometry effect on the maximum power output and maximum Von Mises stress. Their results showed that, at the same temperature difference, the maximum power output was almost keeping the same value with different pad thickness and this leads to that the copper pad thickness was not affected the output power. It might because the copper is a well electrical conducted material that makes lower electric resistance for the current passing through the device.

By contrast, the maximum Von Mises stress was getting higher when the pad thickness became thicker under each temperature difference. The maximum Von Mises stress occurred on the contact surface between copper pad and Aluminum nitride (AlN) substrate, and they clarified that is because of the large coefficient of thermal expansion CTE mismatch between the copper pad and the substrate, especially in the higher temperature case.

GAO et al. [49] presented the thermal stress distribution of a TE module based on the anisotropic mechanical properties and thermoelectric properties of hot pressed material which is Bismuth Telluride Bi_2Te_3 . The effect of the structure parameters, including the length of TE leg and the side length of TE leg, were studied and the optimum dimensions were defined.

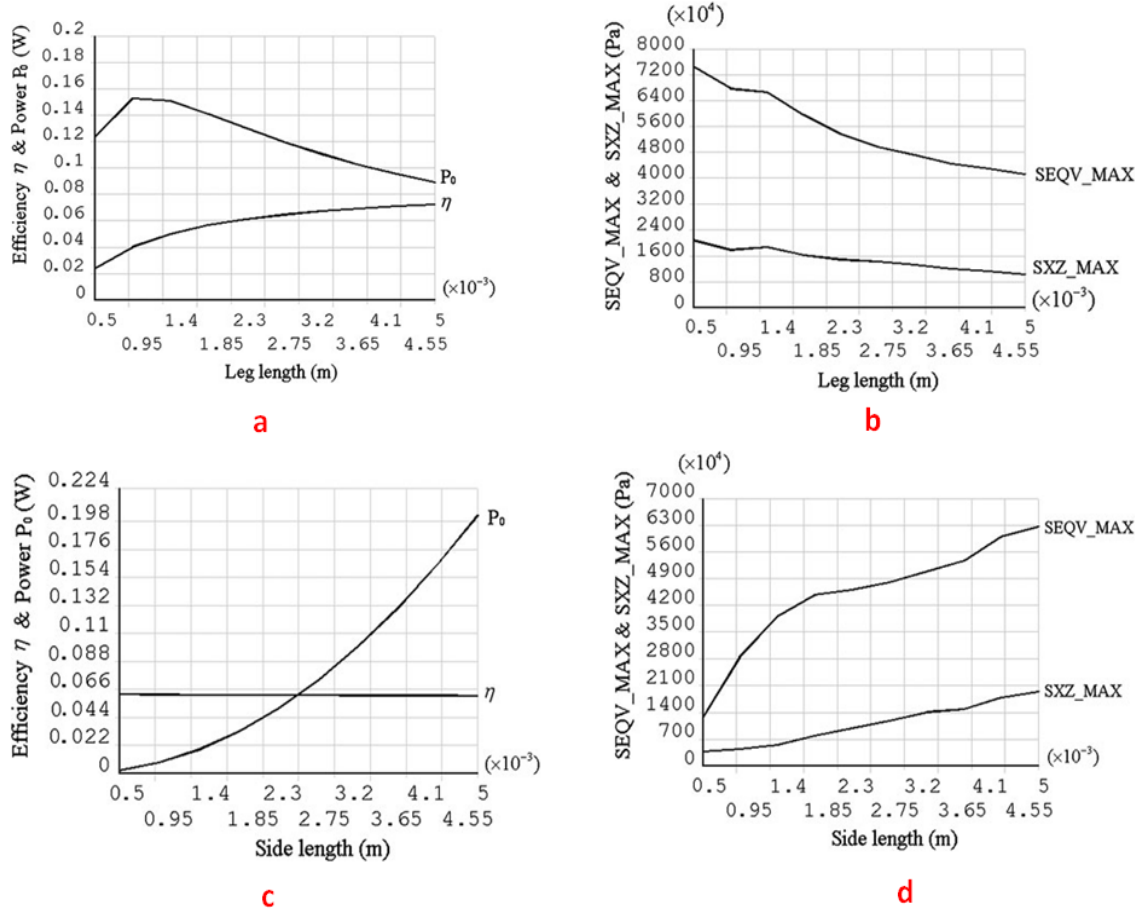


Figure 2.4 The dependence of: (a)the output power and conversion efficiency on the leg length, (b)the thermal stress on the leg length, (c)the output power and conversion efficiency on the side length, and(d) the thermal stress on the side length[49]

They presented that the results that the output power decreased with increasing leg length but increased with increasing cross section side length, while the conversion efficiency increased with increasing leg length but keeps almost constantly with increasing cross-section side length as shown in Figure 2.4. Moreover, both the shear stress and von Mises stress initially decreased with increasing leg length, but the shear stress changed slowly with increasing cross-section side length, while the von Mises stress changes more

significantly with the side length. They suggested that to reduce the possibility of damage along the cleavage plane due to large shear stress, considering the influence of TE leg length and side length, the optimum design of TE with leg length equal to 2.5 mm and side length equal to 4 mm.

Hori et al. [50] performed a heat cycle test in order to analyze the thermo-mechanical performance of modules of three different cross sectional areas of TE legs and to study time dependence of electrical properties. They modeled the three TE legs with constant length of 2.5mm but various cross sectional dimension that $3.5 \times 3.5 \text{mm}^2$, $3 \times 3 \text{mm}^2$, and $2 \times 2 \text{mm}^2$. They found that by increasing the heat cycles, the internal electrical resistance was increased also, and that caused by the poor contact between a thermoelectric element and a copper electrode due to the fall of the solder at the contact. Also, there was a decline in the generation performance of a modules caused by the increase in the internal electrical resistance of the module. Their FEM analysis indicated a possibility of material failure in the hot side solder part and element part.

Huang et al. [51] performed a thermal analysis of thin-film thermoelectric cooler under the effect of the Thomson heating, the Joule heating and Fourier heat conduction. The condition that Thomson coefficient is constant was assumed instead of a Seebeck coefficient. They demonstrated that the conduction heat and the Joule's heat flowing to the cold junction could be considerably reduced by providing the Thomson coefficient of the p-type layer is greater than that of the n-type. A larger maximum temperature difference could be achieved and a larger maximum heat load could be allowed consequently. In addition, they analyzed the thermal stresses, including normal stresses and shear stresses, developed in the layered structure using the non-coupled thermal

elastic theory. They defined the normal-stress distributions within the thermoelectric element and the shear stress distributions between adjacent layers which consist of the supporting membrane and the p-type and n-type thermoelectric films separated by an insulating layer. They presented an improvement in thermal performance by the Thomson effect but the shear stress is proportional to the temperature gradient and the larger the heterogeneity in the thermal expansion coefficients between the adjacent materials, this means the shear stress is increased with Thomson coefficient. The stresses could not be greater than the yielding stress of the material in order to be in safe side form failure.

The results of this paper provided a preliminary understanding to judge whether the thin-film structure is destroyed by the thermal stresses or not, especially by the shear stresses between adjacent layers.

Thermo-mechanical modeling of large area TE generators was carried out by Turenne et al. [52]. They simulated numerically the behavior of TE modules under steady state operation with the help of finite element analysis of large modules ($30 \times 30 \text{ mm}^2$ and $40 \times 40 \text{ mm}^2$). The plastic deformation of the soldering alloys was shown to reduce the amount of stress in the legs. They indicated that the maximum stress was increased in the thermoelectric device close to the edge of the pins. They concluded that the fabrication of thinner modules leading to higher temperature gradients and this would result higher stress levels on in the TE pins, particularly at the pin corners of hot side. Also, the solder always undergoes plastic deformation in simulated modules with legs shorter than 2.5 mm, where the stress became higher than the yield strength of the soldering alloy. This was considered convenient and useful to relax the stress in the TE alloys legs.

Yang et al. [53] simulated hot extrusion process of Bi_2Te_3 material by FEM tools. The influence of extrusion ratio, the ratio between the square of pre-deformation diameter to the square of deformed diameter, and the extrusion angle were analyzed. They found that the friction condition between the extrusion die and the sample had large effect on the surface stress state of the sample, making the surface region under more tension stress, therefore increased the possibility of surface crack. Also, the extrusion angle showed effect on the deformation, with longer or larger regions of deformation in the case of low extrusion angle, which means lower deformation rate and would cause less micro-holes. Then n-type Bi_2Te_3 based materials were also hot extruded under different experiment conditions, and effect of extrusion parameters on microstructure and thermoelectric properties of the materials was studied. They showed that $(0\ 0\ 1)$ was formed in the hot extruded samples as favored orientation microstructure and an agreement between the experimental results with the results of FEM analysis.

Hatzikraniotis et al. [54] investigated experimentally the long-term performance and stability of a commercially available TEG under temperature and power cycling. A sequence of heating cycles applied to the TE module, which the hot side temperature was 200 C and cooling for long times which was 3000 hours in order to measure the changes in the TEG's performance. They presented the TE generators maximum gained power and the electromotive force EMF , which is the open-circuit voltage of the TE when the maximum temperature was reached, during the efficiency test as shown in Figure 2.5.

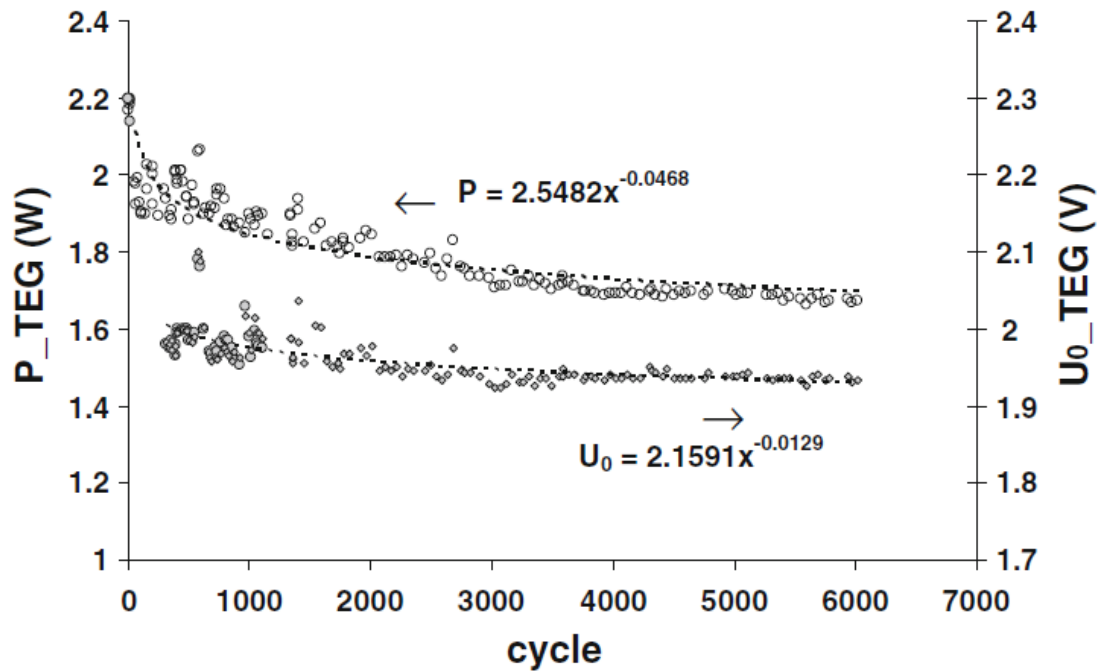


Figure 2.5 TE generator maximum gained power & EMF during reliability test [54]

As shown, both TE power and EMF decreased with thermal cycling and these are proportional to the Seebeck coefficient, and from that they evaluated the change in the Seebeck coefficient of the material. They observed a total drop of about 14% in gained power and 3.3% in EMF to 6000 cycles. In addition, they used SEM to study the microstructure of the material and they found a formation of micro cracks in the vicinity of the leg-solder interface caused by the high temperature since the increase in material resistivity cannot be excluded. Then, a reduction of 6.6 % in the average leg thermal conductivity, a drop about 3.8% in Seebeck coefficient and an increase of 16.1% in electrical resistivity due to that micro cracks was observed.

Ravi et al. [55] investigated the thermal expansion of high temperature TE materials. Since the thermal expansion coefficient is a considerable factor in the thermo-mechanical analysis of TE devices, they measured and presented thermal expansion data for several

advanced TE materials. They carried out in details the stress analysis of various interfaces in advanced thermocouples for integration into advanced TE generators by using Finite-element tools. A numerical example was showed in this paper indicated that the high sensitivity of interfacial stresses to thermal expansion coefficients of adjacent materials and by knowing that the thermally matched system leads to reduced interfacial stresses and less risk of in interface fracture of the TE device. From this study, it is clear that thermal expansion coefficient of the TE materials is the critical parameter influencing stress levels in the device.

Number of attempts concern with the modeling of thermoelectric generates and investigating the TE performances are reviewed and presented.

Antonova and Looman [56] introduced a new set of ANSYS coupled-field elements that allowed users to analyze the efficiently of thermoelectric devices accurately. They considered Joule heating, Seebeck, Peltier, and Thomson effects for the thermoelectric generator and they simulated these tools for steady state and transient cases.

A numerical analysis was conducted by Sisman and Yavuz [57] of the effect of joule heat losses on the efficiency of thermoelectric power cycle by comparing it with conventional DC power cycle. The presented that the typical maximum value of Z is $1 \times 10^{-3} \text{ K}^{-1}$ and the maximum operating temperature difference is about 800 K for TE device based on n-type SiGe/GaP material.

Ozkaynak [58] studied the external and internal irreversible heat and determined the maximum power and thermal efficiency at maximum power output for TE generator.

Chen et al. [59] investigated the characteristics of a multi-element thermoelectric generator with the irreversibility of finite-rate heat transfer, Joule heat inside the TE device, and the heat leak through the TE legs. Then, they derived expressions for the power output and efficiency of thermoelectric generators that composed of multi-elements. The heat transfer irreversibility in the heat exchanger between the TE generator and the heat reservoir was considered. The effect of heat transfer and the number of TE elements were analyzed. The results of this paper showed that the heat transfer irreversibility affected the performance of TE generator and it is important to consider this effect in TE the analysis. Also, the number of TE elements affects the performance for the real generator composed of multi-element. Chen and his group suggested that the performance optimization of TE generator could be carried, including two aspects, i.e., the internal optimization and the external optimization. Internal optimization dealing with optimizes the TE leg size of each element to minimize the heat conductance of heat exchangers between the hot and cold junctions of the TE generator and their respective reservoirs. External optimization is to optimize the external load and internal electrical resistance.

An efficiency analysis of topping cycle which consists of conventional solar concentration power plant with TE generators placed on the heat collector elements was conducted by Sahin et al. [60]. They carried out numerical simulations to predict the flow field and temperature field of the working fluid in the thermal system. The overall efficiency ratio due to the thermal systems with and without the presence of the thermoelectric power generators was also examined for various operating parameters. A comparison between the two systems with and without TE generator was presented.

They found that, for a certain combination of operating and TE device parameters, thermal efficiency of the topping cycle became slightly higher than that of the same system without the presence of the TE generators.

Rockendorf et al. [61] investigated two different principles of thermoelectric cogeneration solar collectors. The first principle was concerning with the thermoelectric collector TEC delivers electricity indirectly by first producing heat and then generating electricity by means of TE generator. The second principle was focused on the photovoltaic-hybrid collector PVHC uses photovoltaic cells, which are cooled by a liquid heat-transfer medium. The characteristics of both collector types are described. Simulation modules have been developed in order to simulate their behavior in typical domestic hot-water systems. They found that the electric output of the PV-hybrid collector is significantly higher than that of the TE collector as shown in Figure 2.6.

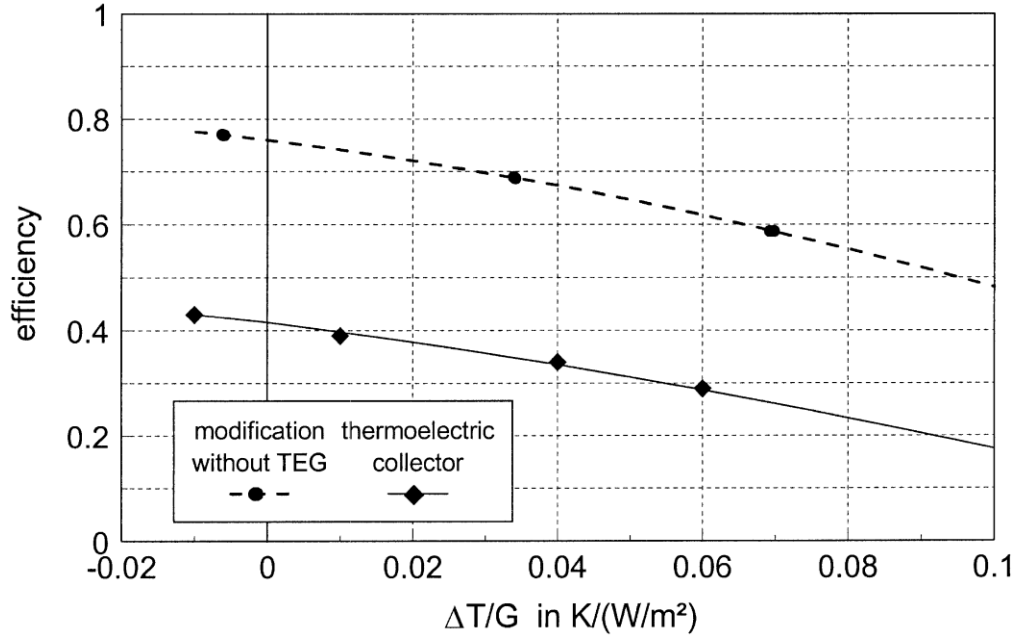


Figure 2.6 Thermal efficiency curve of the TE collector, compared to same collector without a TEG [61]

Esarte et al. [62] modeled the thermoelectric generator as heat exchangers element in order to study the flow parameters. They analyzed analytically and experimentally the influence of fluid flow rate, heat exchanger geometry (Spiral, Zig-Zag and Straight fins), fluid properties and inlet temperatures on the power supplied by the TE generator. They developed an expression that helps to design thermoelectric generators, through providing an idea about which operating conditions best meet the specifications required for a particular application. Their theoretical results meet with the experimental values for low flow rates but not for high flow rates. They explained that is because for high flow rates the parallel heat flux takes a major importance within the global heat transfer produced in the generator resulting in a decrease of the temperatures. They concluded that it is true that the more accurate the over-all heat transfer coefficient, the better the eventual results.

Enhancement of coefficient of performance in thermoelectric refrigeration has been studied and the optimization of heat dissipation was analyzed by Astrian et al. [63]. They constructed two prototypes of thermoelectric domestic refrigerators, one of them with the thermosyphon with a thermal resistance of 0.110 K/W developed, and the other with a conventional fins dissipater. They showed that the use of thermosyphon with phase change increases the coefficient of performance up to 32%.

Kubo et al. [64] experimentally and numerically investigated the performance of thermoelectric device. They studied the dependence of cold side temperature of TH device and the size of the incisions made on its side faces. The temperature difference between the hot and cold sides of the device was estimated, the electric power and the conversion efficiency were examined with a variations in the size of the side incisions and in the cold-side temperature. They illustrated that the results of the simulations were in fairly good agreement with the experimental results. They found that the electrical power generated, the conversion efficiency, and the incision size depend on the cold side temperature.

2.4 Objectives and Approach

The objectives and approaches of the thesis study are:

1. To analyze numerically the thermal efficiency of thermoelectric generator and study the influence of varying the cross-sectional area on it.
2. To perform thermal and stress analysis developed in thermoelectric generator based on Bi_2Te_3 commercial thermoelectric module using coupled temperature-displacement model built in ABAQUS. Conduction heat term is considered and two boundary conditions that are convection and radiation are applied to the surface of thermoelectric pins.
3. The effect of thermoelectric pin geometry on the temperature and stress field over the TE modules will be investigated.
4. To determine the optimum pin configuration with distributed thermal stress, lower maximum von Mises stress, which may prevent the TE device from damages, consequently to increase the life span of device.

CHAPTER 3

MATHEMATICAL ANALYSIS

In this chapter, the analysis pertinent to thermoelectric generator is divided into two sections. The first section gives detail information about thermodynamic analysis. The second section presents the thermal stress formulations relevant to the model used in TE study.

3.1 Thermodynamics Analysis

The efficiency of the trapezoidal pin thermoelectric power generator, which is shown in Figure 3.1, is given as [65]:

$$\eta = \frac{I^2 R_L}{SIT_H + k(T_H - T_L) - \frac{1}{2}I^2 R} \quad (3.1.1)$$

Where k is the thermal conductance and R is the electrical resistivity of the thermoelectric generator.

The current I is a function of Seebeck coefficient $S = S_p - S_n$, the upper and lower junction (plate) temperatures (T_H and T_L), the electrical resistance R and the external load resistance R_L as

$$I = \frac{S(T_H - T_L)}{R_L + R}, \quad (3.1.2)$$

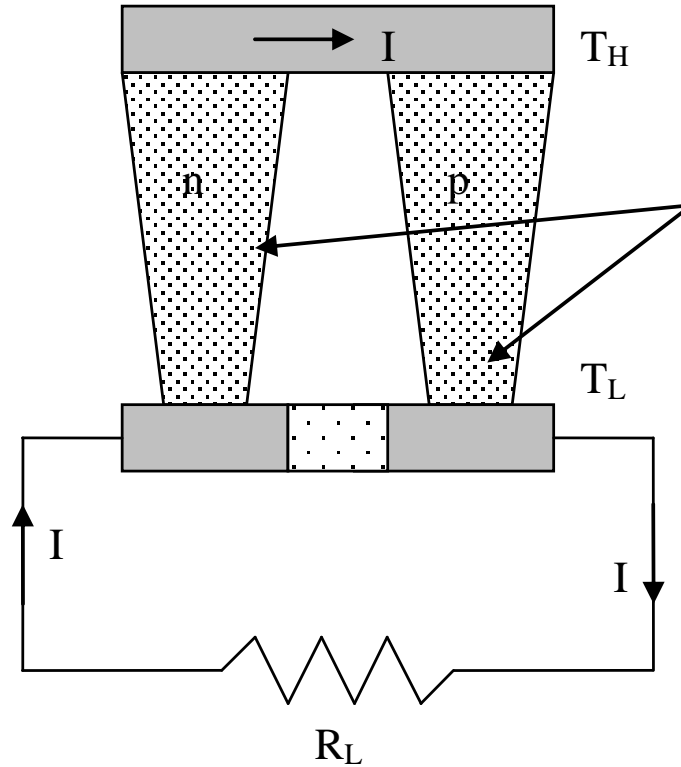


Figure 3.1 Schematic view of a thermoelectric power generator and pin configurations

Substituting equation 3.1.2 in equation 3.1.1, the efficiency becomes

$$\eta = \frac{S^2(T_H - T_L)R_L}{K(R_L + R)^2 + S^2T_H(R_L + R) - \frac{1}{2}S^2(T_H - T_L)R} \quad (3.1.3)$$

The cross-sectional area of the trapezoidal pin of the thermoelectric generator shown in Figure 3.2 is

$$A(x) = \frac{A_H - A_L}{L}x + A_L \quad (3.1.4)$$

Where A_L is the cross sectional area of the bottom side of the pin and A_H is that of the top side. L is the height of the pin. By defining an area ratio $R_A = A_H / A_L$, the cross-sectional area of the leg can be written as

$$A(x) = A_0 \left[1 + 2 \frac{R_A - 1}{R_A + 1} \left(\frac{x}{L} - \frac{1}{2} \right) \right] \quad (3.1.5)$$

where A_0 is the cross-sectional area of the uniform rectangular pin.

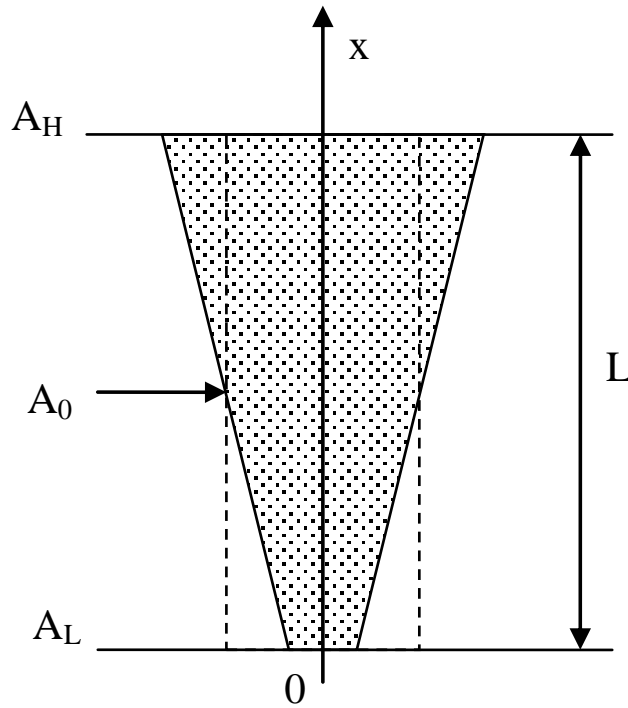


Figure 3.2 Geometric configuration of the thermoelectric generator pin

The heat transfer rate through the pin along x is given by:

$$\dot{Q} = -kA(x) \frac{dT}{dx} \quad (3.1.6)$$

After assuming a steady heating situation and isolated pin surfaces, equation 3.1.6 can be re-arranged as

$$\dot{Q} \int_0^L \frac{dx}{A(x)} = -k \int_{T_L}^{T_H} dT \quad (3.1.7)$$

Making use of equation 3.1.5 in equation 3.1.7, and performing the integration

$$\dot{Q} = \frac{2k \frac{A_0}{L} \left(\frac{R_A - 1}{R_A + 1} \right)}{\ln(R_A)} (T_H - T_L) \quad (3.1.8)$$

Equation 3.1.8 indicates that the overall thermal conductance of the trapezoidal pin is

$$k_{leg} = \frac{2k \frac{A_0}{L} \left(\frac{R_A - 1}{R_A + 1} \right)}{\ln(R_A)} \quad (3.1.9)$$

Considering the two pins in Figure 3.1, the total thermal conductance of the thermoelectric generator can be written as

$$k = 2(k_p + k_n) \frac{\frac{A_0}{L} \left(\frac{R_A - 1}{R_A + 1} \right)}{\ln(R_A)} \quad (3.1.10)$$

Where k_p and k_n are the thermal conductivities of the p-type and n-type pins, respectively.

On the other hand, the overall electrical resistance of the leg can be written as

$$R_{leg} = \int_0^L \frac{dx}{\sigma A(x)} \quad (3.1.11)$$

Substituting area of trapezoid $A(x)$ from equation 3.1.5 and carrying out the integration, the overall electrical resistance is obtained as

$$R_{leg} = \frac{1}{2\sigma \frac{A_0}{L} \left(\frac{R_A - 1}{R_A + 1} \right)} \ln(R_A) \quad (3.1.12)$$

Similarly, considering the two pins, the total electrical resistance of the thermoelectric generator becomes

$$R = \left(\frac{1}{\sigma_p} + \frac{1}{\sigma_n} \right) \frac{1}{2 \frac{A_0}{L} \left(\frac{R_A - 1}{R_A + 1} \right)} \ln(R_A) = \frac{\sigma_p + \sigma_n}{2\sigma_p \sigma_n \frac{A_0}{L} \left(\frac{R_A - 1}{R_A + 1} \right)} \ln(R_A) \quad (3.1.13)$$

Where σ_p and σ_n are the electrical conductivities of the p-type and n-type legs, respectively.

Substituting equation 3.1.10 and equations 3.1.13 in equation 3.1.3, the efficiency of the thermoelectric generator can be written in dimensionless form as

$$\eta = (1 - \theta) \frac{2ZT_{ave} \left(1 + \sqrt{\frac{r_k}{r_\sigma}} \right)^2 \left(\frac{R_L}{R_0} \right)}{(1 + \theta) \left(\frac{K}{K_0} \right) \left(\frac{R_L}{R_0} + \frac{R}{R_0} \right)^2 + 2ZT_{ave} \left(1 + \sqrt{\frac{r_k}{r_\sigma}} \right)^2 \left[\frac{R_L}{R_0} + \frac{1}{2} \frac{R}{R_0} (1 + \theta) \right]} \quad (3.1.14)$$

where

$$\theta = \frac{T_L}{T_H}, \text{ (Temperature ratio)} \quad (3.1.15)$$

$$r_k = \frac{k_p}{k_n}, \text{ (Thermal conductivity ratio)} \quad (3.1.16)$$

$$r_\sigma = \frac{\sigma_p}{\sigma_n}, \text{ (Electrical conductivity ratio)} \quad (3.1.17)$$

$$ZT_{ave} = \frac{S^2 \left(\frac{\sigma_n}{k_n} \right) T_H \left(\frac{1+\theta}{2} \right)}{\left(1 + \sqrt{\frac{r_k}{r_\sigma}} \right)^2} \text{ (The figure of merit based on the average temperature)} \quad (3.1.18)$$

$$K_0 = \frac{A_0 k_n}{L} \text{ (Reference thermal conductance)} \quad (3.1.19)$$

and

$$R_0 = \frac{L}{A_0 \sigma_n} \text{ (Reference electrical resistivity)} \quad (3.1.20)$$

Thus, the overall thermal conductance and overall electrical resistivity can be written in dimensionless form, respectively, as

$$\frac{K}{K_0} = 2 \frac{(r_k + 1)}{\ln(R_A)} \left[\frac{R_A - 1}{R_A + 1} \right] \quad (3.1.21)$$

$$\frac{R}{R_0} = \left(\frac{1 + r_\sigma}{r_\sigma} \right) \frac{\ln(R_A)}{2 \left[\frac{R_A - 1}{R_A + 1} \right]} \quad (3.1.22)$$

3.2 Thermal Stress Formulations

This section consists of two sub-sections. The first one gives the description of the heat transfer analysis through TE material with boundary condition which used in the modeling. The second part deals with the formulation of stress developed in TE material due to thermal force.

3.2.1 Heat Transfer Analysis

For heat transfer analysis, the ABAQUS capability is intended to model solid body heat conduction with general, temperature-dependent conductivity and quite general convection and radiation boundary conditions.

The basic energy balance equation for heat transfer is shown below as [66]

$$\int_V \rho \dot{U} dV = \int_A q dA + \int_V r dV \quad (3.2.1)$$

Where V is a volume of solid material, with surface area A , ρ is the density of the material, \dot{U} is the material time rate of internal energy, q is the heat flux flowing into the body per its unit area, and r represents the heat supplied externally into the body per unit volume.

The heat conduction is assumed to be governed by the Fourier law as

$$\mathbf{f} = -\mathbf{K} \frac{\partial T}{\partial \mathbf{x}} \quad (3.2.2)$$

Where \mathbf{K} is the conductivity matrix, with $\mathbf{K} = \mathbf{K}(T)$, \mathbf{f} is the heat flux and \mathbf{x} is position.

The model discretization performed by combining the energy balance equation 3.2.1 together with the Fourier law equation 3.2.2, the standard Galerkin approach can be obtained directly as

$$\int_V \rho \dot{U} \delta\theta dV + \int_V \frac{\partial \delta\theta}{\partial x} \cdot K \frac{\partial T}{\partial x} dV = \int_{A_q} \delta\theta q dA + \int_V \delta\theta r dV \quad (3.2.3)$$

Where $\delta\theta$ is an arbitrary variational field satisfying the essential boundary conditions. The body is approximated geometrically with finite elements, so the temperature is interpolated as

$$T = N^N(x)T^N, N = 1,2,3, \dots \quad (3.2.4)$$

Where T^N are nodal temperatures and also the Galerkin approach assumes that, the variational field, is interpolated by the same functions

$$\delta\theta = N^N \delta\theta^N \quad (3.2.5)$$

Then, first and second order polynomials in one, two, and three dimensions are used for the N^N . With these interpolations, Equation 3.2.3, becomes

$$\delta\theta^N \left\{ \int_V N^N \rho \dot{U} dV + \int_V \frac{\partial N^N}{\partial x} \cdot K \frac{\partial T}{\partial x} dV = \int_{A_q} N^N q dA + \int_V N^N r dV \right\} \quad (3.2.6)$$

And since $\delta\theta^N$ are arbitrary chosen, this gives the system of equations of the geometric approximation in continues time description as shown below

$$\int_V N^N \rho \dot{U} dV + \int_V \frac{\partial N^N}{\partial x} \cdot K \frac{\partial T}{\partial x} dV = \int_{A_q} N^N q dA + \int_V N^N r dV \quad (3.2.7)$$

For transient heat transfer analysis, equation 3.2.7 integrated over the time. In applied model, the backward difference algorithm is used which is:

$$\dot{U}_{t+\Delta t} = \frac{U_{t+\Delta t} - U_t}{\Delta t} \quad (3.2.8)$$

Then, introducing the operator in equation 3.2.8 into the energy balance equation 3.2.7 gives

$$\frac{1}{\Delta t} \int_V N^N \rho (U_{t+\Delta t} - U_t) dV + \int_V \frac{\partial N^N}{\partial x} \cdot K \frac{\partial T}{\partial x} dV - \int_{A_q} N^N q dA - \int_V N^N r dV = 0 \quad (3.2.9)$$

For nonlinear system, that when the rate of change in internal energy with respect to the change of temperature with a time (the Jacobian matrix) is not formed, the modified Newton method should be applied to take the effect of $T_{t+\Delta t}^N$. The formulation of the terms in the Jacobian matrix is described in the following section.

The internal energy term gives a Jacobian contribution:

$$\frac{1}{\Delta t} \int_V N^N \rho \left. \frac{dU}{dT} \right|_{t+\Delta t} N^M dV \quad (3.2.10)$$

Where $\left. \frac{dU}{dT} \right|_{t+\Delta t}$ is the specific heat and this term can result numerical instabilities in severe latent heat cases, when there is phase change in the material. Then, the conductivity term gives a Jacobian contribution:

$$\int_V \frac{\partial N^N}{\partial x} \cdot K \Big|_{t+\Delta t} \cdot \frac{\partial N^M}{\partial x} dV + \int_V \frac{\partial N^N}{\partial x} \cdot \left. \frac{dK}{dT} \right|_{t+\Delta t} \cdot \left. \frac{\partial T}{\partial x} \right|_{t+\Delta t} N^M dV \quad (3.2.11)$$

The second term of this equation is typically small since the variation of thermal conductivity is slow with respect to the temperature $\left. \frac{dK}{dT} \right|_{t+\Delta t}$. Because of this, and because the term is not symmetric, it is usually more efficient to omit it.

Also, for specific surface boundary conditions (surface or body fluxes) such as convection and radiation conditions, it can also be temperature dependent as it is described it in the following Jacobian equations:

$$\int_A N^N \frac{\partial q}{\partial T} \Big|_{t+\Delta t} N^M dA \quad (3.2.12)$$

For film (convection) condition:

$$q = h(T)[T - T_a] \quad (3.2.13)$$

Then,

$$\frac{\partial q}{\partial T} = \frac{\partial h}{\partial T} [T - T_a] + h$$

For radiation condition:

$$q = \varepsilon\sigma[T^4 - T_a^4] \quad (3.2.14)$$

Then,

$$\frac{\partial q}{\partial T} = 4\varepsilon\sigma T^3$$

Combining all the Jacobian terms will give the modified Newton method as shown below:

$$\begin{aligned}
& \left[\frac{1}{\Delta t} \int_V N^N \rho \frac{dU}{dT} \Big|_{t+\Delta t} N^M dV + \int_V \frac{\partial N^N}{\partial \mathbf{x}} \cdot \mathbf{K} \Big|_{t+\Delta t} \cdot \frac{\partial N^M}{\partial \mathbf{x}} dV \right. \\
& \quad \left. + \int_A N^N \left(\frac{\partial h}{\partial T} (T - T_a) + h + 4\varepsilon\sigma T^3 \right) N^M dA \right] c^{-M} \\
& = \int_V N^N r dV + \int_{A_q} N^N q dA - \frac{1}{\Delta t} \int_V N^N \rho (U_{t+\Delta t} - U_t) dV - \int_V \frac{\partial N^N}{\partial \mathbf{x}} \cdot \mathbf{K} \cdot \frac{\partial T}{\partial \mathbf{x}} dV
\end{aligned} \tag{3.2.15}$$

Where $T_{t+\Delta t, i+1}^N = T_{t+\Delta t, i}^N + c^{-M}$ and i = the iteration number

3.2.2 Stress Analysis

The conservation of energy implied by the first law of thermodynamics states that the time rate of change of kinetic energy and internal energy for a fixed body of material is equal to the sum of the rate of work done by the surface and body forces. This can be expressed as

$$\frac{d}{dt} \int_V \left(\frac{1}{2} \rho \mathbf{v} \cdot \mathbf{v} + \rho U \right) dV = \int_A \mathbf{v} \cdot \mathbf{t} dA + \int_V \mathbf{f} \cdot \mathbf{v} dV \tag{3.2.16}$$

Where ρ is the current mass density, \mathbf{v} is the velocity field vector, U is the internal energy per unit mass, \mathbf{t} is the surface traction vector, \mathbf{f} is the body force vector, and \mathbf{n} is the normal direction vector on boundary A .

By using Gauss' theorem and the identity that $\mathbf{t} = \boldsymbol{\sigma} \cdot \mathbf{n}$ on the boundary A , the first term of the right-hand side of equation 3.2.16 can be rewritten as

$$\begin{aligned}
\int_A \mathbf{v} \cdot \mathbf{t} dA &= \int_V \left(\frac{\partial}{\partial \mathbf{x}} \right) \cdot (\mathbf{v} \cdot \boldsymbol{\sigma}) dV \\
&= \int_V \left[\left(\frac{\partial}{\partial \mathbf{x}} \cdot \boldsymbol{\sigma} \right) \cdot \mathbf{v} + \frac{\partial \mathbf{v}}{\partial \mathbf{x}} : \boldsymbol{\sigma} \right] dV \quad (3.2.17) \\
&= \int_V \left[\left(\frac{\partial}{\partial \mathbf{x}} \cdot \boldsymbol{\sigma} \right) \cdot \mathbf{v} + \dot{\boldsymbol{\varepsilon}} : \boldsymbol{\sigma} \right] dV
\end{aligned}$$

Where $\dot{\boldsymbol{\varepsilon}}$ is the strain rate tensor and $\boldsymbol{\sigma}$ is symmetric, and by substituting equation 3.2.17 into equation 3.2.16 yields

$$\frac{d}{dt} \int_V \left(\frac{1}{2} \rho \mathbf{v} \cdot \mathbf{v} + \rho U \right) dV = \int_V \left[\left(\frac{\partial}{\partial \mathbf{x}} \cdot \boldsymbol{\sigma} + \mathbf{f} \right) \cdot \mathbf{v} + \boldsymbol{\sigma} : \dot{\boldsymbol{\varepsilon}} \right] dV \quad (3.2.18)$$

From Cauchy's equation of motion that stated

$$\frac{\partial}{\partial \mathbf{x}} \cdot \boldsymbol{\sigma} + \mathbf{f} = \rho \frac{d\mathbf{v}}{dt} \quad (3.2.19)$$

Substituting this into equation 3.2.18 gives

$$\begin{aligned}
\frac{d}{dt} \int_V \left(\frac{1}{2} \rho \mathbf{v} \cdot \mathbf{v} + \rho U \right) dV &= \int_V \left[\rho \frac{d\mathbf{v}}{dt} \cdot \mathbf{v} + \boldsymbol{\sigma} : \dot{\boldsymbol{\varepsilon}} \right] dV \\
&= \int_V \left[\frac{d}{dt} \left(\frac{1}{2} \rho \mathbf{v} \cdot \mathbf{v} \right) + \boldsymbol{\sigma} : \dot{\boldsymbol{\varepsilon}} \right] dV \quad (3.2.20)
\end{aligned}$$

From this we get the energy equation

$$\rho \frac{dU}{dt} = \boldsymbol{\sigma} : \dot{\boldsymbol{\varepsilon}} \quad (3.2.21)$$

By performing the integration this equation

$$\int_0^t \left(\int_V \boldsymbol{\sigma} : \dot{\boldsymbol{\varepsilon}} dV \right) dt = \int_V \rho U dV + U_0$$

where U_0 is the energy at time zero.

Integrating the energy balance equation 3.2.16 in time gives

$$\int_V \frac{1}{2} \rho \mathbf{v} \cdot \mathbf{v} dV + \int_V \rho U dV = \int_0^t \dot{E}_{WF} d\tau + \text{constant} \quad (3.2.22)$$

This equation can be represented as

$$E_K + E_U = \int_0^t \dot{E}_{WF} d\tau + \text{constant} \quad (3.2.23)$$

Where \dot{E}_{WF} is defined as the rate of work done to the body by external forces and contact friction forces between the contact surfaces

$$\dot{E}_{WF} = \int_A \mathbf{v} \cdot \mathbf{t} dA + \int_V \mathbf{f} \cdot \mathbf{v} dV \quad (3.2.24)$$

And E_K , the kinetic energy, and E_U , the internal energy, are given by

$$E_K = \int_V \frac{1}{2} \rho \mathbf{v} \cdot \mathbf{v} dV \quad (3.2.25)$$

$$E_U = \int_V \rho U dV = \int_0^t \left(\int_V \boldsymbol{\sigma} : \dot{\boldsymbol{\varepsilon}} dV \right) d\tau - U_0 \quad (3.2.26)$$

To analyze the energy balance equation more deeply, the breakdowns of the stress, strain, and tractions is introduced.

By splitting the traction, \mathbf{t} , into the surface distributed load, \mathbf{t}_s , the solid infinite element radiation traction, \mathbf{t}_{qb} , and the frictional traction, \mathbf{t}_f , the \dot{E}_{WF} can be written as

$$\dot{E}_{WF} = \left(\int_A \mathbf{v} \cdot \mathbf{t}_{sl} dA + \int_V \mathbf{f} \cdot \mathbf{v} dV \right) - \left(- \int_A \mathbf{v} \cdot \mathbf{t}_f dA \right) - \left(- \int_A \mathbf{v} \cdot \mathbf{t}_{qb} dA \right)$$

$$\dot{E}_{WF} = \dot{E}_W - \dot{E}_F - \dot{E}_{QB} \quad (3.2.27)$$

where \dot{E}_W is the rate of work done to the body by external forces, \dot{E}_{QB} is the rate of energy dissipated by the damping effect of solid medium infinite elements, and \dot{E}_F is the rate of energy dissipated by contact friction forces between the contact surfaces. Then, an energy balance for the entire model can then be written as

$$E_U + E_K + E_F - E_W - E_{QB} = \text{constant} \quad (3.2.28)$$

Then, the dissipated portions of the internal energy are split off

$$E_U = \int_0^t \left(\int_V \boldsymbol{\sigma} : \dot{\boldsymbol{\epsilon}} dV \right) d\tau = \int_0^t \left[\int_V (\boldsymbol{\sigma}^c + \boldsymbol{\sigma}^v) : \dot{\boldsymbol{\epsilon}} dV \right] d\tau$$

$$= \int_0^t \left(\int_V \boldsymbol{\sigma}^c : \dot{\boldsymbol{\epsilon}} dV \right) d\tau + \int_0^t \left(\int_V \boldsymbol{\sigma}^v : \dot{\boldsymbol{\epsilon}} dV \right) d\tau \quad (3.2.29)$$

$$= E_I + E_V$$

Where $\boldsymbol{\sigma}^c$ is the stress derived from the user-specified constitutive equation, without viscous dissipation effects included, $\boldsymbol{\sigma}^{el}$ is the elastic stress, $\boldsymbol{\sigma}^v$ is the viscous stress, E_v is the energy dissipated by viscous effects, and E_I is the remaining energy, which called the internal energy.

Then, by introducing the strain decomposition

$$\dot{\boldsymbol{\epsilon}} = \dot{\boldsymbol{\epsilon}}^{el} + \dot{\boldsymbol{\epsilon}}^{pl} + \dot{\boldsymbol{\epsilon}}^{cr} \quad (3.2.30)$$

Where $\dot{\boldsymbol{\epsilon}}^{el}$, $\dot{\boldsymbol{\epsilon}}^{pl}$ and $\dot{\boldsymbol{\epsilon}}^{cr}$ are elastic, plastic, and creep strain rates, respectively.

The internal energy, E_I , can be expressed as

$$E_I = \int_0^t \left(\int_V \boldsymbol{\sigma}^c : \dot{\boldsymbol{\epsilon}} dV \right) d\tau$$

$$\begin{aligned}
&= \int_0^t \left(\int_V \boldsymbol{\sigma}^c : \dot{\boldsymbol{\varepsilon}}^{el} dV \right) d\tau + \int_0^t \left(\int_V \boldsymbol{\sigma}^c : \dot{\boldsymbol{\varepsilon}}^{pl} dV \right) d\tau + \int_0^t \left(\int_V \boldsymbol{\sigma}^c : \dot{\boldsymbol{\varepsilon}}^{cr} dV \right) d\tau \\
&= E_S + E_P + E_C
\end{aligned} \tag{3.2.31}$$

Where E_S is the applied elastic strain energy, E_P is the energy dissipated by plasticity, and E_C is the energy dissipated by time-dependent deformation like creep energy.

The additive strain rate decomposition can also be introduced to give

$$\dot{\boldsymbol{\varepsilon}}^{el} = \dot{\boldsymbol{\varepsilon}} - \dot{\boldsymbol{\varepsilon}}^{th} - \dot{\boldsymbol{\varepsilon}}^{pl} \tag{3.2.32}$$

Where $\dot{\boldsymbol{\varepsilon}}^{th}$ is the strain caused by thermal expansion which is in the constitutive models in ABAQUS is function of temperature $\dot{\boldsymbol{\varepsilon}}^{th} = \dot{\boldsymbol{\varepsilon}}^{th}(T)$ only.

CHAPTER 4

NUMERICAL MODELING

The thermal efficiency of thermoelectric module for various area ratios, which is presented in equation 3.1.14, is simulated using the data in Table 4.1.

For the thermal stress analysis, a fully coupled thermal-stress ABAQUS finite element code is used to simulate temperature and stress fields in the thermoelectric generator. ABAQUS-Standard code uses an implicit backward-difference scheme for time integration of temperatures and displacement at each grid point and the nonlinear coupled system is solved using Newton's method equation 3.2.15

For fully coupled temperature and displacement (thermal-stress) analysis, ABAQUS solves a system of coupled equations [66]

$$\begin{bmatrix} K_{uu} & K_{uT} \\ K_{Tu} & K_{TT} \end{bmatrix} \begin{Bmatrix} \Delta u \\ \Delta T \end{Bmatrix} = \begin{Bmatrix} R_u \\ R_T \end{Bmatrix}$$

where Δu and ΔT are the respective corrections to the incremental displacement and temperature, K_{ij} are sub-matrices of the fully coupled stiffness matrix, and R_u and R_T are the mechanical and thermal residual vectors, respectively.

In more details, the coupled thermal stress analysis requires identifying the displacement-strain relations, which are expressed in dimensionless form as follows [67]:

$$\bar{\epsilon}_{xx} = \frac{\partial \bar{u}}{\partial \bar{x}}, \quad \bar{\epsilon}_{yy} = \frac{\partial \bar{v}}{\partial \bar{y}}, \quad \bar{\epsilon}_{zz} = \frac{\partial \bar{w}}{\partial \bar{z}} \quad (24)$$

$$\bar{\epsilon}_{xy} = \frac{1}{2} \left(\frac{\partial \bar{u}}{\partial \bar{y}} + \frac{\partial \bar{v}}{\partial \bar{x}} \right), \quad \bar{\epsilon}_{yz} = \frac{1}{2} \left(\frac{\partial \bar{v}}{\partial \bar{z}} + \frac{\partial \bar{w}}{\partial \bar{y}} \right), \quad \bar{\epsilon}_{zx} = \frac{1}{2} \left(\frac{\partial \bar{u}}{\partial \bar{z}} + \frac{\partial \bar{w}}{\partial \bar{x}} \right) \quad (25)$$

An exact implementation of Newton's method involves a nonsymmetrical stiffness matrix which is stress-strain relation in dimensionless form as is illustrated in the following matrix representation of the coupled equations [67]:

$$\begin{pmatrix} \bar{\sigma}_{xx} \\ \bar{\sigma}_{yy} \\ \bar{\sigma}_{zz} \\ \bar{\sigma}_{yz} \\ \bar{\sigma}_{zx} \\ \bar{\sigma}_{xy} \end{pmatrix} = \frac{\bar{E}}{(1+\nu)(1-2\nu)} \begin{bmatrix} 1-\nu & \nu & \nu & 0 & 0 & 0 \\ \nu & 1-\nu & \nu & 0 & 0 & 0 \\ \nu & \nu & 1-\nu & 0 & 0 & 0 \\ 0 & 0 & 0 & 1-2\nu & 0 & 0 \\ 0 & 0 & 0 & 0 & 1-2\nu & 0 \\ 0 & 0 & 0 & 0 & 0 & 1-2\nu \end{bmatrix} \begin{pmatrix} \bar{\epsilon}_{xx} \\ \bar{\epsilon}_{yy} \\ \bar{\epsilon}_{zz} \\ \bar{\epsilon}_{yz} \\ \bar{\epsilon}_{zx} \\ \bar{\epsilon}_{xy} \end{pmatrix} - \begin{pmatrix} 1 \\ 1 \\ 1 \\ 0 \\ 0 \\ 0 \end{pmatrix} \frac{\bar{\alpha} \bar{E} \bar{T}}{1-2\nu} \quad (26)$$

Solving this system of equations requires the use of the un-symmetric matrix storage and solution scheme. Furthermore, the mechanical and thermal equations must be solved simultaneously.

Table 4.1 Properties of Bi₂Te₃ used for the efficiency calculation

Parameter	values
$\frac{R_L}{R_0}$	10
ZT_{ave}	0.9
r_k	1.25
r_σ	1.2
θ	$\frac{300}{550}$

Recall:

R_0 is the reference electrical resistivity,

ZT_{ave} is the figure of merit based on the average temperature,

r_k is the thermal conductivity ratio,

r_σ is the electrical conductivity ratio,

θ is the Temperature ratio

4.1 Model validation

The coupled (temperature-displacement) model used in the present study is validated by comparing with the data of thermal-stress study for Bi_2Te_3 -based thermoelectric modules achieved by GAO et al. [49].

To validate the predictions of thermal stress analysis, simulations are extended to include the cases, which were presented in the early study [49]. In this case, simulations conditions are re-set to be in line with the previous study and the parameters of the model used in the previous study are incorporated in the simulations.

Figure 4.1 shows a comparison for the maximum von Mises stress developed in various thermoelectric modules of different pin length predicted using coupled model with data presented for 3 mm side length of the pin [49]. The lengths of the module were 0.5, 1, 2, 3, 4, and 5 mm. Also, Table 4.2 illustrates the values of maximum and minimum von Mises stresses for TE pins. It is evident that both results are in good agreement. Therefore, the model used in the present study is justifiable to proceed with the predictions of thermal stress fields in the thermoelectric generator.

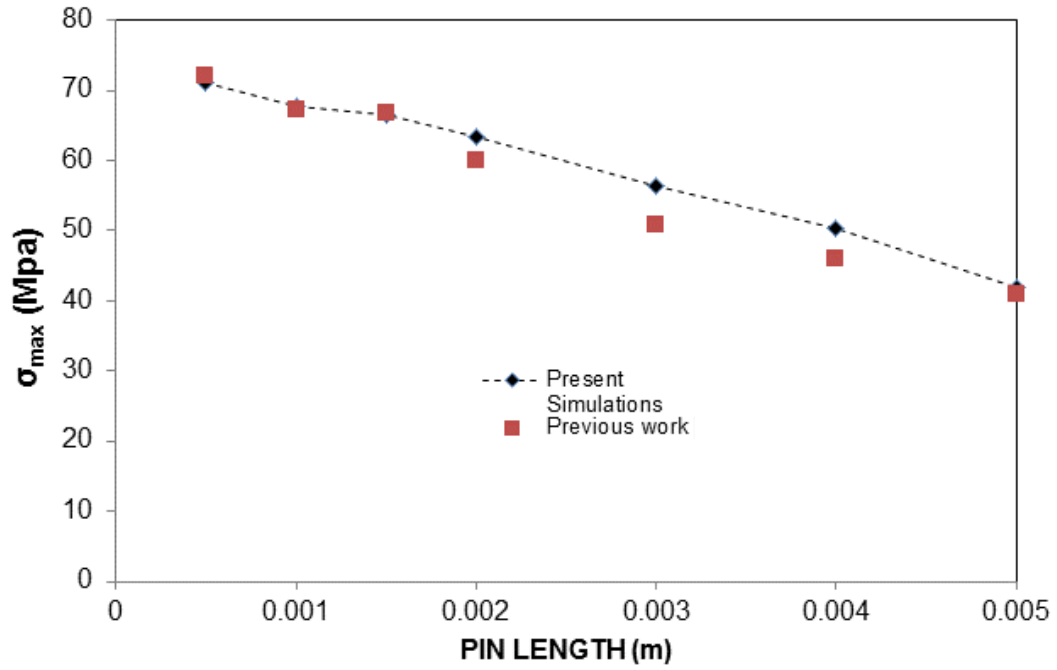


Figure 4.1 Validation of present simulations with the previous study [49]

Table 4.2 Maximum and Minimum von Mises stress for TE pins of present simulations with the previous study

	Present simulation	Previous study [49]
Max. Stress (GPa)	0.292	0.319
Min. Stress (MPa)	52.05	41.1

4.2 Modeling Assumptions

In thermal-stress modeling, the following assumptions and approximations are made:

- The material properties of TE pins are a function of temperature, not position. Since there is no diffusion of material near the boundaries of the thermoelectric and the materials selected are homogenous.
- There is thermal contact resistance. This assumption gives the actual model analysis. The contact layer used is that solder 60% Sn 40% Pb.
- The radiation losses from the edges of the TE legs are considered. The radiation heat transfer affects the temperature distribution over the TE module and thermal stress also, thus getting the most realistic condition.
- The convection losses from the thermoelectric pins edges to the surroundings are considered.
- The Peltier heat transfer through TE pin is ignored since it has small effect on the stress developed, which means the total heat input into the thermoelectric is just the Fourier heat through the interface and radiation and convection losses from the side surface of the pins.
- The temperature profile across TE pin varies with the horizontal axis (x and z axis of the pin. At both the hot-side and cold-side interfaces, the temperature is uniform across the leg. Sidewall radiation losses will produce some non-uniformity in the temperature profile from the center of TE pin to the side surface. The temperature of the hot side is uniform at T_H (240⁰C). This assumption of temperature is just prior the limitation of diffusion for Bi₂Te₃.

- The cold side temperature fixed at T_C (24°C) using constant wall-temperature condition.
- The cross-sectional areas of thermoelectric pin are varying along the leg length. Varying these areas would influence the distribution of stress that developed in thermoelectric modules.
- Commercial thermoelectric generator with small dimensions is used in this thesis.

4.3 Thermoelectric modeling

This section describes the modeling of thermoelectric module which aimed to analyze two physical parameters those are thermal and stresses which have coupled effects. The thermoelectric modules with the following considerations and the finite element discretization are achieved by using ABAQUS 6.10 software.

Thermoelectric generators (TEG) are made from thermoelectric modules and in this study, one module of the TEG is considered as shown in Figure 4.2.

The TE module consists of ceramic substrate, copper plate, Tin-Lead solder, and thermoelectric pins. TE module dimensions are shown in Figure 4.2 where the thickness of copper plate is 0.12 mm, the thickness of solder is 0.04 mm, and the thickness of ceramic substrate is 0.34 mm. The size of TE pins is 3mm×3mm×3mm.

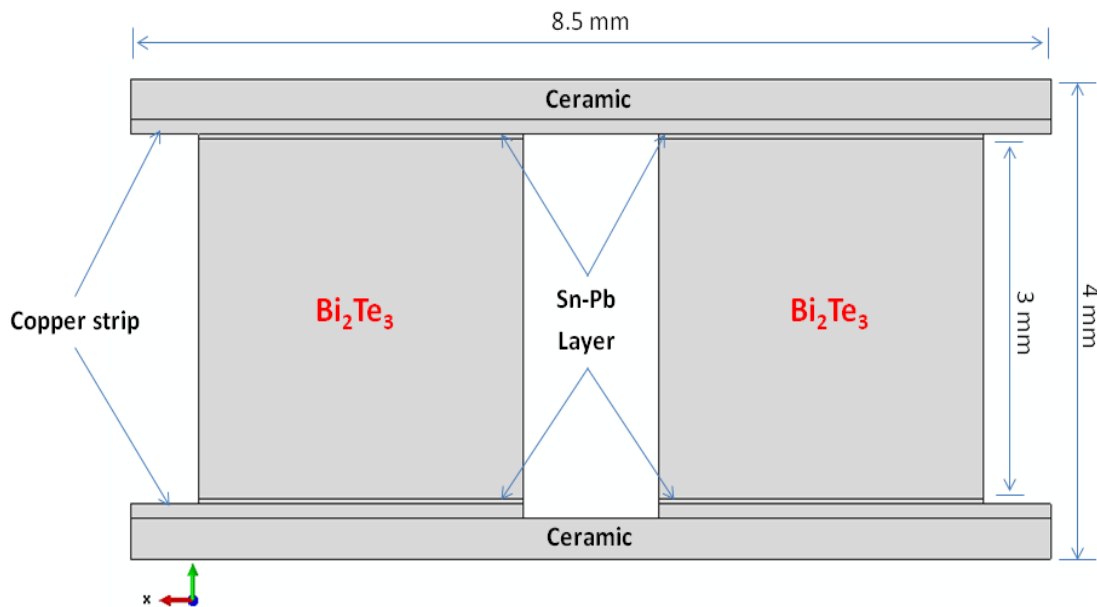


Figure 4.2 The geometric dimensions of TEG module

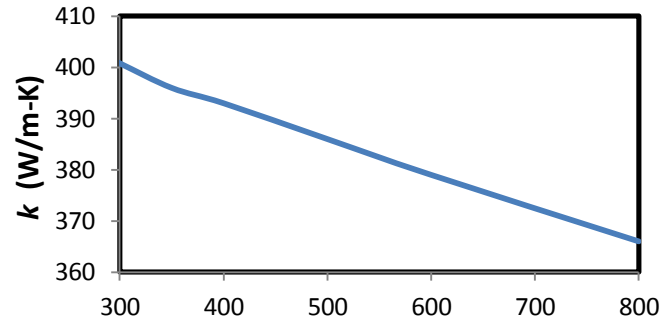
In this simulation, it is assumed that the thermoelectric pins are made of one material that n-type Bi_2Te_3 and that there is no difference in properties as a function of position, so that the thermoelectric and mechanical properties are function of temperature only. The density ρ , thermal conductivity k (T), coefficient of liner thermal expansion α (T), specific heat capacity c_p (T), and modulus of elasticity E (T), and Poisson's ratio ν are needed in this study.

The materials used are alumina Al_2O_3 as ceramic substrate, copper plate as conductor, Tin-Lead solder (60% Sn-40%Pb) as a welding layer, and n-type Bismuth Telluride (Bi_2Te_3) as the martial of the TE pins.

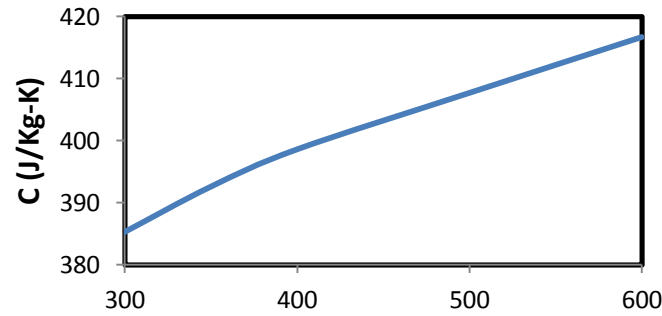
The properties of materials used in these simulations are presented in Table 4.3. The temperature dependence of the material properties [$k(T)$, $c_p(T)$, $\alpha(T)$, and $E(T)$] are shown in Figure 4.3 and Figure 4.4 for copper strip and Bi_2Te_3 pins , respectively.

Table 4.3 Material properties of TEG module, [T. depend means temperatures dependent]

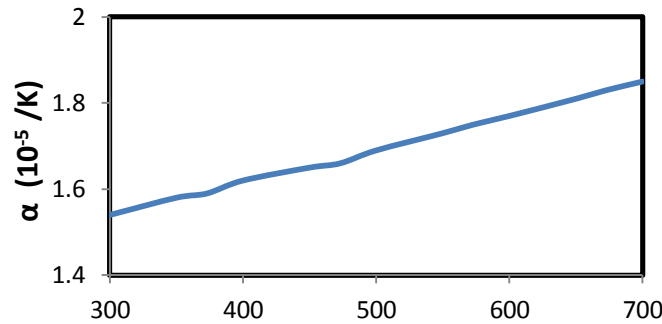
	Young modulus (Pa)	Poisson's ratio	Density (kg/m³)	Specific Heat (J/K-kg)	Thermal conductivity (W/m-K)	Thermal expansion (/K)
Ceramic Substrate	300E9	0.21	3690	880	18	8.1E-5
Sn-Pb Solder	30E9	0.33	8500	220	49	2.5E-5
Copper	T. depend	0.34	8960	T. depend	T. depend	T. depend
n-type Bi₂Te₃	T. depend	0.23	7740	154.4	T. depend	T. depend



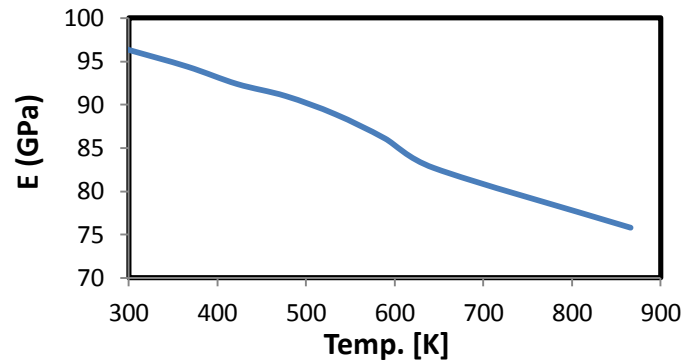
(a)



(b)

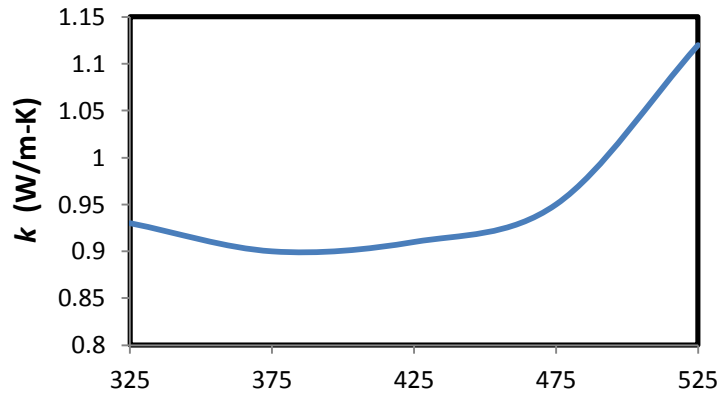


(c)

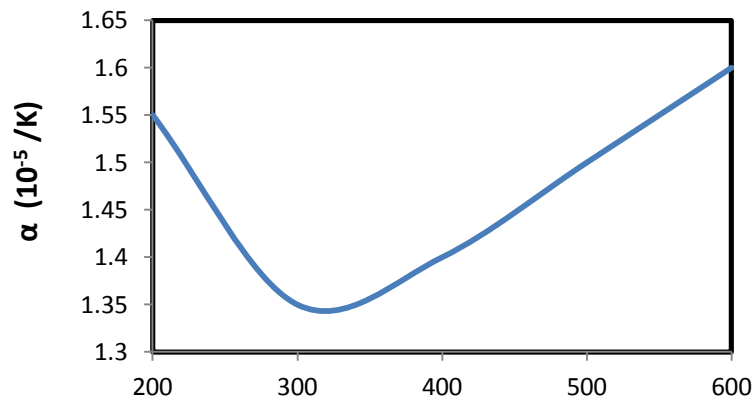


(d)

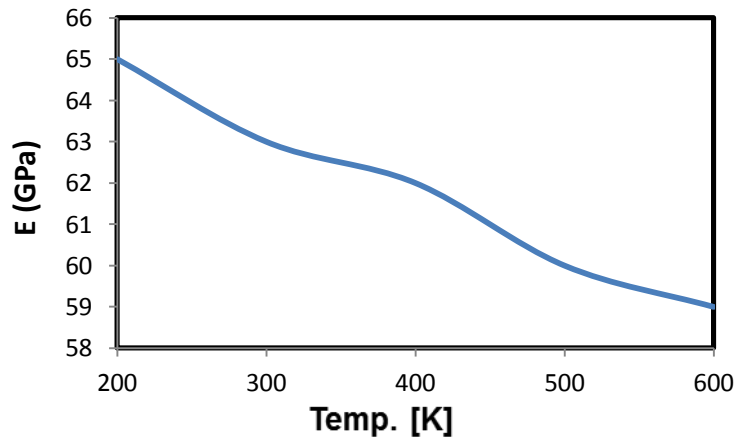
Figure 4.3 The temperature dependence properties of copper plate, (a) thermal conductivity, (b) specific heat, (c) coefficient of linear expansion, and (d) modulus of elasticity [68,69]



(a)



(b)



(c)

Figure 4.4 The temperature dependence properties of Bi_2Te_3 , (a) thermal conductivity, (b) coefficient of linear expansion, and (c) modulus of elasticity. [17,70]

4.3.1 Numerical Simulation

Finite element discretization is carried out by using ABAQUS 6.10 software. The simulation is performed in Abaqus/Standard temperature-displacement model and different TE modules were investigated.

The modeling consists of two steps that are heating and cooling steps. The first step, to analyze the stress developed due to thermal heating of the model. Heating process was applied continually until the temperature distribution of the TE module reaches to steady state profile. The second step, to investigate the residual stress after the TE release all of the heat that gained in the heating process and become to the initial condition and this called "thermal cycling process".

In the thermal stress analysis, a structured grid elements are used to create the model used element type C3D8T which is an 8-node thermally coupled brick, tri-linear displacement and temperature. Figure 4.5 shows the mesh generated in this simulations with approximate global size of 0.5 mm.

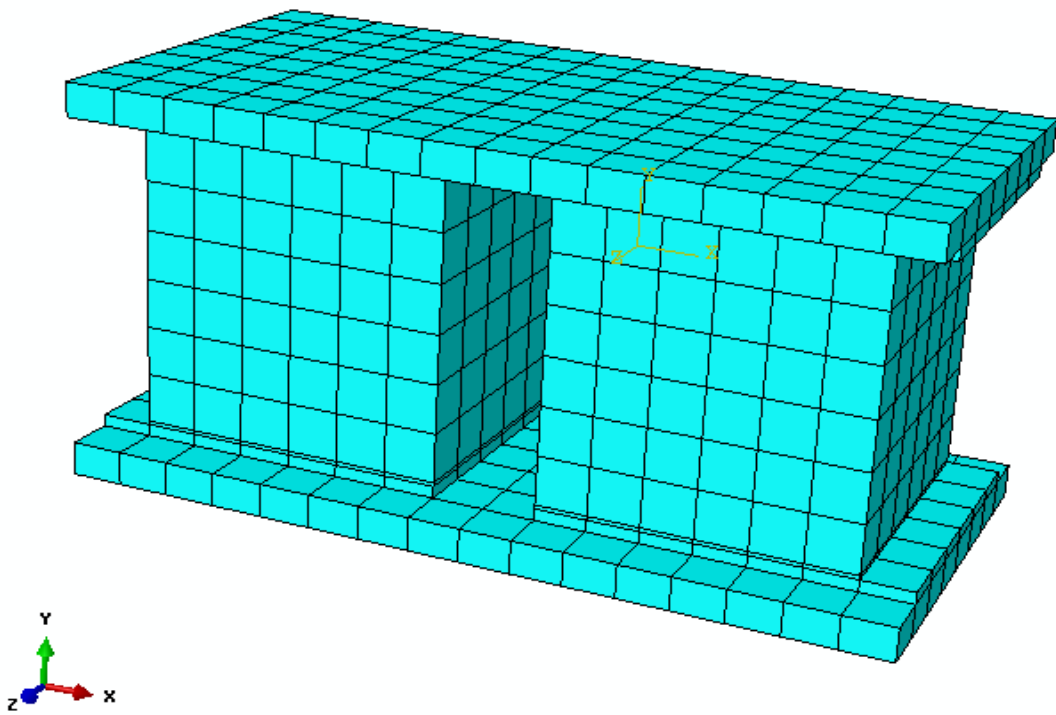


Figure 4.5 Model mesh of TE pins used in the simulations

4.3.2 Boundary conditions

In this study, a uniform wall temperature (UWT) is specified at the hot-side of substrate to be 513 K and at cold-side of substrate to be 297 K. Both sides of substrate are free from convection. Figure 4.6 shows the schematic view of three-dimensional thermoelectric generator module used in the present study with illustrating the thermal force applied on it.

The initial condition, at time equals zero second, applied to TE module is that the temperature of whole body is equal to ambient temperature of 297 K. Fixed boundary conditions are specified to the side surfaces of TE pin for the heat losses.

Figure 4.7 shows the convection and radiation heat losses over one TE pin. The heat loss flux along thermoelectric pins can be computed by Newton's law for the convection heat transfer and Stefan-Boltzmann law for the radiation heat transfer as following equations.

The Heat flux through TE pin surface due to convection is governed by

$$q_{cov} = -h (T - T_a)$$

The value of heat transfer coefficient h is specified as 10 W/K.m² and the sink temperature T_a as 297 K.

Also, Heat flux on the TE surface due to radiation to the environment is governed by

$$q_{rad} = \varepsilon\sigma[(T - T_{abs})^4 - (T_a - T_{abs})^4]$$

The emissivity of the surface ε is defined as 0.8, the Stefan-Boltzmann constant as ($\sigma = 5.67 \times 10^{-8} \frac{W}{m^2K^4}$), and T_{abs} is the value of absolute zero.

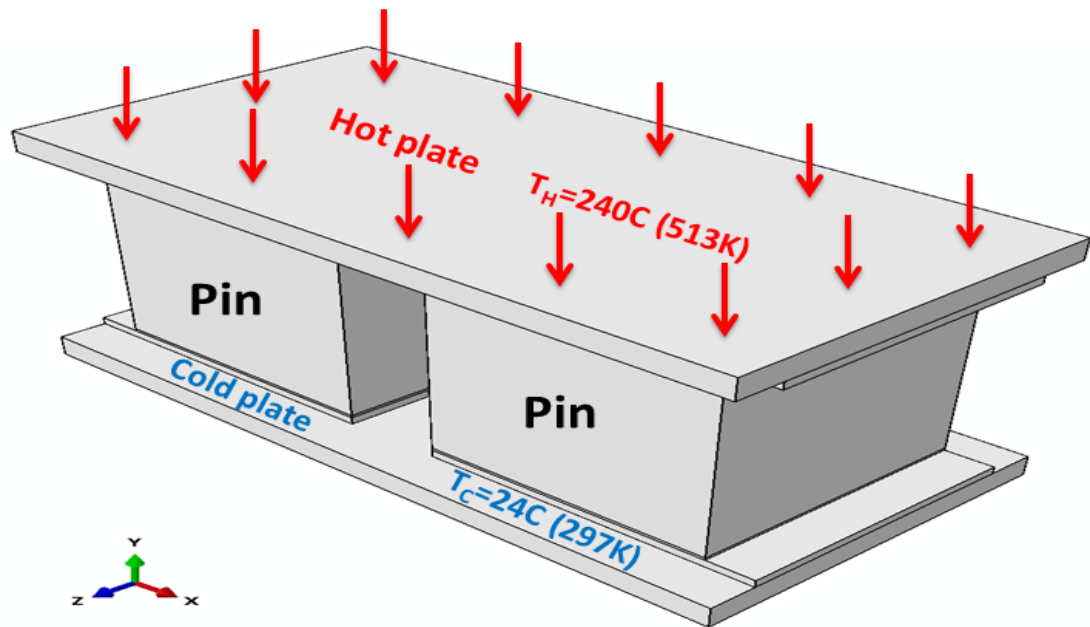


Figure 4.6 Schematic diagram of TE generator module with [force applied] used in ABAQUS simulation

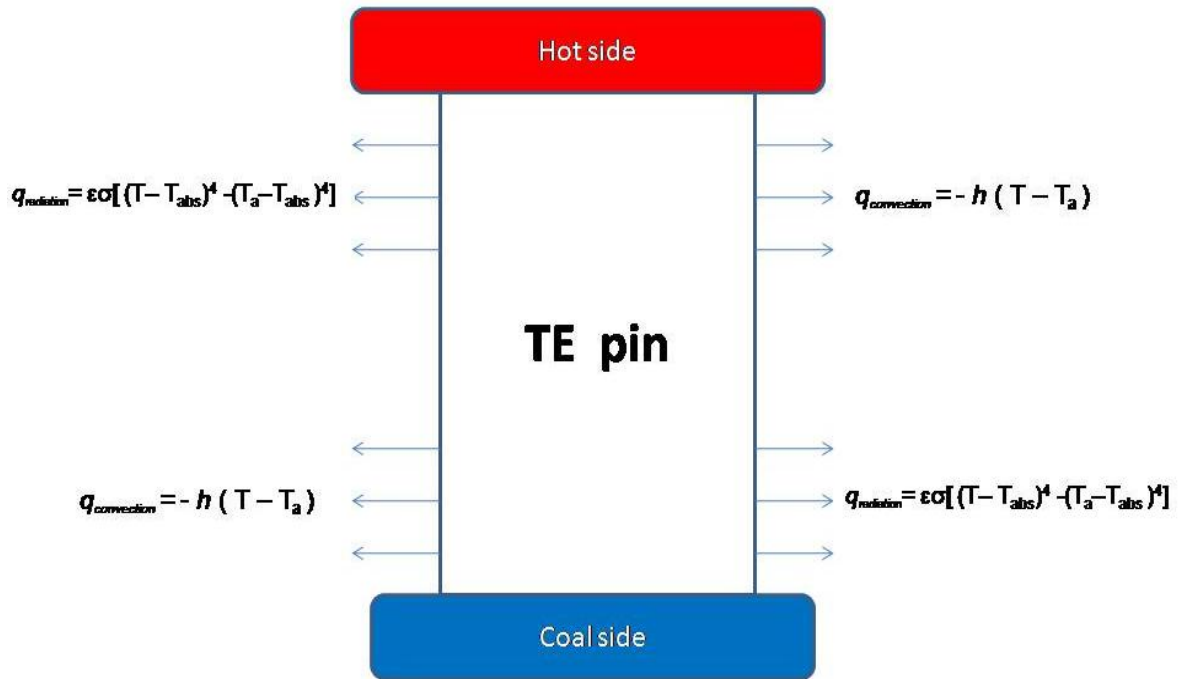


Figure 4.7 Heat losses for TE pin

CHAPTER 5

RESULTS AND DISCUSSION

The chapter consists of three sections. The first section presents the thermodynamics results and outcomes. Second, the results of the thermal stress analysis and the influence of the pin configurations are presented and discussed. In third section, thermal cycling results are shown and discussed.

5.1 Thermodynamics Results

Thermodynamic analysis and thermal stress field developed in the thermoelectric generator are investigated and the influence of pin geometric configuration on thermal efficiency and thermal stress levels are examined.

Figure 5.1 shows efficiency variation with the geometric parameter R_A , which is the area ratio of the pin cross-section at cold junction to hot junction ($R_A = A_H / A_L$). It can be observed that thermal efficiency of the thermoelectric generator increases for R_A values different than $R_A = 1$ and the minimum efficiency occurs for $R_A = 1$. This indicates that parallel sided pins for the thermoelectric generator are not always the optimum design for the maximum efficiency. Consequently, the pin design including either $R_A \leq 0.5$ and $R_A \geq 2$ results in improved thermal efficiency.

Although the improvement in thermal efficiency is low, small improvement of thermal efficiency, which is approximately 2%, for one device adds to the set of TE modules which forms the thermoelectric generator and adds to the improvement of the overall thermal efficiency of all devices in series, which are used for the practical applications.

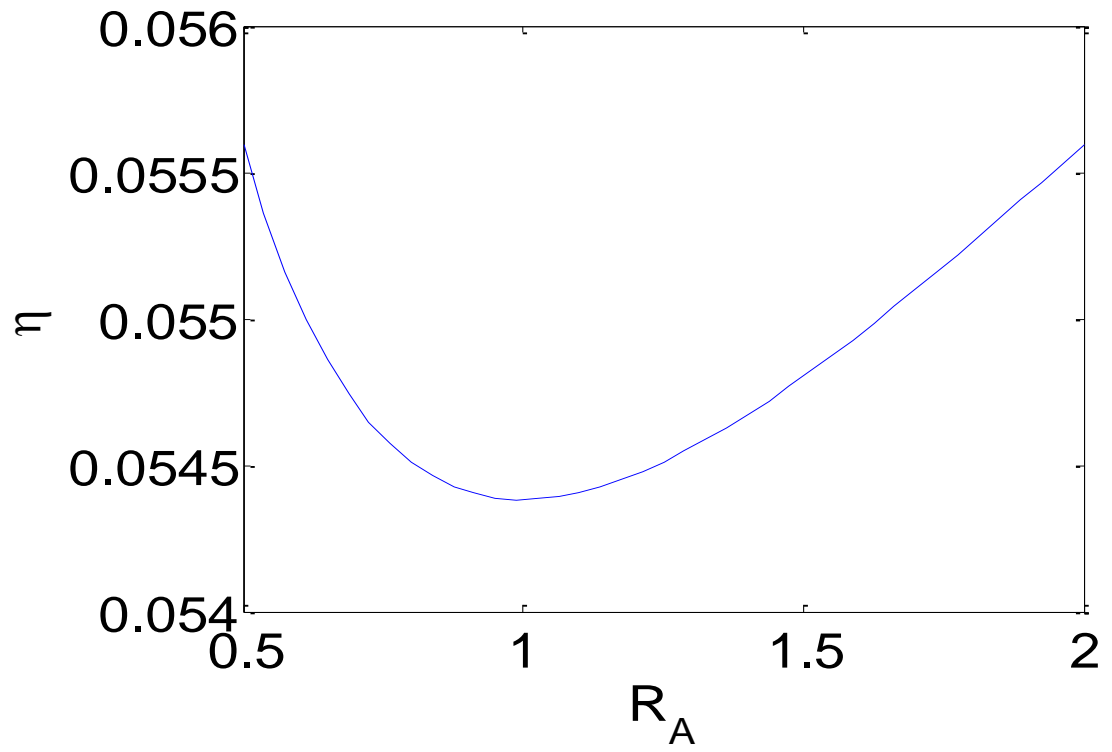


Figure 5.1 Thermal efficiency variation with R_A (pin area ratio of at hot junction to cold junction), $R_A = A_H / A_L$.

5.2 Influence of the pin configurations on the Thermal stress

Figure 5.2 Shows temperature distribution along the two lines in the y-axis for $R_A = 0.5$. The centerline represents the line passing through the pin center along the y-axis (Figure 5.3) and maximum stress line corresponds to the line passing through the maximum stress locations along the y-axis (Figure 5.3). Temperature distribution is presented when the temperature in the pin reaches to a steady state distribution. It should be noted that the transient heating takes place only 0.3 sec after the heating is initiated for the hot side of thermoelectric pins but its take about 11 sec to the whole body of device, as shown in Figure 5.4, and temperature field settles through heat in the thermoelectric device including the pins. The temperature decays gradually along the pin height for both lines in the y-axis. However, the temperature gradients differ totally along these lines, which are evident from Figure 5.5, in which the temperature gradient along the y-axis is shown. The temperature gradient attains high values in the region close to the hot junction of the pin, which is more pronounced along the maximum stress line. However, the temperature gradient reduces towards the cold junction of the pin. When comparing the temperature gradients along both lines; it is evident that the temperature gradient is higher in hot junction of the pin along the maximum stress line as compared to that of the center line.

However, opposite is true in the region towards the cold junction. Consequently, large changes in the temperature gradient results development of high strain in the pin. Figure 5.6 shows temperature contours in the thermoelectric generator and the pins. It is evident that temperature remains almost uniform along the x and z-axes. The large variation in the temperature occurs along the y-axis between the hot and cold junctions.

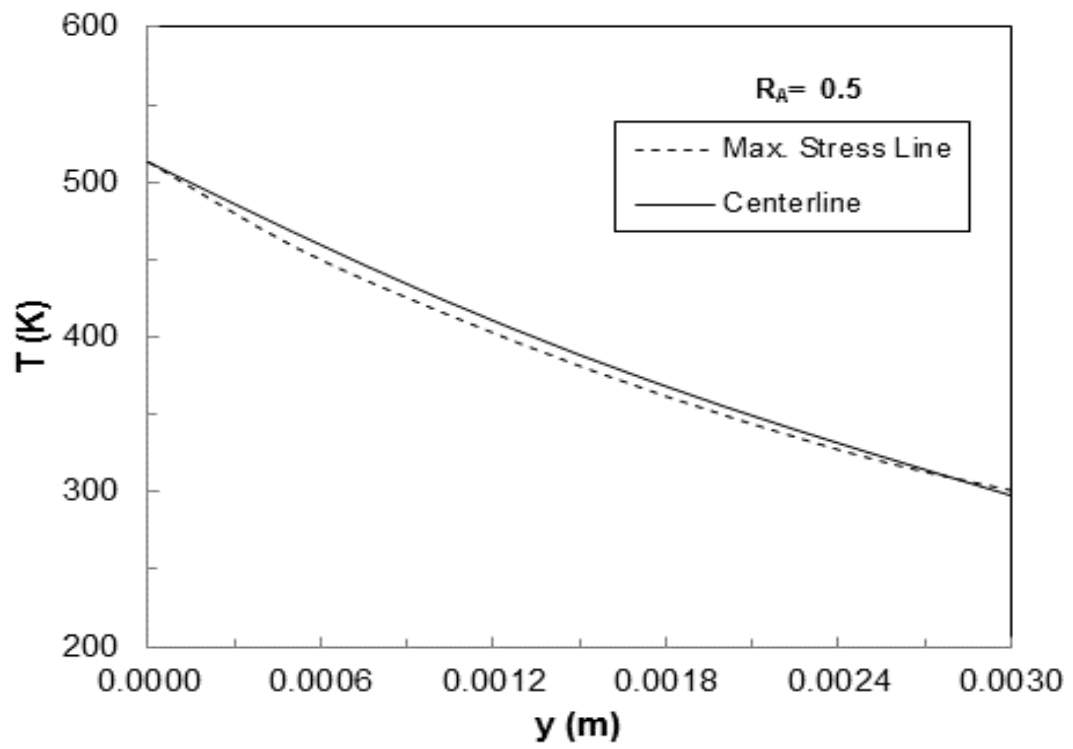


Figure 5.2 Temperature distribution along the centerline and the maximum stress line for $R_A = 0.5$

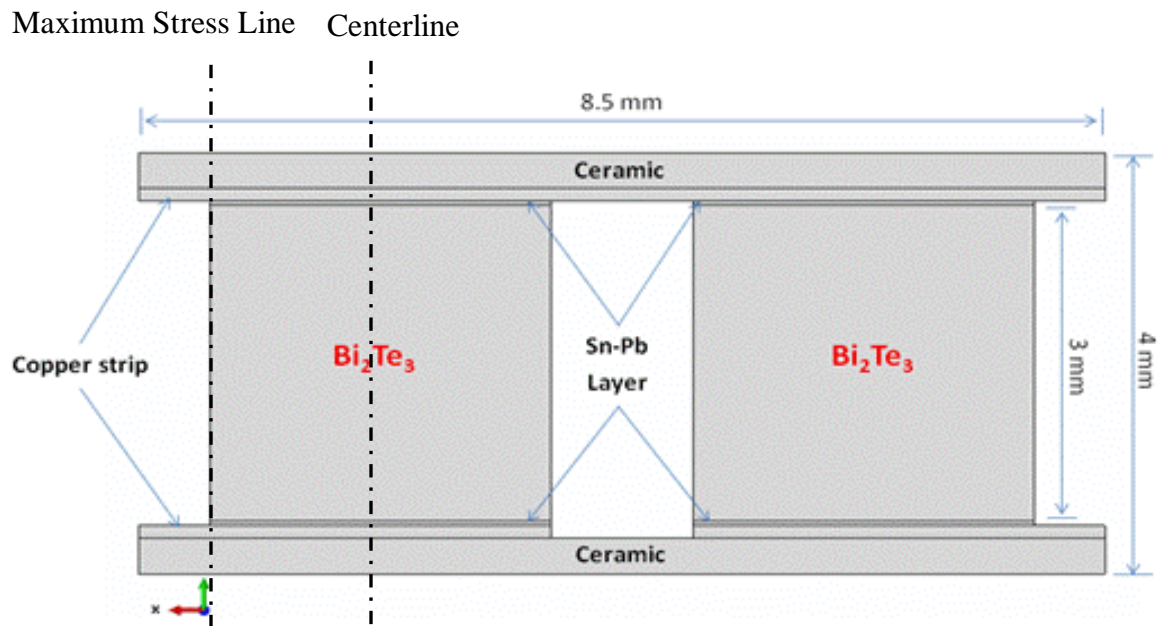


Figure 5.3 Three-dimensional view of thermoelectric generator with defining Max. Stress line and centerline.

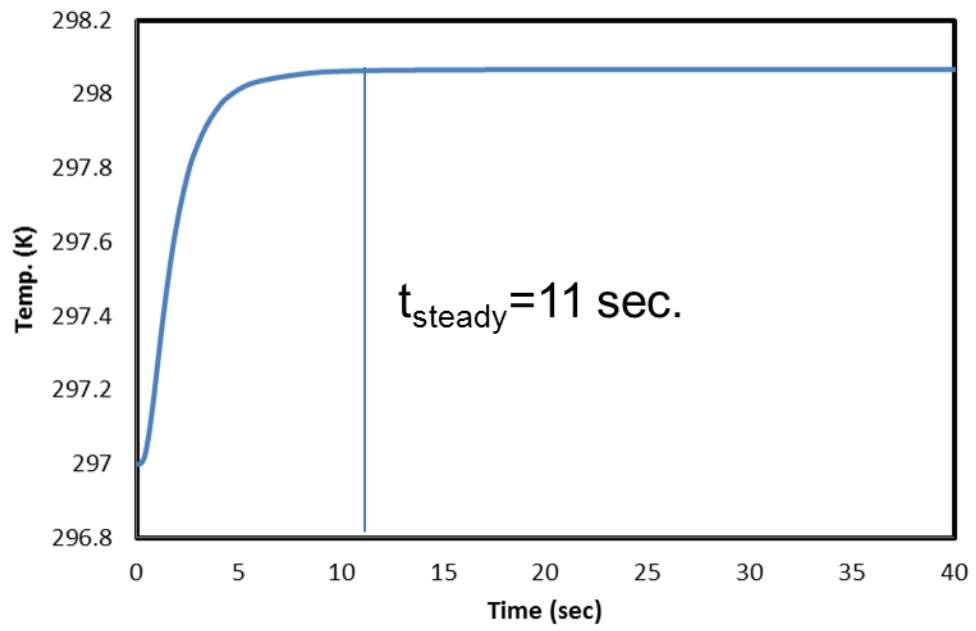


Figure 5.4 Cold side temperature with time of heating

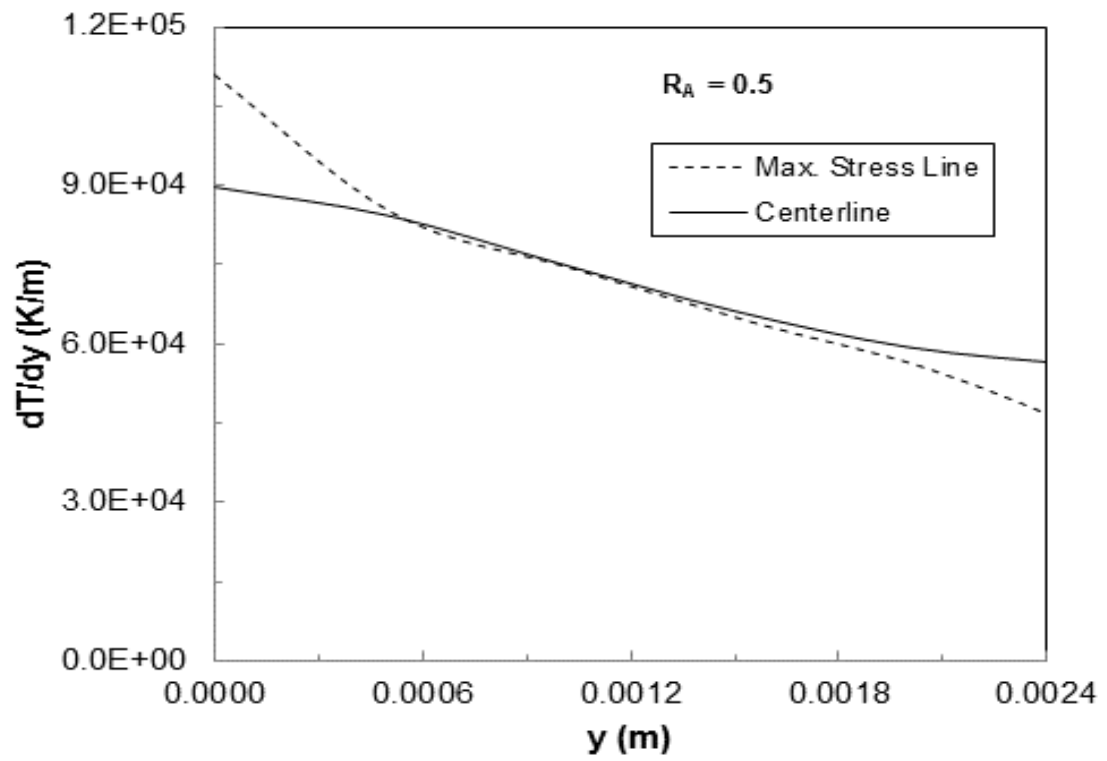


Figure 5.5 Temperature gradient along the centerline and the maximum stress line for $R_A = 0.5$.

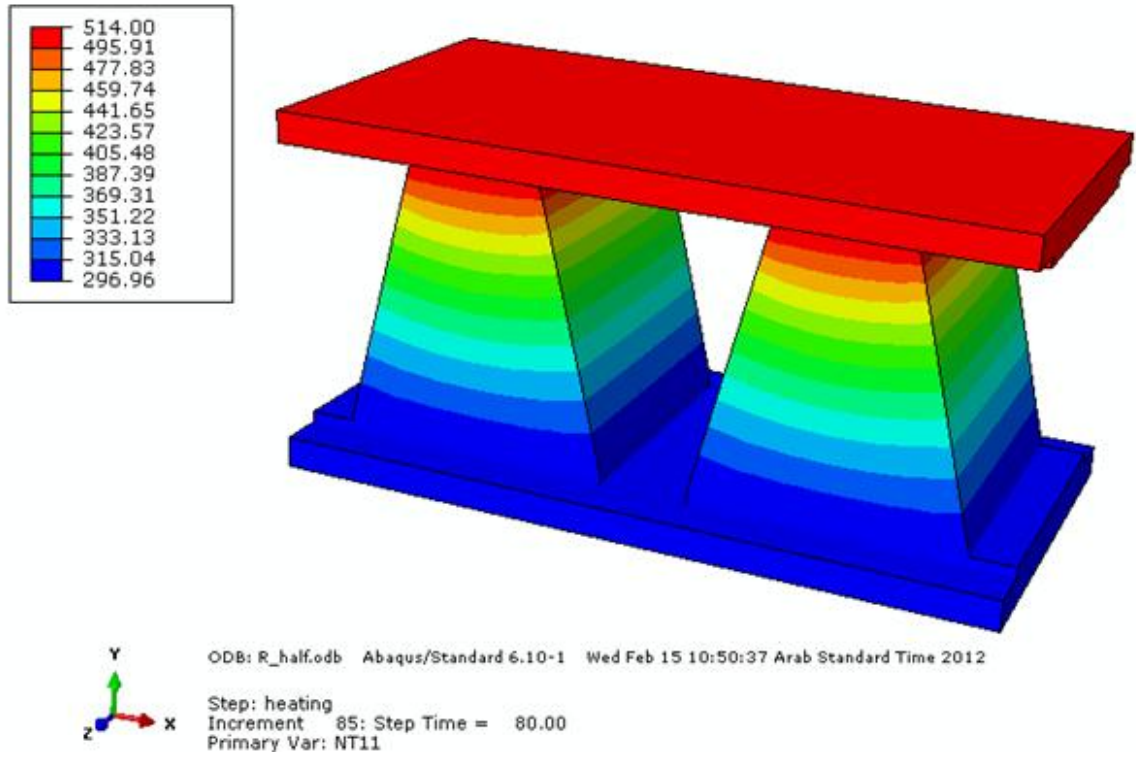


Figure 5.6 Three-dimensional temperature distribution in the thermoelectric generator for $R_A = 0.5$.

Figure 5.7 shows thermal stress variation along the centerline and the maximum stress line in the y-direction for $R_A = 0.5$. It is evident that thermal stress attains high values in the region of the hot junction which is particularly true along the maximum stress line. Thermal stress reduces sharply in the region close to the hot junction in the pin and its decay become gradual towards the cold junction. The sharp decay of thermal stress is attributed to attainment of high temperature gradients in this region.

Figure 5.8 and Figure 5.9 show thermal stress contours in the thermoelectric device and its pins. High stress region occurs locally in the pin, particularly at the edges of the pin where pin is attached to high temperature plate. The attainment of high stress is because of one on all of the following reasons:

- i) High temperature gradient developed in this region gives to high thermal stress levels,
- ii) The difference in thermal expansion coefficients due to pin and the hot plate which generates high stress levels at the interface location between the hot plate and the pin. Moreover, low stress region in the pin extends towards the cold junction region.

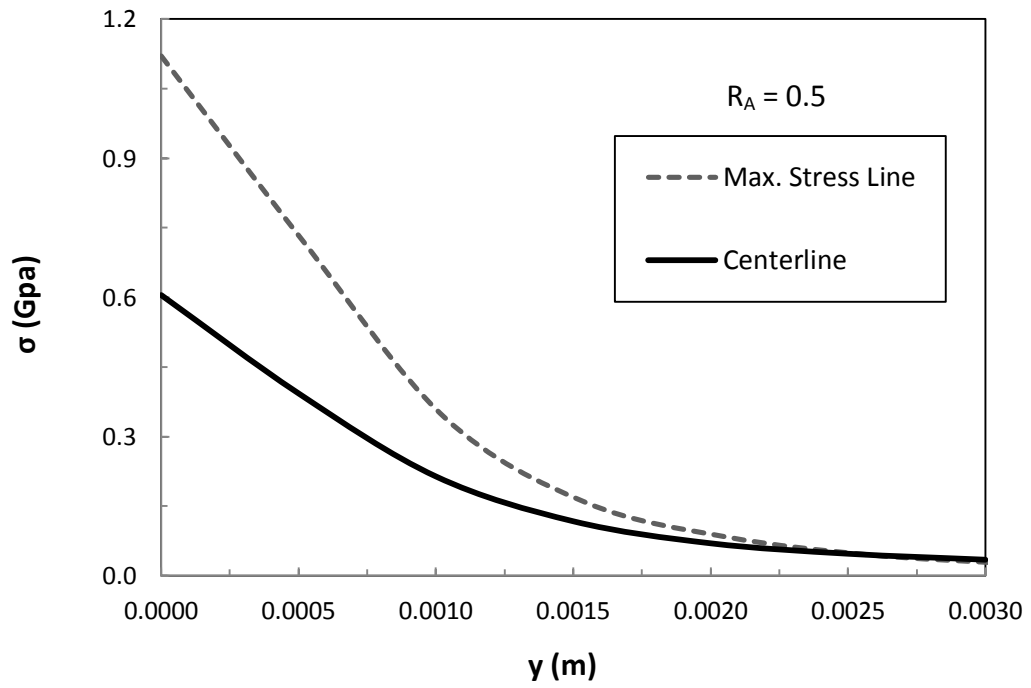


Figure 5.7 Thermal stress distribution along the centerline and the maximum stress line for $R_A = 0.5$.

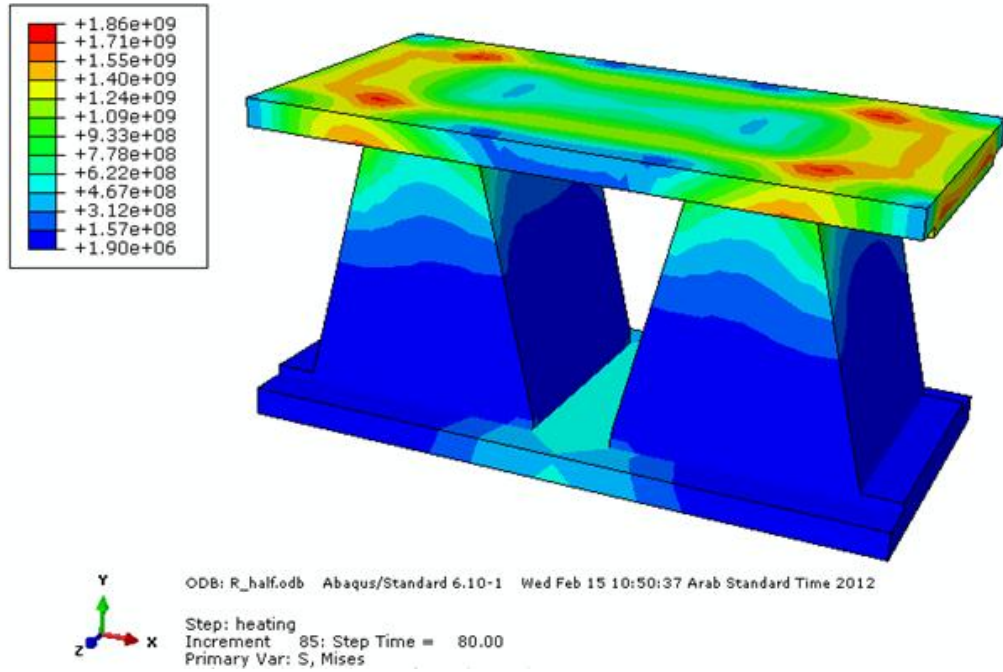


Figure 5.8 Three-dimensional thermal stress distribution in the thermoelectric generator for $R_A = 0.5$.

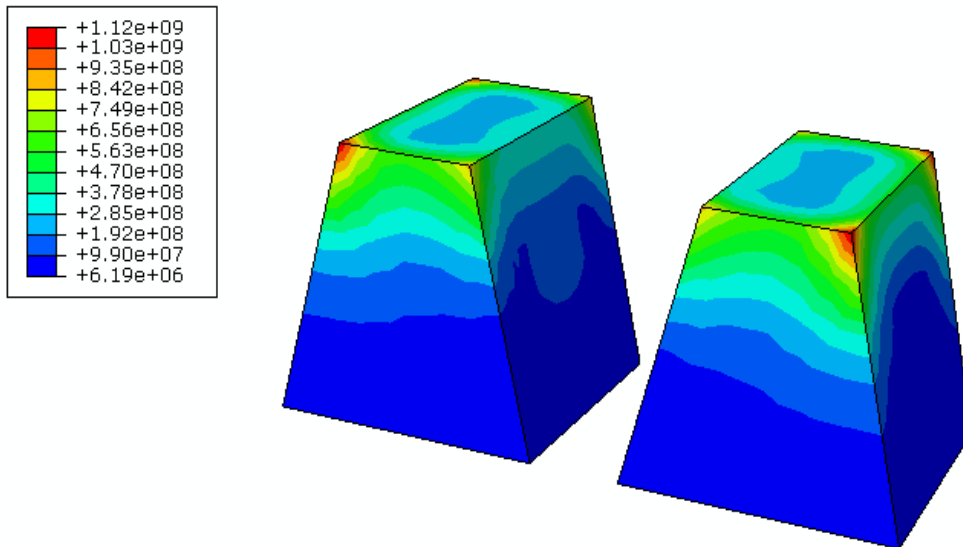


Figure 5.9 Three-dimensional thermal stress distribution in the thermoelectric pins for $R_A = 0.5$.

Figure 5.10 shows temperature distribution along the centerline and the maximum stress line along the y-axis for $R_A = 1$. It should be noted that $R_A = 1$ corresponds to rectangular parallel pin geometry. Temperature variation between the hot and the cold junctions along the both lines is gradual, provided that the temperature gradient changes significantly in the hot plate region for both lines (Figure 5.11). In this case the temperature gradient attains higher values in the vicinity of the hot plate, where $y \cong 0$, for the maximum stress line as compared to that corresponding to the centerline.

The high temperature gradient generates high strain in this region. Figure 5.12 shows temperature contours in the thermoelectric generator and the pins. It is evident that temperature variation along x and z-axes are almost uniform. However, temperature variation along the y-axis is large due to the presence of hot and cold plates across the pins.

Figure 5.13 shows thermal stress distribution along the centerline and the maximum stress line in the y-axis for $R_A = 1$. Thermal stress varies significantly along the both lines and stress reduces slightly in the region next to the hot plate and increases gradually with increasing distance towards the cold plate. However, thermal stress reduces sharply in the region close to the hot plate along the maximum stress line and the decay becomes gradual towards the cold plate. The attainment of high stress along maximum stress line is due to thermal expansion of the pin and high temperature gradient developed in the region close to the hot plate.

Figure 5.14 and Figure 5.15 show thermal stress counters in the thermoelectric generator and its pins, respectively. It can be observed that high stress region is locally developed towards the pin edges, particularly in the region next to the hot plate. However, thermal stress drops significantly towards to the cold plate due to attainment of the low temperature gradients in this region.

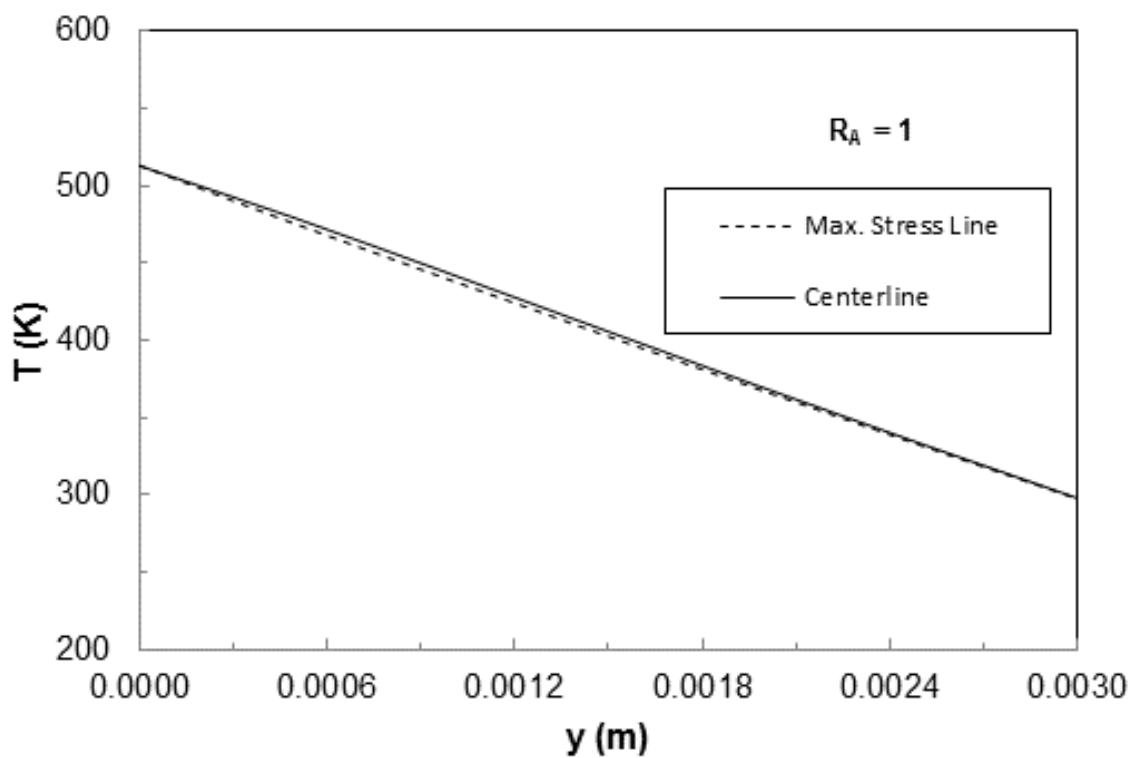


Figure 5.10 Temperature distribution along the centerline and the maximum stress line for $R_A = 1$.

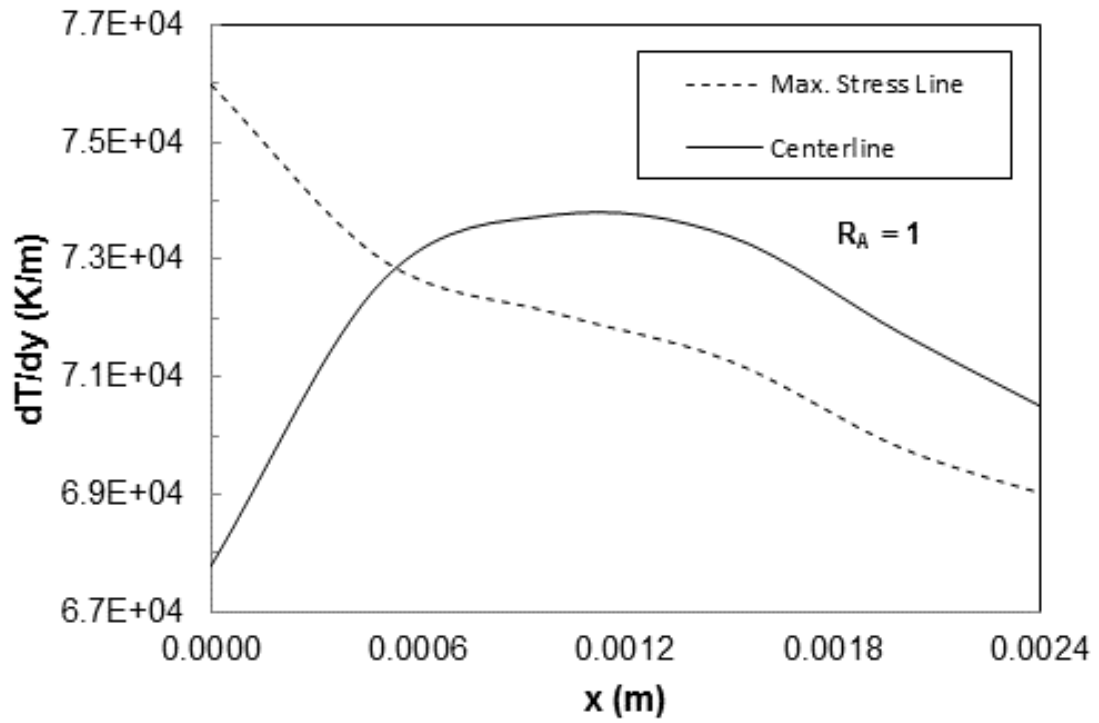


Figure 5.11 Temperature gradient distribution along the centerline and the maximum stress line for $R_A = 1$.

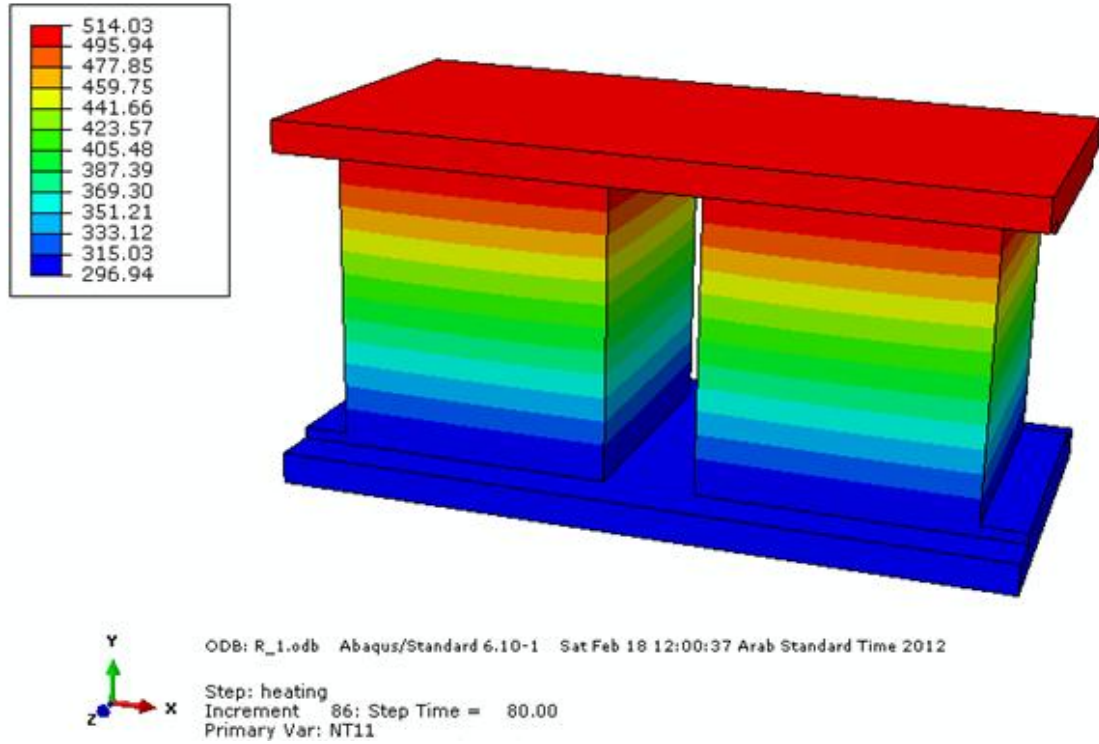


Figure 5.12 Three-dimensional temperature distribution in the thermoelectric generator for $R_A = 1$.

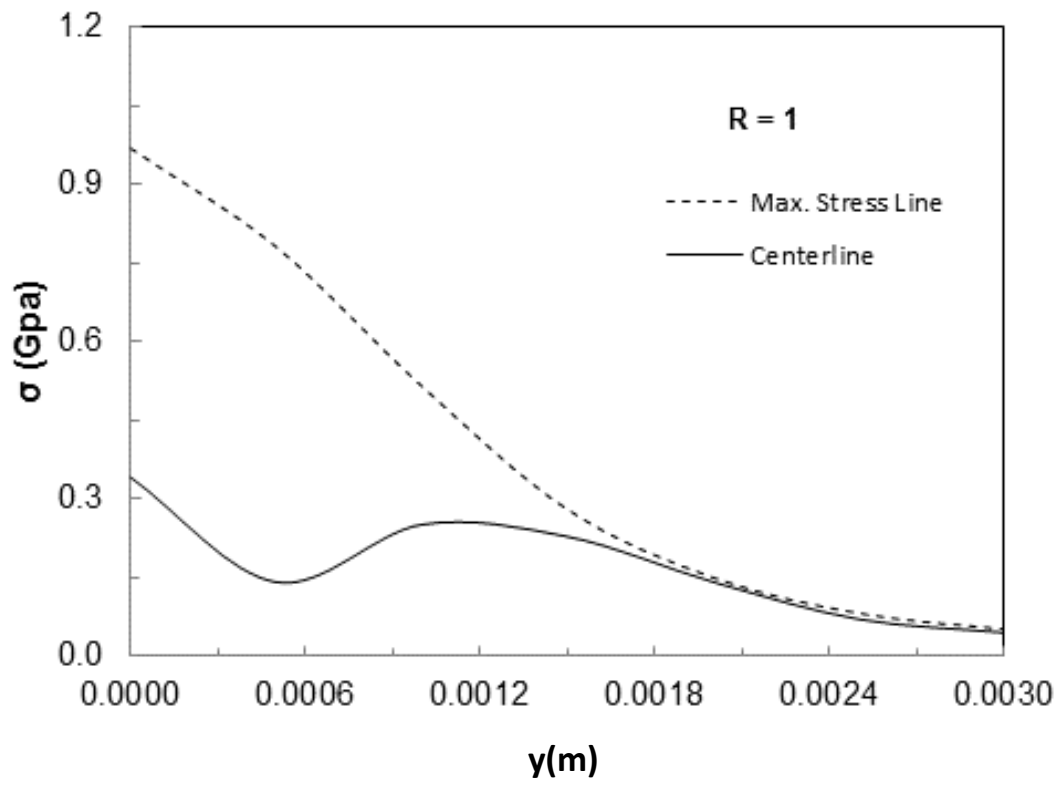


Figure 5.13 Thermal stress distribution along the centerline and the maximum stress line for $R_A = 1$.

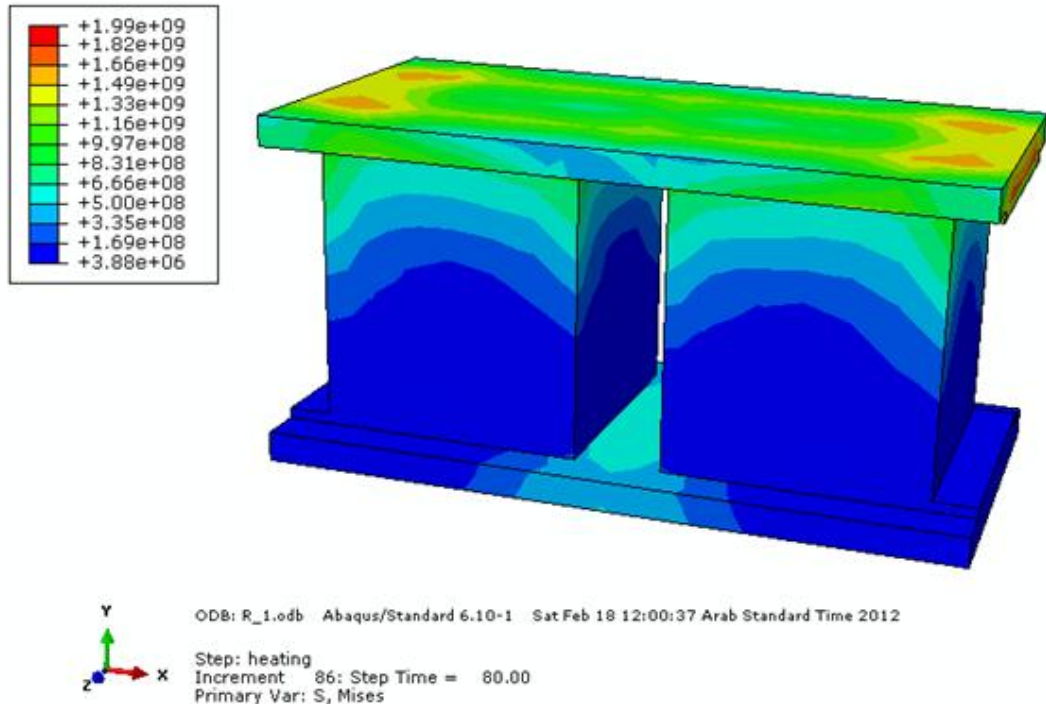


Figure 5.14 Three-dimensional thermal stress distribution in the thermoelectric generator for $R_A = 1$.

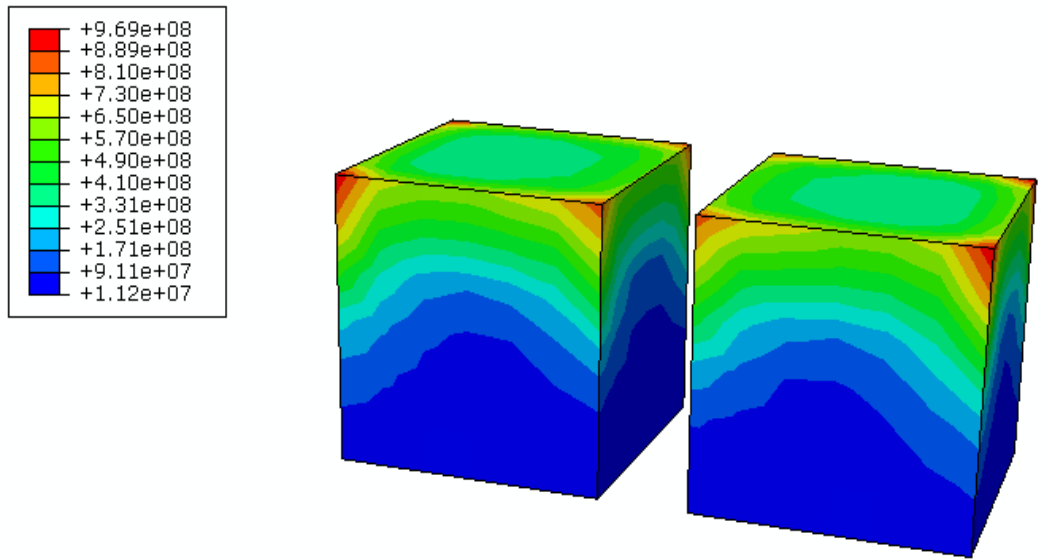


Figure 5.15 Three-dimensional thermal stress distribution in the thermoelectric pins for $R_A = 1$.

Figure 5.16 shows temperature distribution along the centerline and the maximum stress line in the y-axis for $R_A = 2$. Temperature decays gradually along the both lines from the high temperature plate to low temperature plate as similar those shown in Figure 5.2 and Figure 5.10. However, temperature along the maximum stress line attains slightly higher values than that of the centerline. This is associated with the heat conduction along the thermoelectric pins.

Moreover, the temperature gradient increases gradually towards the cold plate, which is associated with the gradual decay of temperature along the both lines (Figure 5.17). The temperature gradient along the maximum stress line is slightly lower than that of along the centerline. This indicates the attainment of relatively lower thermal strain along this line. Figure 5.18 shows temperature contours in the thermoelectric device and in the pins. Temperature variation is almost uniform along the x and z-axes as similar to those obtained for the cases $R_A = 0.5$ and $R_A = 1$.

Figure 5.19 shows von Mises Stress distribution along the centerline and the maximum stress line in the y-axis direction for $R_A = 2$. Thermal stress behavior is similar to that shown in Figure 5.10 for $R_A = 1$, provided that the maximum stress at $x = 0$ is less than that of $R_A = 1$. This is attributed to the differences in the temperature gradient behavior particularly in the region close to the hot plate.

Figure 5.20 and Figure 5.21 shows thermal stress contours in the thermoelectric generator and in the pins. Thermal stress is high in the region close to the hot plate and reduces sharply in the region close to the cold plate. The presence of high stress centers in the region of the pin edges is evident. This is attributed to the attainment of high temperature

gradient and thermal expansion coefficient differences between the hot plate and the pin material.

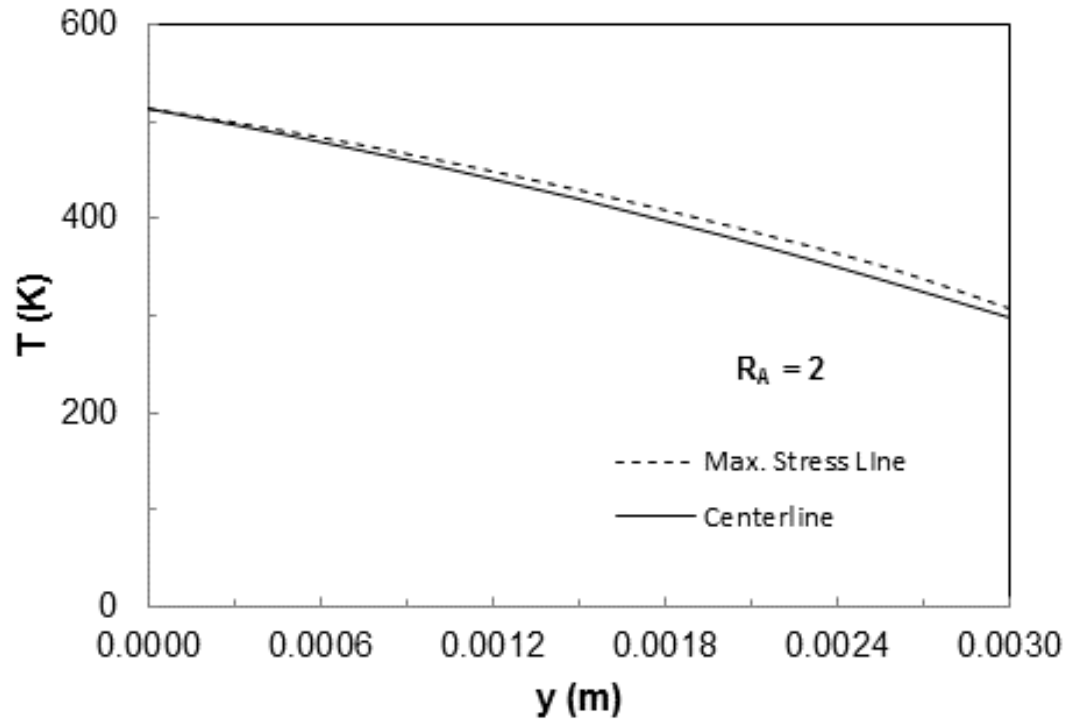


Figure 5.16 Temperature distribution along the centerline and the maximum stress line for $R_A = 2$

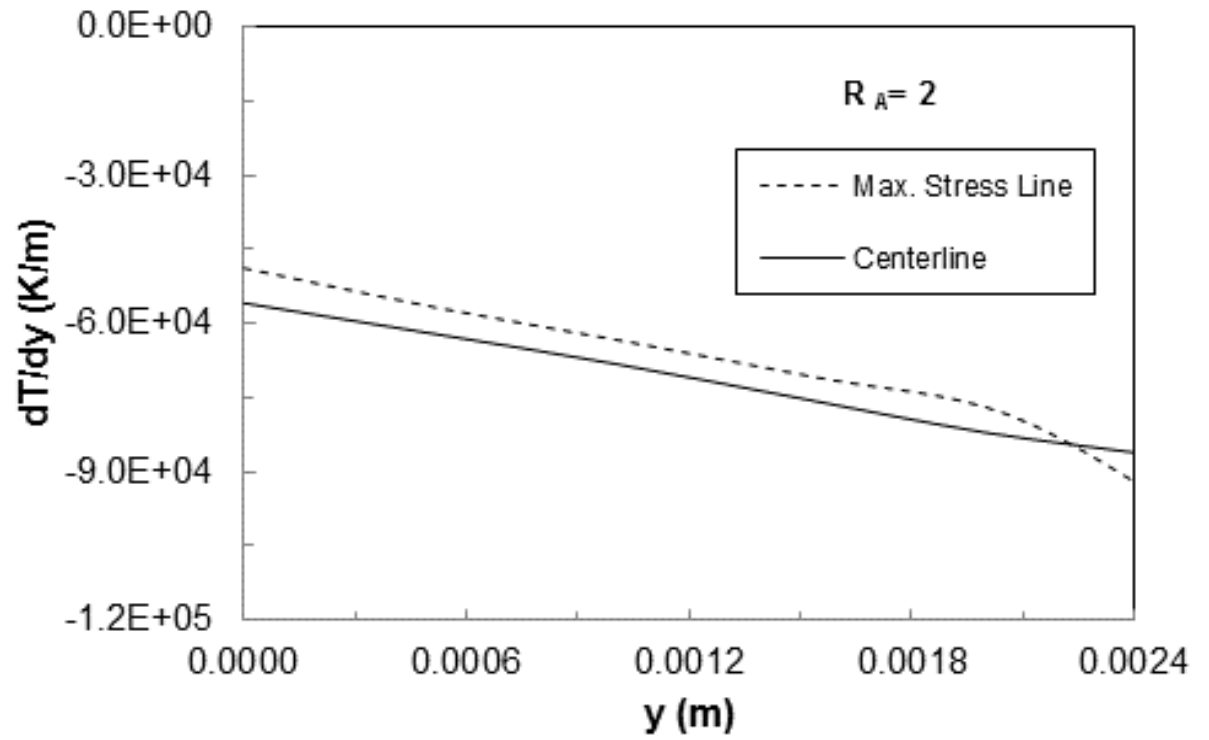


Figure 5.17 Temperature gradient distribution along the centerline and the maximum stress line for $R_A = 2$

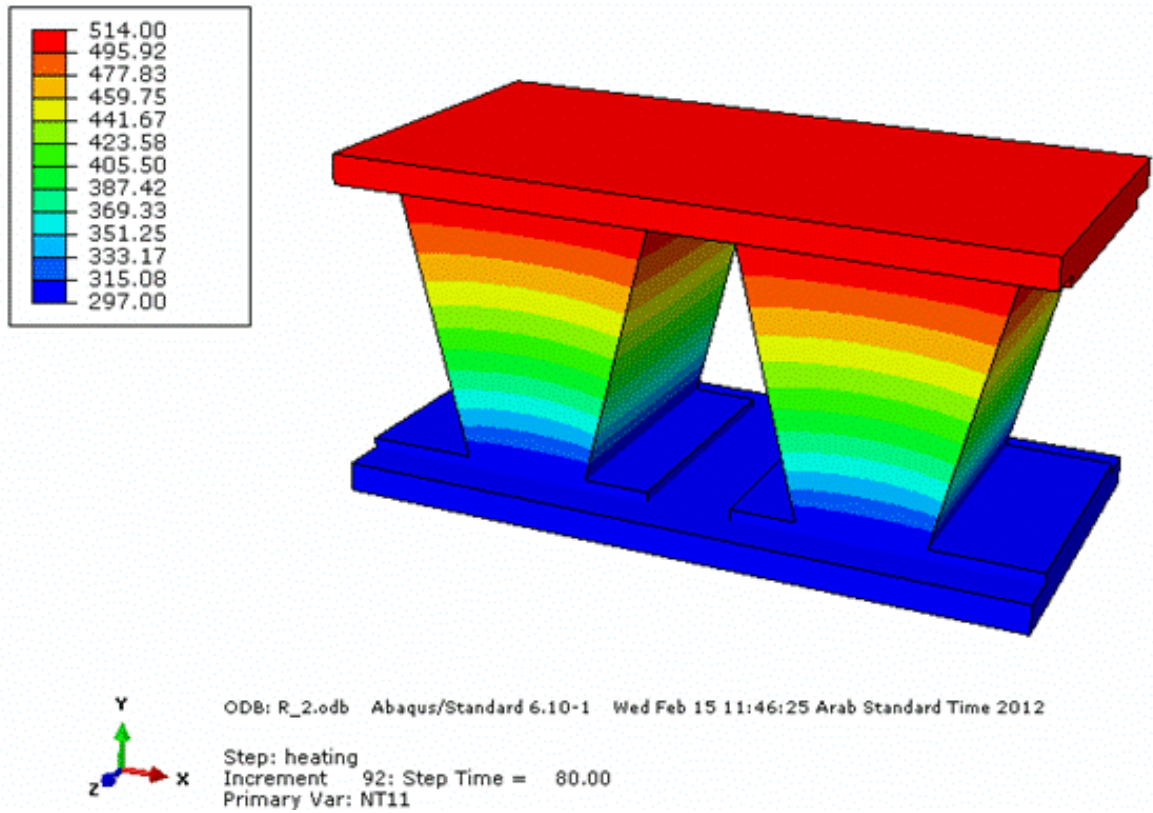


Figure 5.18 Three-dimensional temperature distribution in the thermoelectric generator for $R_A = 2$

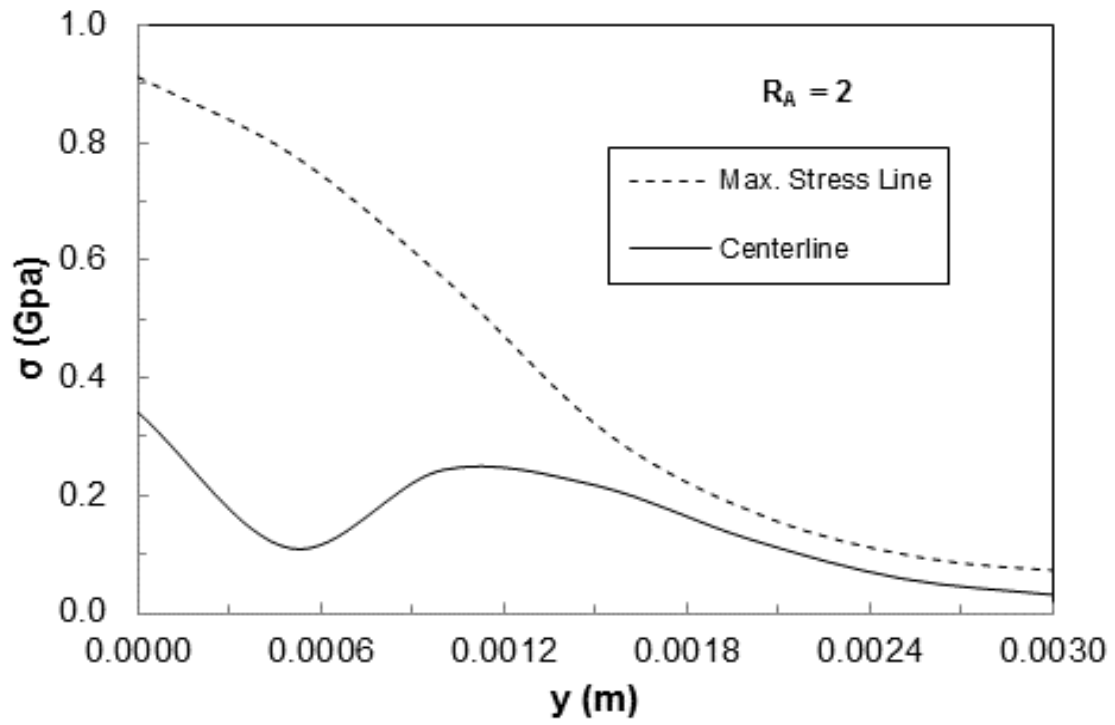


Figure 5.19 Thermal stress distribution along the centerline and the maximum stress line for $R_A = 2$

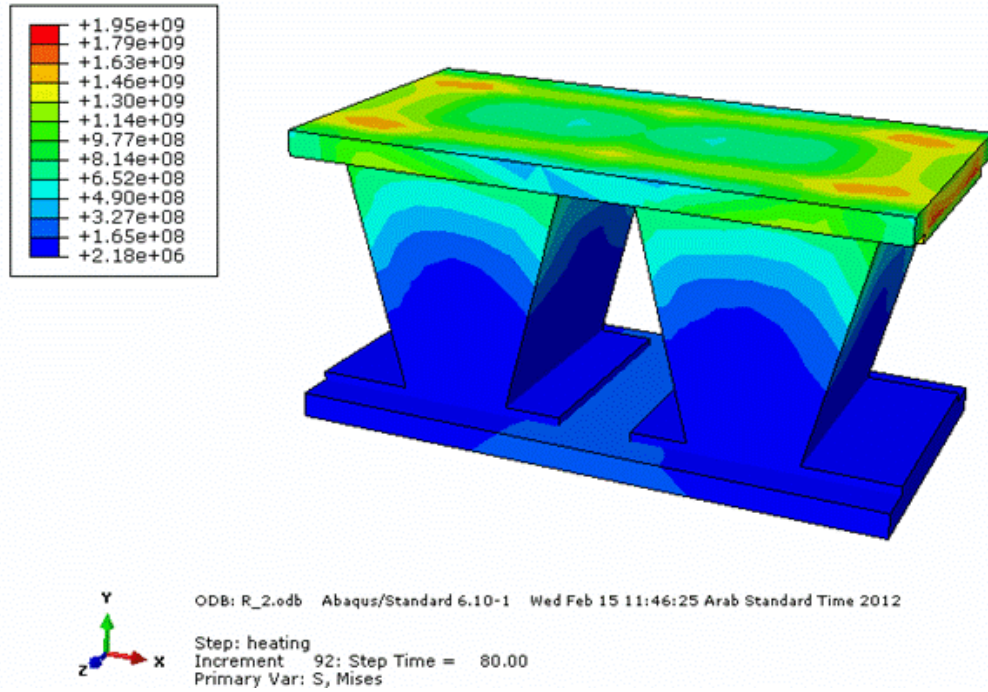


Figure 5.20 Three-dimensional thermal stress distribution in the thermoelectric generator for $R_A = 2$

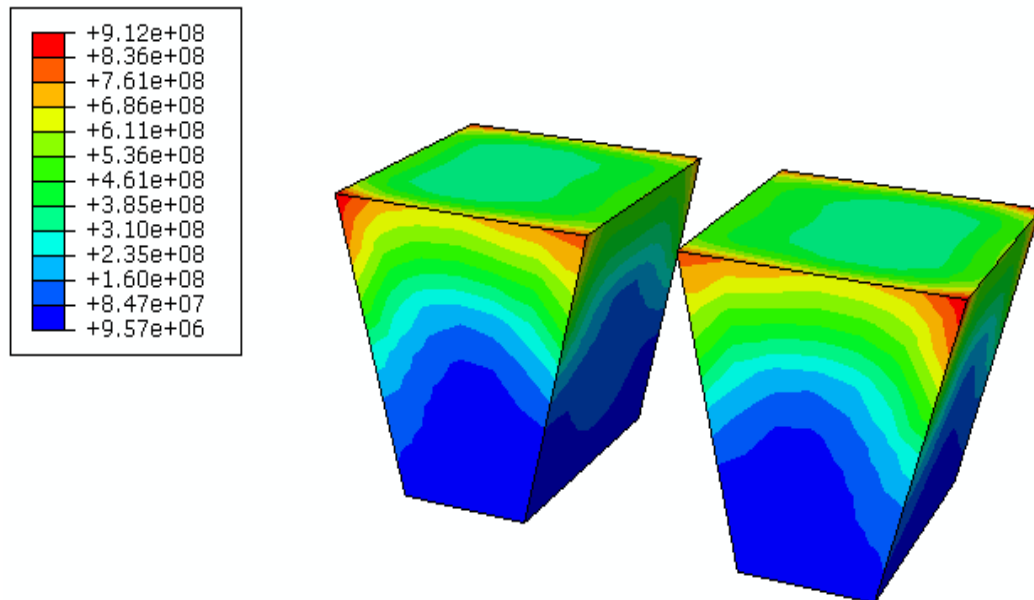


Figure 5.21 Three-dimensional thermal stress distribution in the thermoelectric pins for $R_A = 2$

Figure 5.22 shows temperature distribution along the centerline and the line where the maximum stress takes place in the y-direction. Temperature decays slowly along the both lines from the high temperature plate to low temperature plate. Temperature remains slightly high along the maximum stress line. Figure 5.23 shows temperature gradient along the maximum stress line and the centerline. Temperature gradient in the pin region close to the hot plate is higher than the mid-section of the pin. This is attributed to the pin cross-section, which is review. However, the temperature gradient increases forwards the cold plate. This is associated with the cold plate temperature, which is low, while creating the high temperature gradients in this region.

Figure 5.24 shows thermal stress developed along the centerline and the maximum stress line which Figure 5.25 shows the stress contours of thermoelectric generator and Figure 5.26 shows the stress contours of thermoelectric pins for bi-tapered configuration. The maximum stress reduces gradually along the maximum stress line in the region close to the hot plate and, this decrease becomes sharp as the distance along the maximum stress line increases. On the other hand, stress reduces sharply along the central line as compared to that of the maximum stress line.

Thermal stress reduces at location where temperature gradient is low. This is attributed to the small thermal strain developed at low temperature gradient. When comparing the stress levels for different configurations, thermal stress attains the minimum for the current geometric configuration as compared to other geometric configurations ($R_A = 1$, $R_A = 0.5$ and $R_A = 2$)

Table 5.1 gives the maximum values of thermal stress developed in the thermoelectric generator when the device operation reaches to steady state condition. The maximum thermal stress for the bi-tapered geometry is the minimum among the other cases.

This suggests that changing the design of the pins of the thermoelectric power generators from parallel to trapezoidal geometry, the maximum thermal stress developed can be reduced. Although the reduction is small, the life extension of the thermoelectric device is possible.

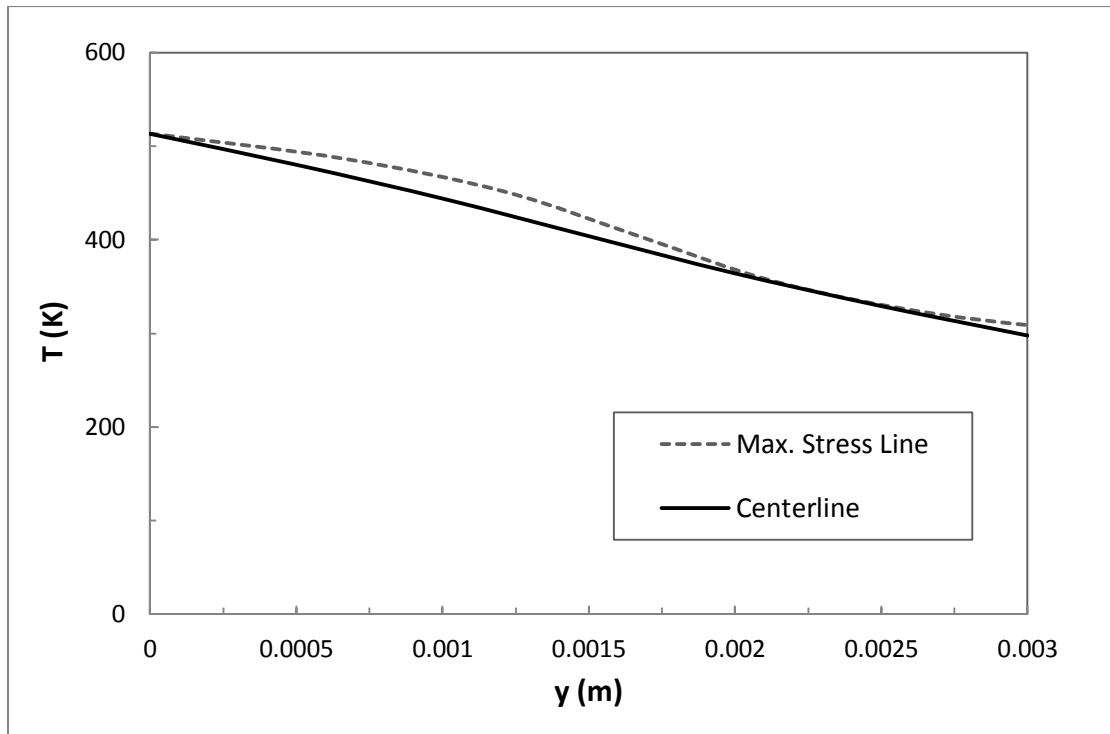


Figure 5.22 Temperature distribution along the centerline and the maximum stress line for bi-tapered

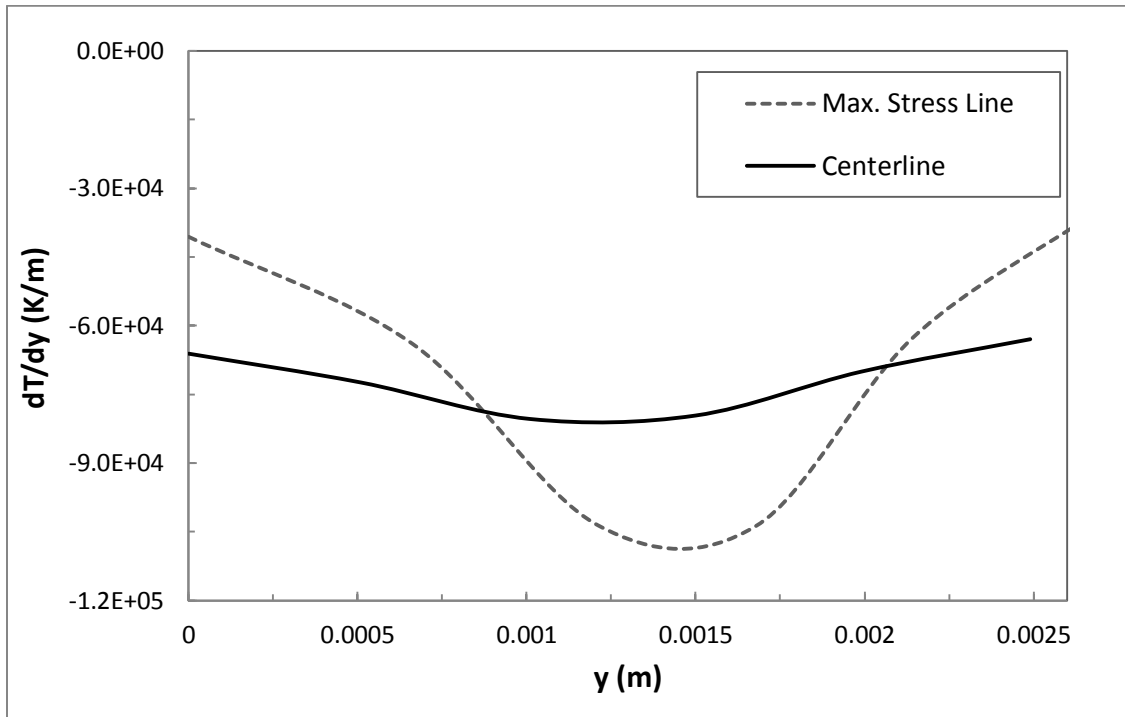


Figure 5.23 Temperature gradient distribution along the centerline and the maximum stress line for bi-tapered

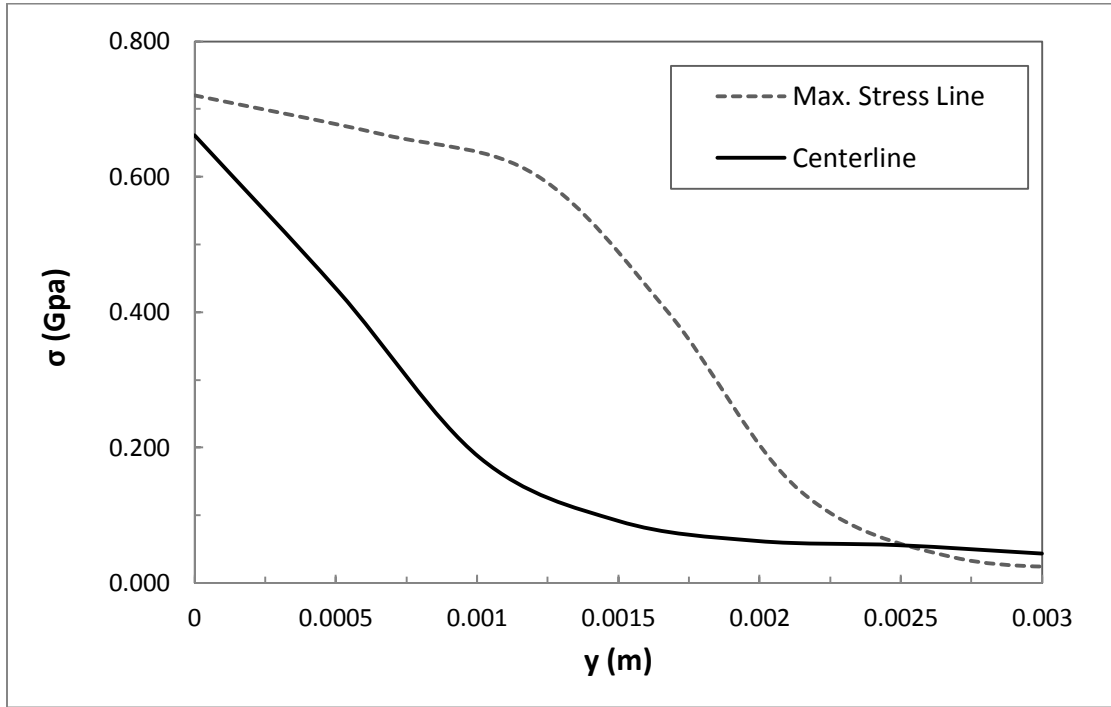


Figure 5.24 Thermal stress distribution along the centerline and the maximum stress line for bi-tapered

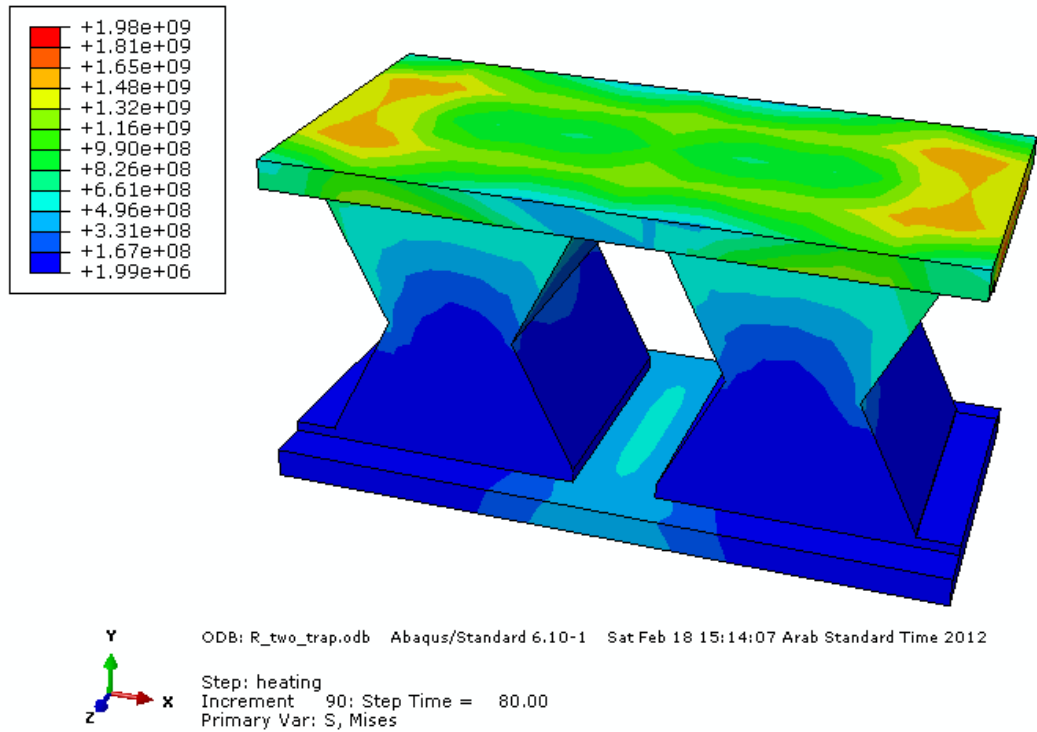


Figure 5.25 Three-dimensional thermal stress distribution in the thermoelectric generator for bi-tapered

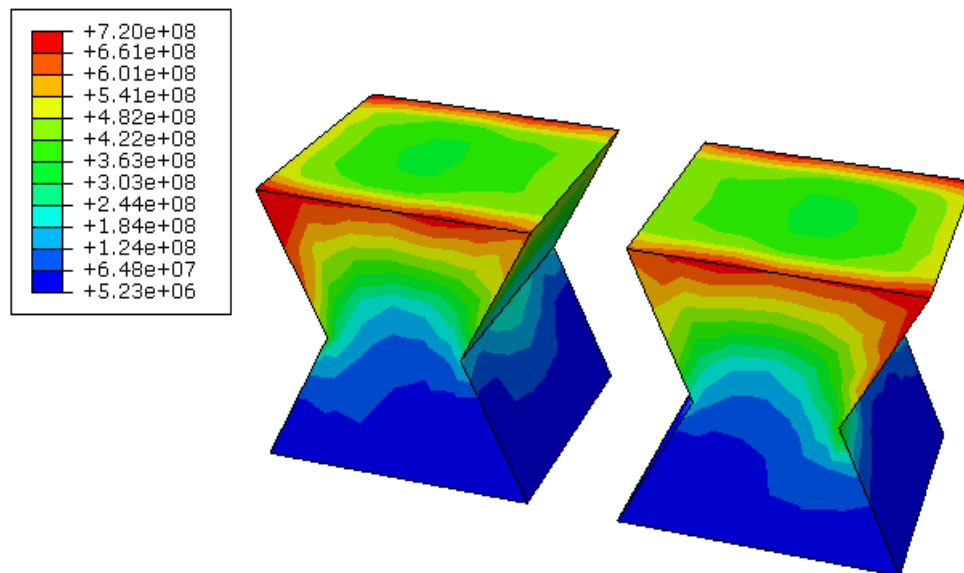


Figure 5.26 Three-dimensional thermal stress distribution in the thermoelectric pins for bi-tapered

Table 5.1 Comparison of the Maximum stresses developed in TE pin for different configurations

	$R_A = 0.5$	$R_A = 1$	$R_A = 2$	Bi-tapered
Max. Stress (Gpa)	1.12	0.969	0.912	0.72

5.3 Thermal cycling performance

Thermal cycling is carried out to analyze the residual stress in thermoelectric module generator by performing heating and cooling processes. The time of heating process is 80 seconds and for cooling is 120 seconds. The thermoelectric module was subjected to five heating-cooling cycles and the hot surface temperature was fluctuated from 24 to 240 C, while the cold side temperature was fixed to 24 C.

Figure 5.27 illustrates one heating-cooling cycle with a time needs to release a heat form thermoelectric pins, and became to the room temperature, of around 90 seconds. In total, five sequential heating-cooling cycles are performed with 1000 seconds as shown in Figure 5.28 (at maximum thermal-stress point).

The von Mises stress of one thermal cycle was fluctuating between the values of around 0.78 GPa and 1 MPa which is the residual stress as shown in Figure 5.29. Since the residual stress is relatively high after the heat is released from the TE module, performing heating and cooling cycles would be not a practical solution of reducing the thermal stress developed in TE module. Even though, it may create a thermal fatigue on the TE module and then, the life span of device may reduce.

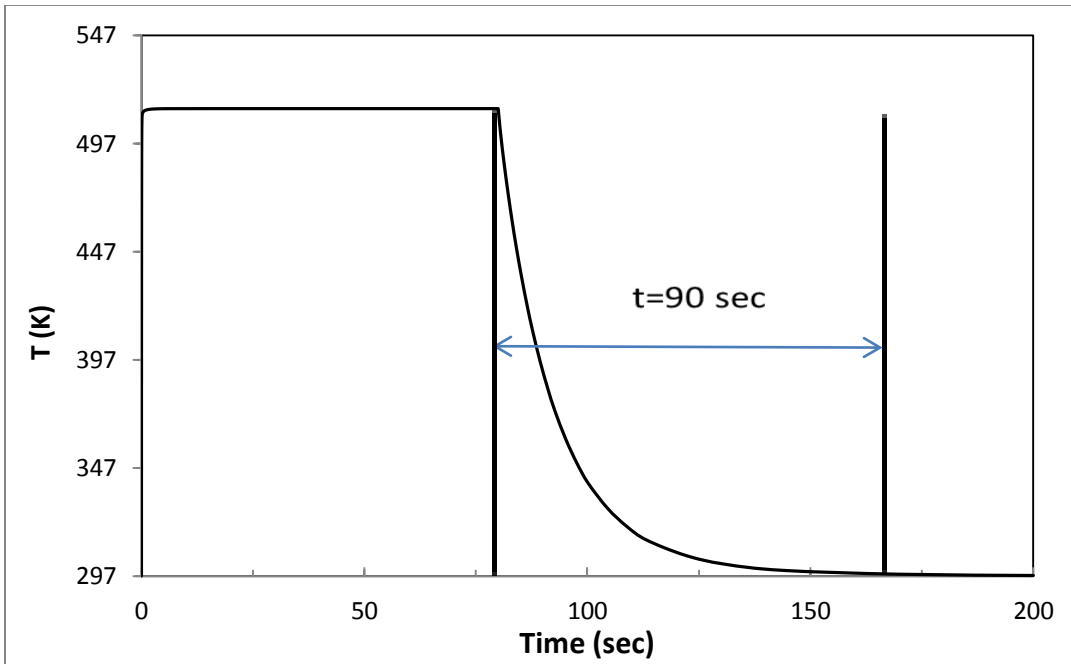


Figure 5.27 One Heating-cooling cycle (time=200 sec)

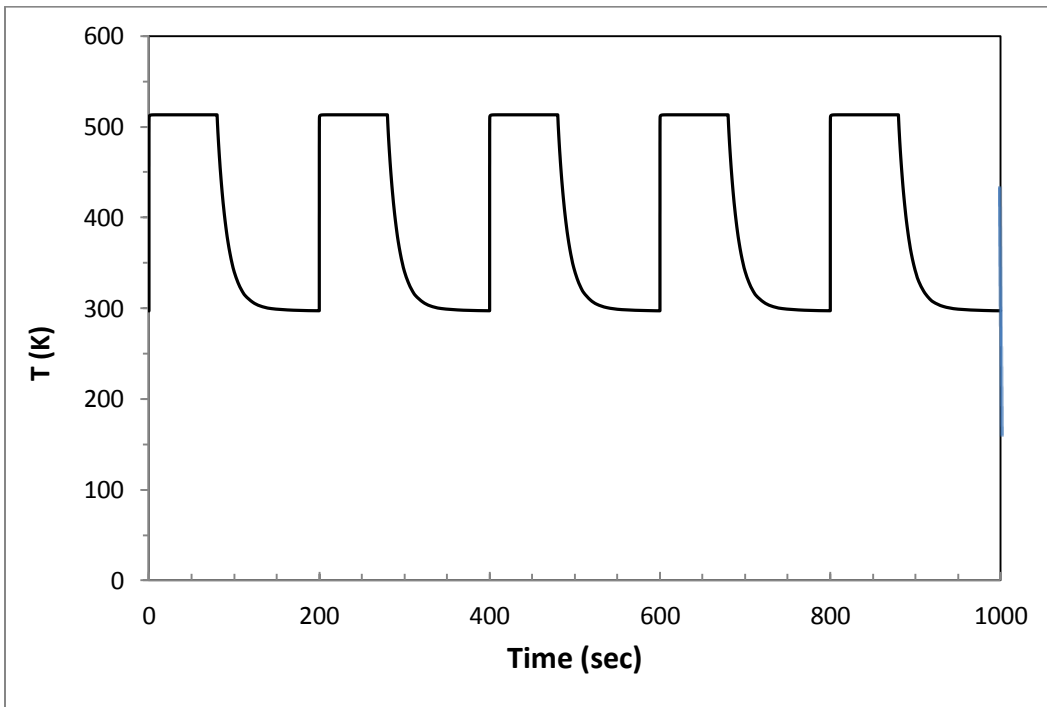


Figure 5.28 Temperature profile of the maximum stress point of five sequential heating-cooling cycles

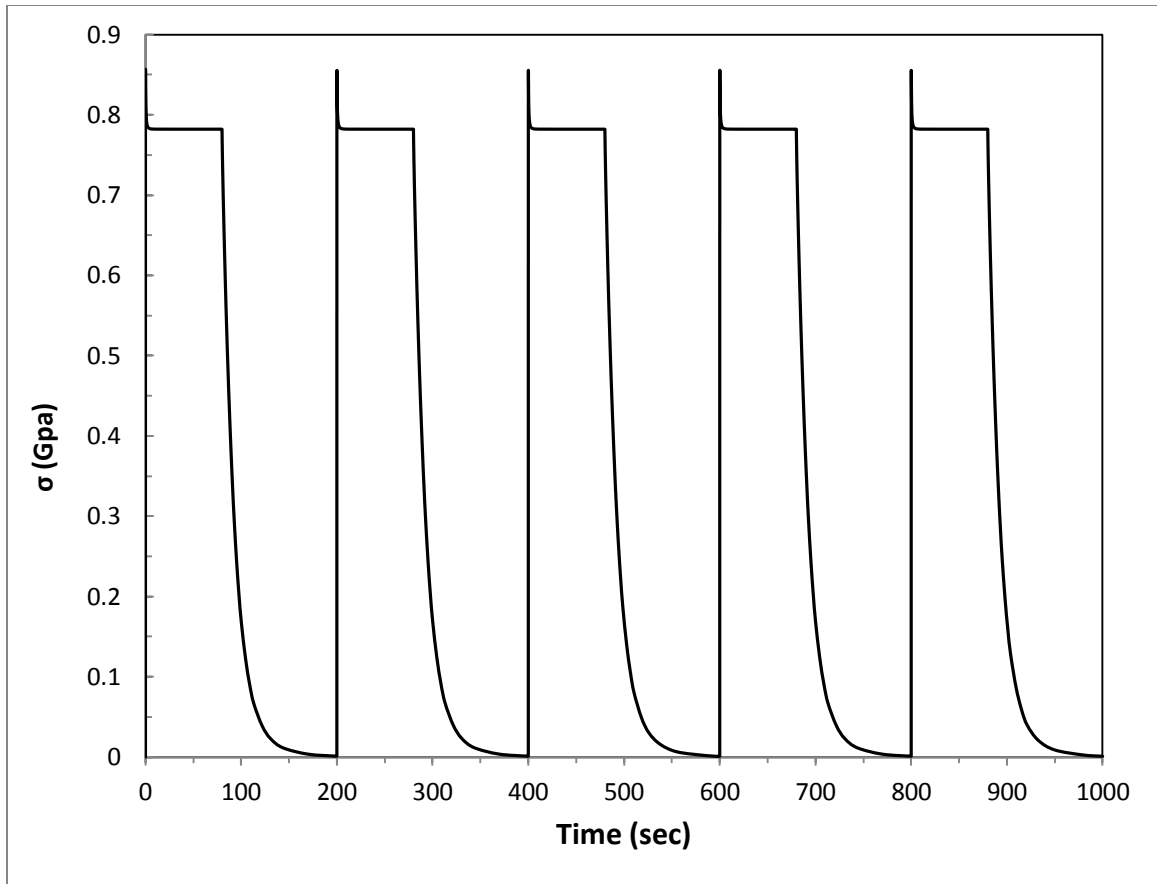


Figure 5.29 Thermal stress profile of the maximum stress point of five sequential heating-cooling cycles

CHAPTER 6

CONCLUSION AND RECOMMENDATION

Thermodynamic and thermal stress analysis of thermoelectric generator is carried out for various device pin configurations. In the analysis, the properties of Bi_2Te_3 thermoelectric material are used. It is found that thermal efficiency of the thermoelectric generator improves for $R_A = 0.5$ and $R_A = 2$. Although this improvement is small in the cases of ($R_A = 0.5$ and $R_A = 2$), its effect becomes high for the series operation of many thermoelectric devices. Temperature variation in the x,y plane does not alter significantly; in which case, almost uniform temperature distribution takes place along the pins. Temperature variation along the y-axis results in sharp decay of temperature in the region close to the hot plate. This gives rise to attainment of high temperature gradients in this region.

Thermal stress developed in the thermoelectric module and its pins varies for different configuration of pin geometry and the maximum stress occurs around the edges of the pins, which is more produced in the region close to the hot plate. The attainment of high stress levels in this region is attributed to the high temperature gradients and the mismatch of thermal expansion coefficients of the hot plate (welding layer) and the device pins.

The influence of pin geometry on temperature gradients and thermal stress is notable. In this case the pin with ($R_A = 2$) results in slightly low thermal stress in the pin. But, in case

of bi-tapered, the maximum thermal stress developed in TE pin reduced approximately 30 % comparing with the regular rectangular pin ($R_A=1$). This reduction resulted by the uniformity distribution of the stress developed due to the temperature variation.

The results indicate that changing the pin geometry improves temperature variation in the thermoelectric generator while suppressing the maximum stress levels in the pin. Consequently, life expectation of the device can be improved with geometric design of the device pins. In addition, for pin geometric configuration $R_A = 2$, thermal efficiency of the device also improves slightly but for the bi-tapered geometric configuration, the thermo-mechanical performance is improved considerably.

The thermal efficiency of thermoelectric generator module with different pin configurations ($R_A=0.5, 1, 2$) was investigated thoroughly in this thesis work. However, the thermal efficiency for bi-tapered pin configuration has to be analyzed with deriving a specific equation of efficiency.

Another direction in which the work of thermal stress of thermoelectric generator can be extended is to incorporate the variable material properties of TE pins during the heating-cooling cycles. This will affect the residual stress developed in TE pins through these cycles.

NOMENCLATURE

V	Electrical potential [V]
S	Seebeck coefficient [$V K^{-1}$]
q	Rate of heat generation [W]
I	Electric current [A]
Z	Figure of merit [K^{-1}]
k	Thermal conductivity [$W m^{-1} K^{-1}$]
R	Electric resistance [Ω]
R_L	External load resistance [Ω]
A_0	Cross-sectional area of the uniform rectangular pin [m^2]
A_H	Top side cross-sectional area [m^2]
A_L	Bottom side cross-sectional area [m^2]
R_A	Ratio between the top (hot side) to bottom (cold side) Area
L	Height of the pin [m]
r_k	Thermal conductivity ratio
r_σ	Electrical conductivity ratio
K_0	Reference thermal conductance
R_0	Reference electrical resistance
c_p	Specific heat capacity [$J kg^{-1} K^{-1}$]

T	Absolute temperature [K]
t	Time [sec]
E	Young's modulus of elasticity [MPa]
ν	Poisson's ratio
h	Heat transfer coefficient [$\text{W m}^{-2} \text{K}^{-1}$]
T_a	Ambient temperature [K]

Greek Symbols

π	Peltier coefficient [V]
β	Thomson coefficient [V K^{-1}]
σ	Electrical conductivity [S m^{-1}]
ρ	Density [kg m^{-3}]
θ	Temperature ratio
α	Coefficient of linear thermal expansion [K^{-1}]
ϵ	Emissivity of the surface

References

- [1] U.S Energy Information Administration," <http://www.eia.gov/electricity/monthly>"
- [2] Caltech Material Science website; Thermoelectrics "*Brief History of Thermoelectrics*"
"<http://www.thermoelectrics.caltech.edu/>"
- [3] E. Weston. U.S. Patent No. 389,124 (1888)
- [4] W. W. Coblenz. U.S. Patent No. 1,077,219 (1913)
- [5] M. V. Vedernikov and E. K. Iordanishvili "*A. F. Ioffe and origin of modern semiconductor thermoelectric energy conversion*" 17th Int. Conf. Thermoelectrics Vol. 1, 37 (1998)
- [6] M. Telkes. "*Solar thermoelectric generators*" J. Appl. Phys. Vol. 25, 765 (1954)
- [7] H. J. Goldsmid and R. W. Douglas "*The use of semiconductors in thermoelectric refrigeration*" J. Appl. Phys. 5, 386 (1954)
- [8] Rowe, D. M. "*Handbook of Thermoelectrics; Macro to Nano*" (CRC Press, 2006)
- [9] Science Buddies website; "http://www.sciencebuddies.org/science-fair-projects/project_ideas/Elec_p055.shtml"
- [10] G. J. Snyder and E. S. Toberer "*Complex thermoelectric materials*" Nature Materials Vol. 7, 105 (2008)
- [11] Rowe, D.M. "*Thermoelectric power generation*" Proc. IEE, Vol. 125, 11R, Review (1978)
- [12] Wright, D. A. "*Materials for direct-conversion thermoelectric generators*" Metallurgical Reviews, Vol. 15, pp. 147-160 (1970)

- [13] C. Wood *"High-Temperature thermoelectric energy conversion II"* Energy Con. Vol. 24, 331 (1984)
- [14] D. G. Cahill, S. K. Watson and R. O. Pohl, *"Lower limit to the thermal conductivity of disordered crystals"*, Phys. Rev. Vol. 46, 6131 (1992)
- [15] Rowe, D.M. and Bhandari, C.M. *"Modern thermoelectric"* Holt, Rinehart and Winston, London, p. 103 (1983)
- [16] Caillat T, Borshchevsky A, and Fleurial J.P. *"Investigations of several new advanced thermoelectric materials at the jet propulsion laboratory"* Atlanta, Georgia, US. 245-248 (1993)
- [17] L. Zhao, Bo. Zhang a, J. Li, M. Zhou, W. Liu and J. Liu *"Thermoelectric and mechanical properties of nano-SiC-dispersed Bi₂Te₃ fabricated by mechanical alloying and spark plasma sintering"* J. Alloys & Compd. Vol. 455, 259 (2008)
- [18] B. Poudel, Q. Hao, Y. Ma, Y. Lan, A. Minnich, B. Yu, X. Yan and D. Wang *"High-Thermoelectric Performance of Nanostructured Bismuth Antimony Telluride Bulk Alloys"* Science 320, 634 (2008)
- [19] D. Polvani, J. Meng, N. Shekar, J. Sharp, and J. Badding, *"Large Improvement in Thermoelectric Properties in Pressure-Tuned p-Type Sb_{1.5}Bi_{0.5}Te₃"* Chem. Mater. Vol. 13, 2068 (2001)
- [20] K. F. Hsu, S. Loo, F. Guo, W. Chen J. S. Dyck, C. Uher, T. Hogan, E. K. P Polychroniadis and M. G. Kanatzidis *"Cubic AgPbmSbTe_{2+m}: Bulk Thermoelectric Materials with High Figure of Merit"*, Science Vol. 303, 818 (2004)

- [21] E. Koukharenko, N. Frety, V.G. Shepelevich, and J.C. Tedenac "*Thermoelectric properties of Bi₂Te₃ material obtained by the ultra rapid quenching process route*" J. Alloys & Compd. Vol. 299, 254 (2000)
- [22] P. Zhu, X. Jia, H. Chen, W. Guo, L. Chen, D. Li, H. Ma, G. Ren, and G. Zou "*A new method of synthesis for thermoelectric materials*" Solid State Commune. Vol. 123, 43 (2002)
- [23] R. Song, T. Aizawa, and J. Sun "*Synthesis of Mg₂Si_{1-x}Sn_x solid solutions as thermoelectric materials by bulk mechanical alloying and hot pressing*" Materials Science and Eng. B Vol. 136 ,111 (2007)
- [24] C. Zhou., D. Morelli., X. Zhou, G. Wang and C. Uher "*Thermoelectric properties of P-type Yb-filled skutterudite Yb_xFe_yCo_{4-y}Sb₁₂*" Intermetallics Vol. 19, 1390 (2011)
- [25] G. Lamberton, S. Bhattacharya, R. Littleton, M. Kaeser, R. Tedstrom, and T. Tritt, "*High figure-of-merit in Eu-filled CoSb₃-based skutterudites*" Appl. Phys. Letters Vol. 80, 598 (2002)
- [26] G. S. Nolas and G.A Slack "*Thermoelectric clathrates*" Am. Sci., Vol. 89, 136 (2001)
- [27] Ioffe, A. "*Semiconductor Thermoelements and Thermoelectric Cooling*" Info. Search London (1956)
- [28] Y. S. Ju and U. Ghoshal "*Study of interface effects in thermoelectric micro-refrigerators*" J. Appl. Phys. Vol. 88, 4135 (2000)

- [29] V. S. Zakordonets and G. N. Logvinov “*Thermoelectric figure of merit of monopolar semiconductors with finite dimensions*”, Semiconductors 31, 265 (1997)
- [30] L. D. Hicks and M. S. Dresselhaus “*Effect of quantum-well structures on the thermoelectric figure of merit*”, Phys. Rev. 8, Vol. 47, 727 (1993)
- [31] T. C. Harman, P. J. Taylor, M. P. Walsh, and B. E. LaForge “*Quantum dot superlattice thermoelectric materials*” Science Vol. 297, 2229 (2002)
- [32] R. Venkatasubramanian, E. Silvola, T. Colpitts, and B. O’Quinn “*Thin-film thermoelectric devices with high room temperature figures-of-merit*” Nature Vol. 413, 597 (2001)
- [33] U. Ghoshal, S. Ghoshal, C. McDowell, L. Shi, S. Cordes, and M. Farinelli, “*Enhanced thermoelectric cooling at cold junction interfaces*” Appl. Phys. Letters Vol. 80, 3006 (2002)
- [34] A. Dauscher, A. Thomy, H. Scherrer “*Pulsed laser deposition of Bi₂Te₃ thin films*”, Thin Solid Films Vol. 280, 61 (1996)
- [35] M. Takashiri, K. Miyazaki, H. Tsukamoto “*Structural and thermoelectric properties of fine-grained Bi_{0.4}Te_{3.0}Sb_{1.6} thin films with preferred orientation deposited by flash evaporation method*” Thin Solid Films Vol. 516, 6336 (2008)
- [36] Z. H. Zheng, P. Fan, G. X. Liang, D. P. Zhang, X. M. Cai and T. B. Chen “*Annealing temperature influence on electrical properties of ion beam sputtered Bi₂Te₃ thin films*” J. Phys. & Chem. of Solids Vol. 7, 1713 (2010)

- [37] H. Noro, K. Sato, and H. Kagechika "The thermoelectric properties and crystallography of Bi-SbTe-Se thin films grown by ion beam sputtering" J. Appl. Phys. Vol. 73, 1252 (1993)
- [38] C. Liao and T. She "Preparation of bismuth telluride thin films through interfacial reaction" Thin Solid Films Vol. 515, 8059 (2007)
- [39] A. Giani, F. Pascal-Delannoy, A. Boyer, A. Foucaran, M. Gschwind, and P. Ancey "Elaboration of Bi_2Te_3 by metal organic chemical vapor deposition" Thin Solid Films Vol. 303, 1 (1997)
- [40] Y. Miyazaki and T. Kajitani "Preparation of Bi_2Te_3 films by electro-deposition" J. Crystal Growth Vol. 229,542 (2001)
- [41] H. Zou, D.M. Rowe and G. Min "Growth of p- and n-type bismuth telluride thin films by co-evaporation", J. Crystal Growth Vol. 222, 82 (2001)
- [42] L. Onsager, "Reciprocal Relations in Irreversible Processes. I." Phys. Rev. Vol. 37, 405 (1931)
- [43] C. A. Domenicali. "Irreversible thermodynamics of thermoelectric effects in inhomogeneous, anisotropic media" Phys. Rev. Vol. 92, 877 (1953)
- [44] M. J. Lampinen "Thermodynamic analysis of thermoelectric generator" J. Appl. Phys. Vol. 69, 4318 (1991)
- [45] M. Kassas "Thermodynamic Analysis of Thermoelectric Device" International J. EXERGY, Vol. 4, 168 (2007)

- [46] J. Chen, Z. Yan and L. Wu "Nonequilibrium Thermodynamic Analysis of A thermoelectric Device" Energy Vol. 22, 979 (1997)
- [47] O. Yamashita "*Effect of linear temperature dependence of thermoelectric properties on energy conversion efficiency*" Energy Conv. Manage. Vol. 39, 3163 (2008)
- [48] S. L. Li, C. K. Liu, C. Y. Hsu, M. C. Hsieh M. J. Dai and S. T. Wu "*Thermo-mechanical Analysis of Thermoelectric Modules*" 5th Inter. Conf. (IMPACT), 1 (2010)
- [49] J. Gao, Q. Du, X. Zhang and X. Jiang "*Thermal Stress Analysis and Structure Parameter Selection for a Bi₂Te₃-Based Thermoelectric Module*" J. Electronic Material, Vol. 40, 884 (2011)
- [50] Y. Hori, D. Kusano, T. Ito and K. Izumi "*Analysis on thermo-mechanical stress of thermoelectric module*" 18th Inter. Conf. Thermoelectrics, 328 (1999)
- [51] M. Huang, P. Chou and M. Lin "*Thermal and thermal stress analysis of a thin-film thermoelectric cooler under the influence of the Thomson effect*" Sensor and Actuators A Vol. 126, 122 (2006)
- [52] S. Turenne, T. Clin, D. Vasilevskiya and R. A. Masut, "*Finite element Thermomechanical modeling of large area thermoelectric generators based on bismuth telluride alloys*" J. Electronic Materials, Vol. 39, 1926 (2010)
- [53] J. Yang, R. Chen, X. Fan, W. Zhu, S. Bao and X. Duan "*Microstructure control and thermoelectric properties improvement to n-type bismuth telluride based materials by hot extrusion*" J. Alloys and Comp. Vol. 429, 156 (2007)

- [54] E. Hatzikraniotis, K. Zorbas, I. Samaras, T. Kyratsi and K. Paraskevopoulos "Efficiency Study of a Commercial Thermoelectric Power Generator (TEG) Under Thermal Cycling" J. Electronic Material, Vol. 39, 2112 (2010)
- [55] V. Ravi, S. Firdosy, T. Caillat, E. Brandon, K. Walde, L. Maricic, and A. Sayir "Thermal expansion studies of selected high-temperature thermoelectric materials" J. Electronic Materials, Vol. 38, 1433 (2009)
- [56] E. Antonova and D. Looman "Finite Elements for Thermoelectric Device Analysis in ANSYS" Inter. Conf. on Thermoelectrics 200 (2005)
- [57] A. Sisman and H. Yavuz "The effect of joule losses on the total efficiency of a thermoelectric power cycle" Energy Vol. 20, 573 (1995)
- [58] S. Ozkaynak and S. Goktun "Effect of irreversibilities on the performance of thermoelectric generator" Energy Conv. Vol. 35, 1117 (1994)
- [59] L. Chen, J. Gong, F. Sun and C. Wu "Effect of heat transfer on the performance of thermoelectric generators" Int. J. Therm. Sci. Vol. 41, 95 (2002)
- [60] A. Z. Sahin, B. S. Yilbas, S. Z. Shuja, O. Momin "Investigation into topping cycle: Thermal efficiency with and without presence of thermoelectric generator" Energy Vol. 36, 4048 (2011)
- [61] G. Rockendore, R. Sillmann, L. Podlowski and B. Litzenburger "PV-hybrid and Thermoelectric Collector" Solar Energy, Vol. 67, 227 (1999)
- [62] J. Esarte, G. Min and D.M. Rowe "Modeling heat exchangers for thermoelectric generators" J. Power Sources Vol. 93, 72 (2001)

- [63] D. Astrain , J. G. Vian and M. Dominguez *"Increase of COP in the thermoelectric refrigeration by the optimization of heat dissipation"* App. Thermal Engineering Vol. 23, 2183 (2003)
- [64] M. Kubo, M. Shinoda, T. Furuhashi and K. Kitagawa *"Optimization of the incision size and cold-end temperature of a thermoelectric device"* Energy Vol. 30, 2156 (2005)
- [65] B.S. Yilbas B.S. and A.Z. Sahin, *"Thermoelectric Device and Optimum External Load Parameter and Slenderness Ratio"* Energy, Vol. 35, 5380(2010)
- [66] ABAQUS Theory Manual, Version 6.10, 2010, ABAQUS Inc., Pawtucket, USA
- [67] Y. Ootao and Y. Tanigawa *"Three-dimensional solution for transient thermal stresses of functionally graded rectangular plate due to nonuniform heat supply"* Int. J Mechanical Science, Vol. 47, 1769 (2005)
- [68] Engineering fundamentals website; element information of copper, "http://www.efunda.com/materials/elements/element_info.cfm?Element_ID=Cu"
- [69] T. A. Hahn *"Thermal Expansion of Copper from 20 to 800 K"* J. Appl. Phys., Vol. 41, 5096 (1970)
- [70] Y. Tong, F. Yi, L. Liu, P. Zhai, and Q. Zhang *"Molecular dynamics study of mechanical properties of bismuth telluride nanofilm"* Physica B, Vol.405, 3190 (2010)

VITA

Name: Abdulrahman Salman Almerbati

Place of Birth: Dhahran, Saudi Arabia

Nationality: Saudi

Permanent Address: South Al-Khobar, P.O.BOX 20200, Zip. 31952
Al-Joubail St. 24-24 Cross-Road,
Al-Khobar, Saudi Arabia

Telephone: 00966-531399911, 00966-38819215

Email Address: Abdulrahman.salman@gmail.com

Educational Qualification:

M.S (Mechanical Engineering)
May 2012
King Fahd University of Petroleum and Minerals
Dhahran, Saudi Arabia.

B.E. (Mechanical Engineering)
September 2009
King Fahd University of Petroleum and Minerals
Dhahran, Saudi Arabia